Review

THE 2017 RELEASE OF Cloudy

G. J. Ferland[1], M. Chatzikos[1], F. Guzmán[1], M. L. Lykins[1], P. A. M. van Hoof[2], R. J. R. Williams[3], N. P. Abel[4], N. R. Badnell[5], F. P. Keenan[6], R. L. Porter[7], and P. C. Stancil[7]

RESUMEN

Se presenta la versión 2017 del código de síntesis espectral Cloudy con mejoras en la precisión y tratamiento de la física hechas desde la version previa. La exportación de los datos atómicos hacia bases de datos externas ha permitido la incorporación de grandes conjuntos de nuevos datos. El uso completo de éstos no es práctico para la mayoría de las simulaciones, así que describimos el subconjunto de datos usado por defecto y que predice un número considerablemente mayor de líneas que en la versión previa. No obstante, la versión actual es más rápida debido a la optimización del código. Se dan ejemplos de los límites de precisión de los modelos pequeños y de los requisitos de rendimiento para los modelos completos. Se resumen avances en los modelos para iones con secuencias isoelectrónicas de H y He y el uso de modelos colisionales-radiativos completos en la determinación de las densidades donde las aproximaciones coronal y de equilibrio termodinámico local funcionan.

ABSTRACT

We describe the 2017 release of the spectral synthesis code Cloudy, summarizing the many improvements to the scope and accuracy of the physics which have been made since the previous release. Exporting the atomic data into external data files has enabled many new large datasets to be incorporated into the code. The use of the complete datasets is not realistic for most calculations, so we describe the limited subset of data used by default, which predicts significantly more lines than the previous release of Cloudy. This version is nevertheless faster than the previous release, as a result of code optimizations. We give examples of the accuracy limits using small models, and the performance requirements of large complete models. We summarize several advances in the H- and He-like iso-electronic sequences and use our complete collisional-radiative models to establish the densities where the coronal and local thermodynamic equilibrium approximations work.

Key Words: atomic processes — galaxies: active — methods: numerical — molecular processes — radiation mechanisms: general

[1]University of Kentucky, Lexington, USA.
[2]Royal Observatory of Belgium.
[3]AWE plc, UK.
[4]University of Cincinnati, USA.
[5]University of Strathclyde, Glasgow, UK.
[6]Queen's University Belfast, Belfast, UK.
[7]University of Georgia, USA.

CONTENTS

1. INTRODUCTION

We introduce the next major version of CLOUDY, version C17. CLOUDY is a non-local thermodynamic equilibrium (NLTE) spectral synthesis and plasma simulation code designed to simulate astrophysical environments and predict their spectra. The previous version of CLOUDY, C13, is described in Ferland et al. (2013), hereafter referred to as C13, while the last major review before C13 was Ferland et al. (1998). These give an overview of the scope and goals for our simulation code. The basic physics is described in Osterbrock & Ferland (2006), hereafter referred to as AGN3. Ferland (2003) goes into some atomic and plasma physics questions with examples of CLOUDY applications to photoionized clouds.

A great effort since C13 has gone into moving CLOUDY's atomic and molecular data into external databases. These external databases make it possible to compute intensities of a great many emission lines. A theme running through this review is the tradeoff between the increased accuracy that comes from including larger and more complete models, and the associated increase in time and memory. For this reason using the full databases is usually not practical. Command-line user options control the size of the various model atoms, ions, and molecules. With all databases fully used the number of lines is increased by well over an order of magnitude, and the default setup predicts significantly more lines than the previous release. Despite the increased number of lines, in its default state C17 is actually faster than C13 because of a good number of optimizations introduced to the code base.

The next sections describe how we incorporate a number of external databases to compute large and complex models of ionic and molecular emission. We then discuss how we determine the ionization and emission of the gas, and its range of validity. Other major changes to the physics and functionality of the code are also reviewed. The external data, with its common user interface and underlying software, make it simple to report such quantities as the column density or population in a particular level of a species, or its spectrum. We give examples of using CLOUDY to compute both equilibrium (Lykins et al. 2013; Wang et al. 2014) and non-equilibrium (Chatzikos et al. 2015) cooling. The former occurs if the system has not changed over timescales longer than those required for atomic processes to reach steady state. The latter occurs mainly at temperatures at or below the 10^5 K peak in the cooling function, if the temperature changes too rapidly for the system to come into ionization equilibrium. Another change includes options to remove isotropic continuum sources, such as the CMB, from the spectral predictions.

We do not review those parts of the code, its documentation, user support sites, or web access that have not changed since the release of C13. The C13 review paper remains the primary documentation for those parts of this release.

2. DATABASES

2.1. *The Move to External Databases*

The greatest effort since C13 has gone into a massive reorganization of our treatment of ions, atoms, or molecules, which we collectively refer to as "species". Cloudy originally added species models on a case-by-case basis, with the data mixed in with the source. This was a significant maintenance problem since only people with a working knowledge of C++ could update the data. We have largely moved the data into external databases. As much as possible we treat all species with a common code base. New models are added to our Stout database (Lykins et al. 2015), which was designed to present data in formats as close as possible to the original data sources, for ease of maintenance.

These databases make it possible to create very extensive models of line emission that include a very large number of levels, although this comes at the cost of longer computing times. They also provide the flexibility of including far fewer levels, with faster execution time, but with a less realistic representation of the physics. This compromise between speed and precision will be a theme running throughout this review.

There are five distinct databases used to model spectral lines. These are outlined here and, in more detail, in later sections.

2.1.1. *The H-like and He-like Iso-electronic Sequences*

We treat atomic one and two electron systems (except H^-) with full collisional radiative models, referred to as CRM (see the review by Ferland & Williams 2016). These models are described in greater detail in § 3.1 below. The models are complete, are capable of making highly accurate predictions of emission, and go to the interstellar medium (ISM), Local Thermodynamic Equilibrium (LTE) and Strict Thermodynamic Equilibrium (STE) limits when appropriate. As described in § 3.2 below, our models of other ions are not as complete.

2.1.2. *The H_2 Molecule*

This, the most common molecule in the universe, is treated as an extensive model introduced in Gargi Shaw's thesis (Shaw et al. 2005). Improvements are described in greater detail in § 5 below.

2.1.3. *Stout, CHIANTI, and LAMDA Models*

We treat emission from atoms, ions, and molecules (other than those described in the previous sections) using the Stout, CHIANTI, and LAMDA databases. These use a common codebase and are controlled in very similar ways. The H-like and He-like iso-sequences, and the H_2 model, were created as separate projects and are controlled by a separate set of commands.

For molecules, we use the Leiden Atomic and Molecular Database "LAMDA"[8] (Schöier et al. 2005). § 5.5 below gives more details. For some ions, we use version 7.1.4 of the CHIANTI[9] database (Dere et al. 1997; Landi et al. 2012), as described by Lykins et al. (2013).

We add new species to our Stout database (Lykins et al. 2015). The data format is designed to be as close as possible to the presentation tables in the original publications. This makes Stout easy to maintain and update. We use NIST energy levels where possible.

The original publications defining the LAMDA and CHIANTI databases should be consulted to find the original references for individual data sources. Our Stout database is constantly updated. Appendix B gives a summary and references for the data it uses.

There are many species for which NIST gives level energies and transition probabilities but no collision data are available. For these we use NIST data with collision rates from the g-bar approximation (Burgess & Tully 1992). We refer to these as "baseline" models in Appendix B. Lykins et al. (2015) give further details.

Baseline model wavelengths should be accurate, and the transition probabilities are matched to the energy levels, but the g-bar collision strengths are highly approximate. High-quality collision data *are* available for most astrophysically important species, as shown in Appendix B, so baseline models are mainly used for species that are not commonly observed.

There are several considerations to keep in mind if a baseline species is important in a particular application. First, the collision rates are highly approximate, so at low densities the line intensities will be too. If the density is high enough for the levels to be in LTE the predictions will be fine. However, with some effort, the predictions could be improved. First, the OPEN-ADAS data collection[10]

---

[8]http://www.strw.leidenuniv.nl/~moldata/
[9]http://www.chiantidatabase.org/
[10]http://open.adas.ac.uk/

does include plane-wave Born or distorted-wave collision rates. These are better than g-bar but the data set is not matched to NIST energies. This matching can be done with some effort, as has been done for Fe II (Verner et al. 1999) and Si II (Laha et al. 2016). Alternatively, members of the atomic physics community could be asked to produce close-coupling collision rates for the astrophysical application.

Cloudy has long included a large and very complete model of Fe II emission which was developed as part of Katya Verner's thesis (Verner et al. 1999). Modern atomic calculations now routinely provide datasets of similar or larger size, so the current version of Cloudy can create complex emission models of any species with sufficient data. The Verner et al. (1999) Fe II model is now fully integrated into the Stout database.

2.2. *Species and their Names*

Cloudy simulates gas ranging from fully ionized to molecular. Nomenclature varies considerably between chemical, atomic, and plasma physics. We have adopted a naming convention that tries to find a middle ground between these different fields.

A particular atom, ion, or molecule is referred to as a "species". A species is a baryon, and this release of Cloudy has 625 species. Examples are CO, H_2, H^+, and Fe^{22+}. Species are treated using a common approach, as much as possible. Our naming convention melds a bit of each of these fields because a single set of rules must apply to all species.

- Species labels are case sensitive, to distinguish between the molecule "CO" and the atom "Co".

- At present we do not use "_" to indicate subscripts, or "^" to indicate charge.

- Molecules are written pretty much as they appear in texts. H_2, CO, and H^- would be written as "H2", "CO", and "H-".

- Atoms are the element symbol by itself. Examples are "H" or "He" and *not* the atomic physics notation H^0 or He^0.

- Ions are given by "+" followed by the net charge. Examples are "He+2" or "Fe+22" and *not* the correct atomic physics notation, He^{2+} or Fe^{22+}. The latter would clash with notation for molecular ions. "C2+" indicates C_2^+ in our notation.

- We specify isotopes using "^" and the atomic weight placed before the atom to which it refers.

For example, "^13CO" is the carbon monoxide isotopologue ^{13}CO.

Appendix B lists our species together with the database used to treat them.

2.3. *Working with Spectral Lines*

These species may emit a collection of photons which we refer to as a spectrum, although the species and spectrum may be labeled differently. We follow the spectroscopic convention that a spectral line is identified by a label and a wavelength. The next sections discuss how each is specified.

2.3.1. *Specifying Spectral Lines*

We follow a modified atomic physics notation for the spectrum. In atomic physics, H I, He II, and C IV are the spectra emitted by H^0, He^+, and C^{3+}. "H I" indicates a collection of photons while H^0 is a baryon. In our notation, we replace the Roman numeral with an integer so we refer to the spectrum as "H 1" and the baryon as "H" in the output. For example, H I $\lambda4861$Å, He II $\lambda4686$Å, and the C IV $\lambda1549$Å doublet would appear in the output as H 1 4861.36, He 2 4686.01, and Blnd 1549.00 (blends are discussed below).

Chemistry does not suffer from this distinction between baryons and spectra so the species label is also the spectroscopic ID. Some examples of molecular lines in the output might include H2O 538.142m, HNC 1652.90m, HCS+ 1755.88m, CO 2600.05m, CO 1300.05m, ^13CO 906.599m. In this context the "m" indicates microns rather than our default angstrom unit.

To summarize, atomic hydrogen would be referenced as "H" while the Lα line would be "H 1". The distinction is important because, depending on whether it is formed by collisional excitation or recombination, Lα can trace either H^0 or H^+.

We continue to follow the spectroscopic convention of denoting a line by its species label and wavelength. This has the problem that several lines in a rich spectrum may have the save wavelength, at least to our quoted precision. An example is the strongest molecular hydrogen line that can be measured from the ground. The H_2 1-0 S(1) transition has a wavelength of 2.121 μm. However there are a number of H_2 lines with nearly this wavelength; 3-2 S(23) 2.11751μm, 1-0 S(1) 2.12125μm, and 3-2 S(4) 2.12739μm. We ameliorate this confusion by reporting the wavelengths with six significant figures in this version. However, this method of identifying lines is fragile and it is still possible that the code will find a line with the specified wavelength that is not the intended target.

2.3.2. *Line Blends*

We introduce the concept of "line blends" in this version. These have the label "Blnd" in the main output, and a simplified wavelength. An example is `Blnd 2.12100m`, which is the sum of the three H_2 lines mentioned above. Operationally, a spectrometer measures the total flux through one spectral resolution element and it is frequently not possible to identify individual contributors to what appears as a single spectral feature. The `Blnd` output option makes it possible for Cloudy to report what is measured.

There are other cases where spectroscopists report the total intensity of a multiplet even when individual members can be measured. Two examples are the [O II] $\lambda\lambda3726, 3729$ and [S II] $\lambda\lambda6731, 6716$ doublets. We report the total multiplet intensity as `Blnd 3727` and `Blnd 6720`. Such multiplet sums had been added to Cloudy on an ad hoc basis in previous versions, often with the label "TOTL". The "Blnd" entry makes the notation consistent across the code and allows it to be included in the reporting framework described in § 2.6.5.

2.3.3. *Air vs Vacuum Wavelengths*

The convention in spectroscopy, dating back to 19th century experimental atomic physics, is to quote line wavelengths in vacuum for $\lambda < 2000$Å and air wavelengths for $\lambda \geq 2000$Å. Cloudy has long followed this convention.

There is an increasing trend to use vacuum for all wavelengths, e.g. due to satellite missions and the Sloan project[11]. We provide a command, `print line vacuum`, to use vacuum wavelengths throughout. The continuum reported by the family of `save continuum` commands, used in several of the examples presented below, is always reported in vacuum wavelengths to avoid a discontinuity at 2000Å.

2.4. *Which Database for Which Species?*

The H-like and He-like iso-electronic sequences are always included, although the default number of levels is a compromise between speed and precision. This is discussed in § 3.1. It is not possible to substitute other models, for instance, CHIANTI, for these species. These iso-sequences are integrated into the ionization-balance solver, so they are needed for it to function.

The large H_2 model is not used by default. It is enabled with the command `database H2`. In this comprehensive model, radiative/collisional processes

are coupled to the dissociation/formation mechanisms and resulting chemistry.

The remaining databases, Stout, CHIANTI, and LAMDA, have different emphases. LAMDA has a focus on molecules and PDRs, while CHIANTI is optimized for solar physics and models in collisional ionization equilibrium. Nonetheless, there are some species that are present in more than one database.

Each database has its own "`masterlist`" file that specifies which of its models to use. The `masterlist` file follows the naming convention used within its database. For CHIANTI and Stout, the internal structure of C^{3+}, which produces C IV emission, is called "c_4". The water molecule in LAMDA is referenced as "H2O". If a particular species is specified in more than one `masterlist` file we will use Stout if it exists, then CHIANTI, followed by LAMDA.

A small part of the default Stout `masterlist` file is shown here:

```
#c mn_23
#n mn_3
#n mn_4
mn_5
mn_6
#c mn_8
#c mn_9
# 50 levels for N I to do continuum pumping discussed in
# >>refer  Ferland et al., 2012, ApJ 757, 79
n_1  50
#c n_2
#c n_3
#c n_4
n_5
na_1
na_2
#c na_3
#c na_4
```

This file lives in the `cloudy/data/stout/masterlist` directory. Similar files are located in the `cloudy/data/chianti/masterlist` and `cloudy/data/lamda/masterlist` directories. Each line in the file has a species label and those beginning with "#" are available but are commented out (we use the "#" character to indicate comment lines across our data files). This shows that we use Stout models of Mn V, Mn VI, N I, Na I, and Na II. We might use CHIANTI data, or ignore, species that are commented out.

It is easy for the user to use species from different databases by editing the `masterlist` files. But there are consequences of using a non-default database. The biggest is that different databases will often have different versions of the level energies. The line wavelengths may change because we derive the wavelength from the level energies. We

---

[11]`http://www.sdss.org/dr12/spectro/spectro_basics/`

use both the line label and the extended precision form of the wavelength to match lines. This may break down if the wavelengths change significantly.

We do support changing the databases but in release versions of the code have created MD5 checksums for all of the data included in the download. A caution will be reported if the non-default data files are used. This is intended to remind the user that our default data files have been changed in some way.

2.5. *How Complete a Model Should be Done?*

The default setup for the iso-electronic sequences is described below. When our H_2 model is selected, the full dataset is used.

The Stout, CHIANTI, and LAMDA databases have similar user interfaces. The default number of levels is described in Lykins et al. (2013). For a particular species, the temperature of maximum ion abundance is hotter in a collisionally-ionized gas than in the photoionized case. Because of this higher kinetic temperature, more levels will be energetically accessible in the collisional case. By default, we use 50 levels for the collisional and 15 levels for the photoionization case.

The number of levels can be adjusted to suit particular needs. There are several ways to do this. The command `database species "name" levels xxx` will change the number of levels for a particular species. The command `database CHIANTI levels maximum` will make all of the CHIANTI models as large as possible. Similar commands also work for the Stout and LAMDA databases. Finally, the minimum number of levels for a species can be specified in its `masterlist` file by entering a number after the species label. For instance, faint optical [N I] lines in H II regions are mainly excited by continuum fluorescence (Ferland et al. 2012). This physics requires that the lowest fifty levels of N I be included. This was done in C13 by explicitly including those levels in the C++ source. In this version we specify this minimum number of levels in the Stout `masterlist` file. The example portion of the Stout `masterlist` file given above includes this particular case.

With these databases we predict, by default, more lines in this version of CLOUDY than with C13. This actually takes less computer time because of memory and other optimizations described below. Figure 1 compares the density of lines per $1000~\mathrm{km\,s^{-1}}$ velocity interval for C13, given as the black dots, and our default setup for C17, the red dots. Most spectral regions now have more lines, often by up to 50%.

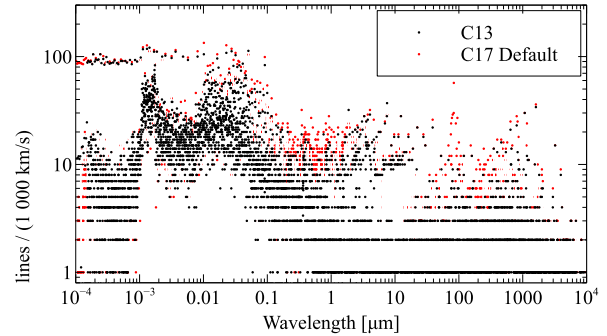Figure 2 compares the density of lines per velocity bin in our default setup versus a calculation with

Fig. 1. This compares the number of lines that fall into $1000~\mathrm{km\,s^{-1}}$ velocity bins in C13 (black) and the default C17 setup (red). The color figure can be viewed online.

the databases made as large as possible. The upper panel presents the "big picture", the line density over the full spectral range we cover, a frequency of 10 MHz ($\lambda \approx 29.98$ m – this is approximately the lowest frequency observable through the ionosphere) and an energy of $h\nu = 7.354 \times 10^6$ Ryd ($\approx 100\,\mathrm{MeV}$). Few lines are present shortward of $10^{-4}\mu$m $= 1$Å or longward of $3 \times 10^6~\mu$m$= 3$m. The lower panel zooms into the mid-spectral region with significant numbers of lines. The red points indicate our default C17 setup. The upper envelope of black points results from making the databases as large as possible.

We will give example input scripts across this document to show how various Figures were produced. The large-database calculation in Figure 2 was created with the following input deck:

```
table AGN
ionization parameter -2
stop zone 1
constant temperature 1e4 K
hden 0
database H2
database H-like levels resolved 5
database He-like levels resolved 5
database H-like levels collapsed 200
database He-like levels collapsed 200
database CHIANTI levels maximum
database stout levels maximum
database LAMDA levels maximum
save continuum units microns "mesh.con"
```

All commands are fully documented in "Hazy 1", CLOUDY's documentation, which is part of the download. Most commands are unchanged from C13. The spectral energy distribution (SED) is our generic Active Galactic Nucleus (AGN) continuum, with an ionization parameter of $U = 10^{-2}$. The geometry is a single zone with a hydrogen density of $1\,\mathrm{cm^{-3}}$ and a gas kinetic temperature set to 10^4 K. These have to be specified to get the code to run and were
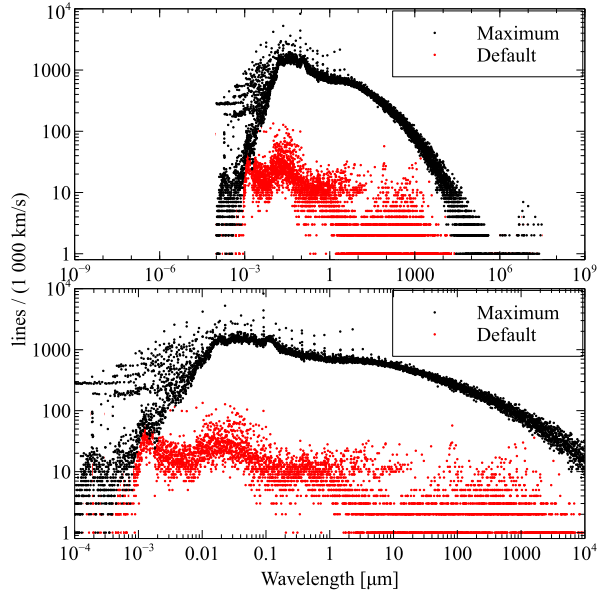
Fig. 2. This shows the number of lines that fall into 1000 km/s velocity bins, across the spectrum. The red points for default setup and the black points give the number of lines the are predicted when the databases are made as large as possible. The upper panel shows the full spectral range considered by the code, while the lower panel shows the peak of the line density. The color figure can be viewed online.

chosen to do the simplest and fastest calculation. As described here, the `database` commands are new in C17 and control the behavior of the databases.

The number of lines per spectral bin is one of the items in the file produced by the `save continuum` command. The width of each continuum bin, or, equivalently, the spectral resolution, can be adjusted in two ways. The default continuum mesh can be changed by a uniform scale factor with the `set continuum resolution ...` command. This method is used in several simulations presented below to increase the spectral resolution to highlight particular issues in the spectrum. Alternatively, the initialization file `continuum_mesh.ini` in the `data` directory can be changed to alter the default continuum mesh. This second method was used to make the C13 and C17 continuum meshes the same, to allow the comparison in Figure 1.

Figure 2 shows that it is possible to predict a very large number of lines, but this comes at great cost. The default C17 calculation took 4.3 s on an Intel Core I7 processor while the calculation using the large databases took 1822 s, roughly half an hour. It would not now be feasible to use the full databases in a realistic calculation in which the temperature

solver is used and the cloud has a significant column density so that optical depths are important.

2.6. *Generating Reports*

2.6.1. `database print`

The command `database print` generates a report listing all species. The following would generate a report for Cloudy in its default setup:

```
test
database print
```

This command was used to generate Tables 2 and 3 giving the default setup for the one- and two-electron iso-sequences. A small portion of the report for the Stout, CHIANTI, and LAMDA databases follows:

```
Using LAMDA model SO with 70 levels of 91 available.
Using LAMDA model SiC2 with 40 levels of 40 available.
Using LAMDA model CS with 31 levels of 31 available.
Using LAMDA model C2H with 70 levels of 102 available.
Using LAMDA model OH+ with 49 levels of 49 available.
Using STOUT spectrum Al 1 (species: Al) with 15 levels of 187 available.
Using STOUT spectrum Al 3 (species: Al+2) with 15 levels of 83 available.
Using STOUT spectrum Al 4 (species: Al+3) with 15 levels of 115 available.
Using STOUT spectrum Zn 2 (species: Zn+) with 15 levels of 27 available.
Using STOUT spectrum Zn 4 (species: Zn+3) with 2 levels of 2 available.
Using CHIANTI spectrum Al 2 (species: Al+) with 15 experimental energy levels of 20 available.
Using CHIANTI spectrum Al 5 (species: Al+4) with 3 experimental energy levels of 3 available.
Using CHIANTI spectrum Al 7 (species: Al+6) with 15 experimental energy levels of 15 available.
Using CHIANTI spectrum Al 8 (species: Al+7) with 15 experimental energy levels of 20 available.
Using CHIANTI spectrum Al 9 (species: Al+8) with 15 experimental energy levels of 54 available.
```

Each line of output gives the database name, the spectroscopic designation, the species designation, the number of levels used, and the total number available. With CHIANTI there is the further option to use all levels, or only those with experimental (measured) energies.

2.6.2. `save species labels all`

The `save species labels all` command will produce a file containing the full list of species labels. One can generate this list by running the following input deck:

```
test
save species labels "test.slab" all
```

Table 1 shows a small part of the resulting output. There are several important points in this Table. First, several species do not list a database. The cases of "H+", "He+2", and "C+6" are bare nuclei and have no electronic levels, while the negative hydrogen ion"H-" and the molecules "HeH+", "C2+" and "CN+" do have internal levels in nature, but we currently do not have models of these systems. The remainder are treated with one of the databases described above. Although many of these species have no internal structure, other species properties,

TABLE 1

SAVE SPECIES LABEL EXAMPLE

Species label	Database
H	H-like
H+	
H-	
He	He-like
He+	H-like
He+2	
HeH+	
C	Stout
C+	Stout
C+2	Stout
C+3	CHIANTI
C+4	He-like
C+5	H-like
C+6	
C2+	
C2H	LAMDA
NH3	LAMDA
CN	LAMDA
CN+	
HCN	LAMDA

especially the column density, are computed and reported.

Note a likely source of confusion. As described above, "C+2" is doubly ionized carbon, while "C2+" is an ion of molecular carbon.

2.6.3. `print citation`

The `print citation` command reports the ADS links to papers defining the databases we use. We encourage users to cite the original source of any data that played an important role in an investigation. This will support and encourage atomic, molecular, and chemical physicists to continue their valuable work.

2.6.4. `save species` *Commands*

It is easy to report internal properties of a species, such as the column density or population of a particular level. The following is an example of a `save species` command used to report the column densities of several species and the visual extinction:

```
save species column densities "test.col"
"e-"
"CO[2]"
"C[1:5]"
"H2"
```

```
"H"
"H+"
"*AV"
end of species
```

The total column density of electrons, H_2, H^0, and H^+ would be reported, along with the population in the $J = 1$ level of CO, and the first five levels of C^0. Note that the level index within the "[xx:yy]" counts from a lowest level of 1.

2.6.5. `Save line labels`

The `save line labels` command creates a file listing all spectral-line labels and wavelengths in the same format as they appear in the main output's emission-line list. This is a useful way to obtain a list of lines to use when looking for a specific line. The file is tab-delimited, with the first column giving the line's index within the large stack of spectral lines, the second giving the character string that identifies the line in the output, and the third giving the line's wavelength in any of several units. Each entry ends with a description of the spectral line. Lines derived from databases (CHIANTI, Stout, LAMDA) are followed by a comment that contains the database of origin and the indices of the energy levels, as listed in the original data.

An example of some of its output follows:

```
    4 Inci            0  total luminosity in incident continuum
    5 TotH            0  total heating, all forms, information since individuals
                         added later
    6 TotC            0  total cooling, all forms, information since individuals
                         added later
 1259 H  1      911.759A radiative recombination continuum
 1260 H  1      3646.00A radiative recombination continuum
 1261 H  1      3646.00A radiative recombination continuum
 1262 H  1      8203.58A radiative recombination continuum
 3552 H  1      1215.68A H-like, 1 3,   1^2S -   2^2P
 3557 H  1      1025.73A H-like, 1 5,   1^2S -   3^2P
 3562 H  1      972.543A H-like, 1 8,   1^2S -   4^2P
 5328 Ca B      1640.00A case a or case b from Hummer & Storey tables
 5329 Ca B      1215.23A case a or case b from Hummer & Storey tables
73487 CO        2600.05m LAMDA, 1 2
73492 CO        1300.05m LAMDA, 2 3
73497 CO        866.727m LAMDA, 3 4
85082 C  3      1908.73A Stout, 1 3
85087 C  3      1906.68A Stout, 1 4
85092 C  3      977.020A Stout, 1 5
180217 Al 8     5.82933m CHIANTI, 1 2
180222 Al 8     2139.33A CHIANTI, 1 4
180227 Al 8     381.132A CHIANTI, 1 8
312763 H2       1.13242m diatoms lines
312768 H2       1.26316m diatoms lines
312854 Blnd     2798.00A Blend: "Mg 2      2795.53A"+"Mg 2      2802.71A"
312855 Blnd     615.000A Blend: "Mg10      609.794A"+"Mg10      624.943A"
```

3. THE IONIZATION EQUILIBRIUM

Our goal is to compute the ionization for a very wide range of densities and temperatures, as shown in Figures 17 and 18 of C13, for the first thirty elements and all of their ions.[12] This development is complete for the H- and He-like iso-electronic sequences, but is still in progress for many-electron systems. This is challenging because of limitations in

---

[12]Those figures were created using the output of `grid_extreme` from our test suite.

the available atomic data, computer hardware, and human effort. We currently use a hybrid scheme, outlined below, which is motivated by the astrophysical problems we wish to solve. Figure 3 shows energy levels for five typical species, to serve as an example of some of the issues involved in the following discussion.

There are two simple limits for the solution of the ionization equilibrium. At the low densities found in the interstellar medium (ISM), most ions are in the ground state and the ionization rate per unit volume is proportional to the atom density multiplied either by the electron density, in the case of collisional ionization, or the ionizing photon flux, in the case of photoionization. The recombination rate per unit volume is proportional to the product of the ion and electron density. The density dependence drops out for the case of collisional ionization (see Equation 4 below). In contrast, at very high densities, such as the lower regions of a stellar atmosphere, the ionization is given by the Saha-Boltzmann equation and is inversely proportional to the electron density (Equation 5 below). CLOUDY spans both regions so neither approximation can be made and a full solution of the NLTE equations should be performed to obtain the ionization balance and level populations.

In a collisional-radiative model (CRM), the name given to the full NLTE treatment in plasma physics, the level populations are determined self-consistently with the ionization. That is, the populations in bound levels and the continuum above them in Figure 3 are solved as a coupled system of equations. We use this approach for the H-like and He-like isosequences, as described in C13 and the following sections, and shown in Figures 17 and 18 of C13. A modified two-level approximation, described below, is used for other species. This hybrid approach is motivated by the physics of the systems shown in Figure 3.

3.1. The H- and He-like Iso-electronic Sequences

Energy levels for H^0 are shown in Figure 3 on the left. This structure is valid for all ions of the H-like isoelectronic sequence. For H^0, the first excited $n = 2$ level occurs at an energy $E \approx (1 - 1/n^2) \approx 0.75$ of the ionization limit. This lowest excited level is much closer to the continuum above it than to the ground state below it. At the low kinetic temperatures found in photoionization equilibrium there should be little collisional coupling between excited and ground states because of this large energy separation, although very highly excited levels are strongly coupled to the continuum above. As
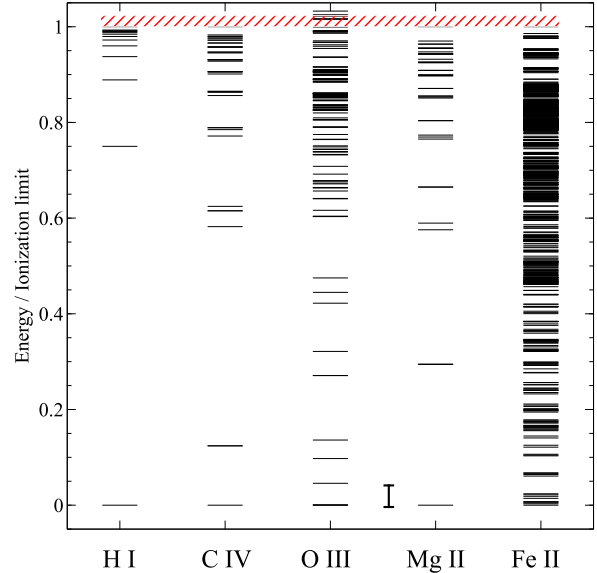

Fig. 3. Experimental energy levels (Kramida et al. 2014) for some species present in an ionized gas. The energies are given relative to the ionization potential (IP). Of these ions, only O III and Mg II have data for autoionizing levels, shown as the levels above the ionization limit indicated by the red hashed box. The autoionizing levels of Mg II are not visible since they are far above the ionization limit. The vertical bar in the middle, corresponding to E/IP = 0.05, is a typical gas kinetic energy in a photoionized plasma and is shown to indicate which levels are energetically accessible from the ground state. The color figure can be viewed online.

a result, the very highly excited "Rydberg" levels are populated following recombination from the ion above it, rather than collisional excitation from the ground state, in photoionization equilibrium. Most optical and infrared emission is produced following recombination in this case. The energies of the n-shells are also roughly valid for the He-like sequence. These two-electron systems behave in a similar manner; optical and IR lines form by recombination.

We treat these two iso-electronic systems with a full CRM because of the strong coupling of excited level populations to the continuum (C13). A large coupled system of equations is solved to determine both the level populations and the ionization, so the two are entirely self-consistent. Predictions over a wide range of density and temperature are shown in Figures 17 and 18 of C13. We developed a unified model for both the H-like and He-like isoelectronic sequences that extends from H to Zn, as described by Bauman et al. (2005); Porter et al. (2007); Porter

& Ferland (2007); Porter et al. (2012) and Luridiana et al. (2009), As shown in C13, and previously by Ferland & Rees (1988), our model of the ionization and chemistry of hydrogen does go to the correct limits at high (LTE) and low (ISM) densities, and to the strict thermodynamic equilibrium (STE) limit when exposed to a true blackbody. This is only possible when the ionization and level populations are self-consistently determined by solving the full collisional-radiative problem.

3.1.1. Recent Developments

The H- and He-like isoelectronic-sequences, coupled with the cosmic abundances of the elements, cause their spectra to fall into two very different regimes. For brevity, we refer to these as iso-sequences in the following. Hydrogen and helium have low nuclear charge Z and so have low ionization potentials, $IP \sim Z^2$. As a result, H I, He I, and He II emission is produced in gas with nebular temperatures, $\approx 10^4$ K, and occurs mainly in the optical and infrared. A goal of the current development is the prediction of highly accurate line emissivities as a step towards measuring the primordial helium abundance (Porter et al. 2007).

The next most abundant elements, starting with carbon ($Z = 6$), have high ionization potentials, $IP \geq 6^2$ Ryd, so are produced in very hot gas, $T \geq 10^6$ K, and emit X-rays (Porter & Ferland 2007; Porter et al. 2006). Heavy elements of these iso-sequences fall into very different spectral regimes than hydrogen and helium, probe gas with very different physical conditions, and so are found in distinctly different environments.

The high precision needed for primordial helium measurements means that the atomic data must be quite accurate. We are revisiting this problem. The original papers on H I and He I emission (Brocklehurst 1971, 1972; Benjamin et al. 1999; Hummer & Storey 1987) all used the Pengelly & Seaton (1964) theory of l-changing collisions. Vrinceanu & Flannery (2001b,a) and Vrinceanu et al. (2012) present an improved theory for these collisions, which predict rate coefficients that are $\approx$6 times smaller. We have used these newer rates in most of our published work (Bauman et al. 2005; Porter et al. 2007; Porter & Ferland 2007; Porter et al. 2012; Luridiana et al. 2009), and in C13.

There are good reasons, outlined in Guzmán et al. (2016), to prefer the Pengelly & Seaton (1964) theory. Guzmán et al. (2017b) extend this treatment to He-like systems, in which the low-l S, P, and D states are not energy-degenerate, so an extra cut-off

energy term is applied to the probability integral as in Pengelly & Seaton (1964). Guzmán et al. (2017b) also improve the Pengelly & Seaton (1964) approximations to deal with low densities and high temperatures, where the original formulae could produce negative values. They call this the modified Pengelly & Seaton (1964, PS-M) approach. Williams et al. (2017) extend the semi-classical theory of Vrinceanu & Flannery (2001b) to provide thermodynamically consistent l-changing rates, which are found to agree quite closely with the results of the other approaches.

These differences affect the predictions. In Figure 4, the line emissivities from the different approaches are divided by the emissivities obtained using PS-M. Here, a single layer of gas has been considered and emissivities from recombination lines calculated. A cosmic helium abundance, He/H =0.1, was assumed. The cloud is radiated by a monochromatic radiation field using CLOUDY's laser command. It was centered at 2 Ryd, with an ionization parameter of $U = 0.1$ (Osterbrock & Ferland 2006). The state of the emitting gas in these conditions resembles that in H II regions, observationally relevant for the determination of He abundances (Izotov et al. 2014). The monochromatic radiation field was used to prevent internal excitations that would be produced by a broadband incident radiation field. A constant gas kinetic temperature of 1×10^4 K is assumed. We assume 'Case B' (Baker & Menzel 1938), where Lyman lines with upper shell $n > 2$ are assumed to scatter often enough to be degraded into Balmer lines and Lyα. The hydrogen density is varied over a wide range and the electron density is calculated self-consistently. The latter is approximately 10% greater than the hydrogen density, since He is singly ionized. The atomic data used for He and H emission, except for l-changing collisions, are the 'standard' set of data that have been described in previous work (Porter et al. 2005).

In Figure 4, the most accurate quantum mechanical treatment, VOS12-QM (Vrinceanu & Flannery 2001b,a; Vrinceanu et al. 2012), agrees closely with PS-M. The semiclassical treatments, VOS12-SC (Vrinceanu & Flannery 2001b,a), and the further simplified approach, VOS12-SSC (Vrinceanu et al. 2012), produce differences of up to 10% in the predicted line intensities. The input to generate Figure 4 for the quantum mechanical case can be as follows[13]:

---

[13]The commands must be written in one line. Here, "\" is used to break the command in two lines for presentation purposes.

```
laser 2
ionization parameter -1
hden 4
element helium abundance -1
init file "hheonly.ini"
stop zone 1
set dr 0
database he-like resolved levels 30
database he-like collapsed levels 170
database he-like collisions l-mixing S62 \
      no degeneracy thermal VOS12 quantal
constant temperature 4
case b no photoionzation no Pdest
no scattering escape
no induced processes
iterate
normalise to "He 1" 4471.49A
monitor line luminosity "He 1" 7281.35A \
      -18.8686
```

In this input, the `no photoionization` option is added to `case b` to suppress photoionization from excited levels. Then, the pumping of the levels by the resulting photon field is removed by turning off the destruction of Lyman lines with the `no Pdest` option. The density is set to $10^4 \, \mathrm{cm}^{-3}$ using the `hden 4` command, and the temperature is kept constant with `constant temperature 4`. The commands:

```
stop zone 1
set dr 0
```

define a layer of gas of 1 cm thickness. The commands:

```
no scattering escape
no induced processes
```

prevent losses due to scattering, so that all Lyman lines are degraded into Balmer lines. The `monitor line luminosity ...` command compares the computed luminosities ($\mathrm{erg\,s}^{-1}$) of selected He I lines against the reference values given by the PS method. Luminosities can be directly translated into emissivities as the thickness of the gas is 1 cm.

Figure 4 has been computed extending to the $n = 200$ shell using the `database he-like resolved/collapsed levels` commands described in § 3.1.2. Most of the higher n-shells are collapsed (C13, Figure 1) assuming a statistical population for the l-subshells, while the low-n levels are resolved. The number of resolved levels needed is determined by the critical density for l-mixing, where collisional transition rates exceed radiative decay rates, as shown in figure 4 of Pengelly & Seaton

(1964). The number of resolved n-shells used to predict the lines in Figure 4 has been varied from $n = 60$ at the lowest density to $n = 20$ at the highest density.

Commands are provided to select the preferred l-changing theory in the input file for Cloudy. The command to use PS-M is:

```
database he-like collisions l-mixing S62 \
      no degeneracy Pengelly
```

The keyword `S62` in this command tells Cloudy to use the Seaton (1962) electron impact cross sections for the l-changing collisions of the highly non-degenerate $l < 3$ subshells (see Guzmán et al. 2017b). The keyword `no degeneracy` uses an energy criterion (Pengelly & Seaton 1964) to account for the non-degeneracy of the l-subshells of He I Rydberg levels (see above). Calculations using the original formulas provided by Pengelly & Seaton (1964) can be used by adding the keyword `Classic`.

VOS12-QM rate coefficients can be used with the command:

```
database he-like collisions l-mixing S62 \
      no degeneracy thermal VOS12 Quantal
```

where the keyword `thermal` tells Cloudy to perform a Maxwell average for the cross sections. By default, the effective coefficients will not be Maxwell averaged, and energies of the collision particles will be taken to be kT. The evaluation at a single energy kT is significantly faster.

The VOS12-QM theory needs a larger number of operations than the analytic PS-M approach. It also needs a numerical integration of the collision probability to obtain the cross sections. These may be integrated once more to obtain the Maxwell averaged coefficients, making this method computationally slow. Simulations using VOS12-QM calculations are ≈ 60 times slower than those using PS-M. The computational cost of VOS12-QM calculations makes PS-M method the preferred one. The VOS12-QM method is recommended when very high-precision results are required.

Finally VOS12-SC and VOS12-SSC can be obtained using the commands:

```
database he-like collisions l-mixing S62 \
      thermal Vrinceanu
database he-like collisions l-mixing S62 \
      VOS12 semiclassical
```

respectively. While VOS12-SSC cross-sections can be obtained with an analytical formula, VOS12-SC need a double integration making them as computationally slow as VOS12-QM.
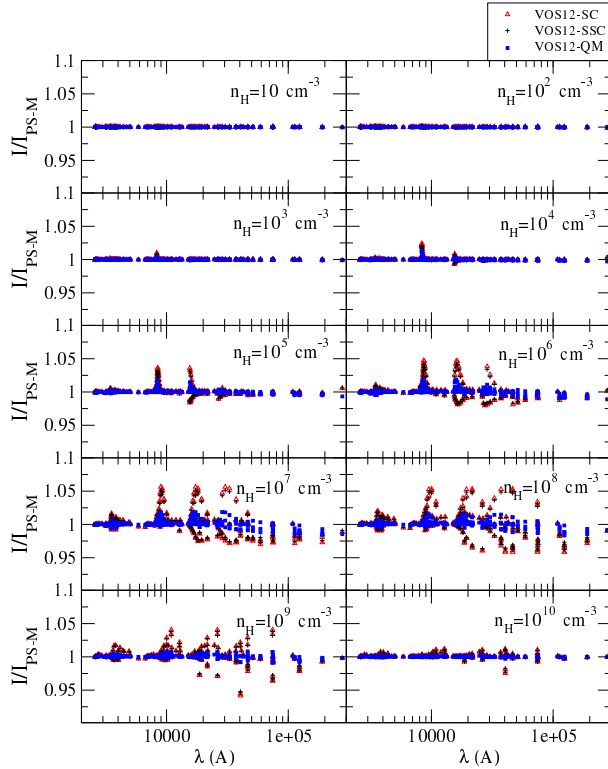
Fig. 4. Ratios of He I lines using the different datasets with respect to PS-M, see text for details. Figure from (Guzmán et al. 2017b). The color figure can be viewed online.

It is not now possible to experimentally determine which of the theories mentioned above is more correct, although we prefer the PS-M approach. Guzmán et al. (2017a) outline an astronomical observation that, while difficult, could conclusively determine which l-changing theory holds.

3.1.2. *Adjusting the Size of the Model*

Our models of the H- and He- like iso-sequences have a mixture of resolved and collapsed levels, as shown in Figure 1 of C13. Resolved levels are relatively expensive to compute due to the need to evaluate the l-changing collision rates described above. Collapsed levels assume that the l-levels are populated according to their statistical weight within the n shell, so this expense is avoided.

The number of resolved and collapsed levels are controlled by a family of commands similar to

```
database H-like hydrogen levels resolved 10
database H-like hydrogen levels collapsed 30
database H-like helium levels resolved 10
database H-like helium levels collapsed 30
database He-like helium levels resolved 10
database He-like helium levels collapsed 30
```

This example resolves $n \leq 10$ for H I, He I, and He II and adds 30 collapsed levels to make each atom extend through $n = 40$. These commands work for H-like and He-like ions of all elements up through zinc (Z=30).

The command:

```
database print
```

generates a report summarizing all databases in use during the current calculation. This includes the number of resolved and collapsed levels for the isosequences. By default we resolve $n \leq 10$ with an additional 15 collapsed levels for H I and He II, and $n \leq 6$ as resolved with an additional 20 collapsed levels for He I.

In C13 and earlier versions the collapsed levels were intended to "top off" the model and their treatment did not have spectroscopic accuracy. Bauman et al. (2005) discuss top off, the need to use a finite number of levels to approximate an infinite-level system, and its effects on predictions. We did not report lines from collapsed levels. A great deal of effort has gone into improving the physics of these levels. Their emission is now highly accurate if the implicit assumption that the l levels within the n shell are populated according to their statistical weight is valid. The densities required for this "well l-mixed" assumption can be derived from Figure 4 of Pengelly & Seaton (1964). We now report emission from collapsed levels up to $n < n_{highest} - 4$. This limit was chosen to avoid the "edge" effects discussed in the next subsection.

3.1.3. *Comparisons in the Case B Limit*

It is possible to judge the accuracy of the predicted lines by comparing with the textbook "Case B" spectrum (Baker & Menzel 1938). Case B is a well defined limit that is a fair approximation to nebulae (AGN3 § 4.2) and can serve as an important benchmark. Hummer & Storey (1987) and Storey & Hummer (1995) compute Case B emission and the second paper includes a series of machine-readable tables. We interpolate on these tables to include Case B predictions for H-like ions in the CLOUDY output. This makes comparison of our predictions with Case B simple.

While Case B is an idealized limit, it gives a fairly good representation of emission for low to moderate density photoionized nebulae (AGN3). The assumptions break down if Balmer or higher lines become optically thick, when collisional excitation from the ground state becomes important, or if Lyman lines can escape. Optical depth effects become important

in high radiation-density environments such as the inner regions of active galactic nuclei. Collisional contributions become important when suprathermal electrons are present as in X-ray ionized neutral gas (Spitzer & Tomasko 1968), or for hot regions such as very low metallicity nebulae. The Lyman lines may not be optically thick in low column density clouds. These processes are treated self-consistently in any complete Cloudy calculation.

Larger models, with more levels, make the spectrum more accurate, at the cost of longer execution times and higher memory requirements. The default H I model is a compromise between performance and accuracy.

Figure 5 compares our predictions with Storey & Hummer (1995) for a typical "nebular" temperature, $T_e = 10^4$ K, and two densities, $n(\mathrm{H}) = 10^4\,\mathrm{cm}^{-3}$ and $10^7\,\mathrm{cm}^{-3}$. The lower two panels show predictions of our default model at the two densities while the upper panel shows predictions at the lower density with a greatly increased number of resolved and collapsed levels.

In a normal calculation, Cloudy determines the line optical depths self-consistently, assuming the computed column densities, level populations, and line broadening. A `Case B` command exists to create these conditions and to make these comparisons possible while computing a single "zone", a thin layer of gas. The command sets the Lyman line optical depth to a large number and suppresses collisional excitation out of $n = 2$, to be consistent with the Storey & Hummer (1995) implementation of `Case B`. This command was included in the input script used to to create Figure 5. In previous versions of Cloudy we also recommended using the `Case B` command in certain simple PDR (photodissociation region, or photon-dominated region) calculations to block Lyman line fluorescence. As described in § 5.4 below, we now recommend using a different command in the PDR case, reserving the `Case B` command for this purpose only.

The large model reproduces the Storey & Hummer (1995) results to high precision. There are differences at the $\sim 2\%$ level, which we believe to be caused by recent improvements in the collision and recombination data. This will be the subject of a future paper (Guzmán et al. in preparation).

The middle and lower panels show the results of applying our default H I model ($n \leq 10$ resolved with an additional 15 collapsed) to the same density, and to a higher density case. The default model was chosen to reproduce the intensities of the brighter H I lines to good precision. The large red filled circles
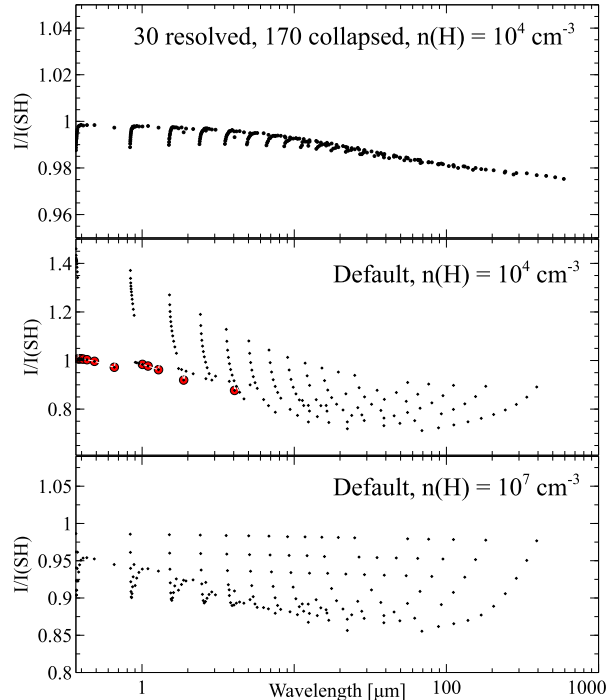
Fig. 5. This shows ratios of our predicted H I emission to the Storey & Hummer (1995) Case B tables. Calculations are for $T_e = 10^4$ K and the indicated densities. The upper panel, our test case `limit_caseb_h_den4_temp4.in.`, shows that we reproduce their results to high accuracy when a large model is used. The default model, chosen as a compromise between speed and accuracy, is shown in the lower two panels. The default model is designed to give higher accuracy for the brighter optical and near-IR lines, plotted as the larger filled circles. Note that each panel has a different vertical scale. The color figure can be viewed online.

in the middle panel indicate lines with intensities greater than 5% that of Hβ. These have deviations of $\lesssim 10\%$.

The eye picks up a trend for the error ratio to move away from unity along a spectroscopic (that is, Balmer, Paschen, etc) series, as the upper level n increases. This is produced by two effects. The first is an "edge" effect as the upper level approaches the upper limit of the model. (We do not report lines arising from $n \geq n_{\mathrm{highest}} - 4$ for this reason.) The level populations for the very highest levels are inaccurate because of their proximity to the large "gap" that exists between the highest level and the continuum above. The errors at lower n are due to the fact that the lower collapsed levels, $10 < n \leq 15$, are not actually l-mixed at the lower density of $10^4\,\mathrm{cm}^{-3}$. The density of $10^7\,\mathrm{cm}^{-3}$ is high enough to l-mix

$n = 11$ so this model is better behaved. These tests show that the implementation gives reliable results when the number of levels is made large enough.

The default model was designed to reproduce the intensities of the brighter H I lines while being computationally expeditious. As a test we computed the intensities of four of the most commonly observed H I lines over the density and temperature given in the Storey & Hummer (1995) tables including the `Case B` command. The ratio of our predictions to their Case B values is given in Figure 6. The largest differences are at the higher densities where Case B would not be expected to apply. These differences are due to recent improvements in the H^0 collision rates. At the lower densities where Case B might apply the agreement is good; the default model is generally within 10% of Storey & Hummer (1995).

This calculation used our `grid` command to compute the required range of density and temperature and the `save linelist ratio` command to save predictions into a file. The input script is

```
set save prefix "nt"
case B
hden 4 vary
grid 2 14 .5 log
constant temperature 4 vary
grid 2.7 4.4 0.05 log
#
stop zone 1
set dr 0
laser 2
ionization parameter 0
init "honly.ini"
save grid ".grd"
save linelist  ratio ".rat" "nt.lines" last no hash
```

The `save linelist ratio` command reads the list of lines in the file `nt.lines` and saves them into the file `nt.rat`. The list of lines in `nt.lines` are ordered pairs and the ratio of intensities of the first to second is reported. (The "#" lines are comments added to aid the user and are ignored.) The predictions in the `nt.rat` file were combined with the grid model parameters saved in the file `nt.grd` to create the plot. The `nt.lines` file contained the following set of line ratios:

```
H  1     4340.49A
Ca B     4340.49A
#
H  1     4861.36A
Ca B     4861.36A
#
H  1     6562.85A
Ca B     6562.85A
#
H  1     1.87511m
Ca B     1.87511m
```

```
#
H  1     2.16553m
Ca B     2.16553m
```

Similar tests can be made for other lines of interest.

The number of resolved levels must be increased when higher precision is needed at low densities (Figure 6) or for faint IR / FIR lines (Figure 5). Figure 4 of Pengelly & Seaton (1964) can be used as a guide in deciding how many resolved levels are needed. Their vertical axis is, in effect, the negative log of the hydrogen density. The lines indicate the critical density, defined in eqn 3.30 of AGN3, where l-changing rates are equal to the radiative decay rate. The l levels within the indicated n will be well mixed when the density is significantly higher than this critical density. For instance, at a density of $10^4 \, cm^{-3}$, the figure shows that the $n = 15$ shell is at its critical density. Our default model uses collapsed levels for $11 \leq n \leq 15$, causing the residuals in the center panel of Figure 5. Our lowest collapsed level, $n = 11$, has a critical density of $\sim 10^{5.5} \, cm^{-3}$. This is why the model is so much more accurate, but still not excellent, at the higher density in the lower panel, $10^7 \, cm^{-3}$.

The user could adjust the model to suit requirements at a particular density using Case B predictions as a guide. We recommend creating a one-zone Case B simulation with a density and temperature set to the conditions under study. Then, adjust the size of the model to achieve the desired accuracy by comparing the lines of interest with the Storey & Hummer (1995) Case B predictions that are included in the output.

Making the model large does come at some cost. Tests show that the test suite example pn_paris, one of the original Meudon meeting test cases (Péquignot 1986), takes ≈ 27s using the default H^0 model on a modern Xeon, while the large model in Figure 5 takes 44m 25s.

3.1.4. *Convergence of Lines onto Radiative Recombination Continua*

As mentioned above, the finite size of the H^0 model is one source of deviations from Case B line predictions in Figure 5. Any finite model will have a "gap" between the highest level and the continuum above. This gap is also present in the predicted spectrum, as shown in Figure 7. This shows the converging high-n Balmer lines and the Balmer jump corresponding to radiative recombination captures to $n = 2$. The upper panel shows the large model used in Figure 5 while the lower is the default model. There is no "gap" in the large model, or in
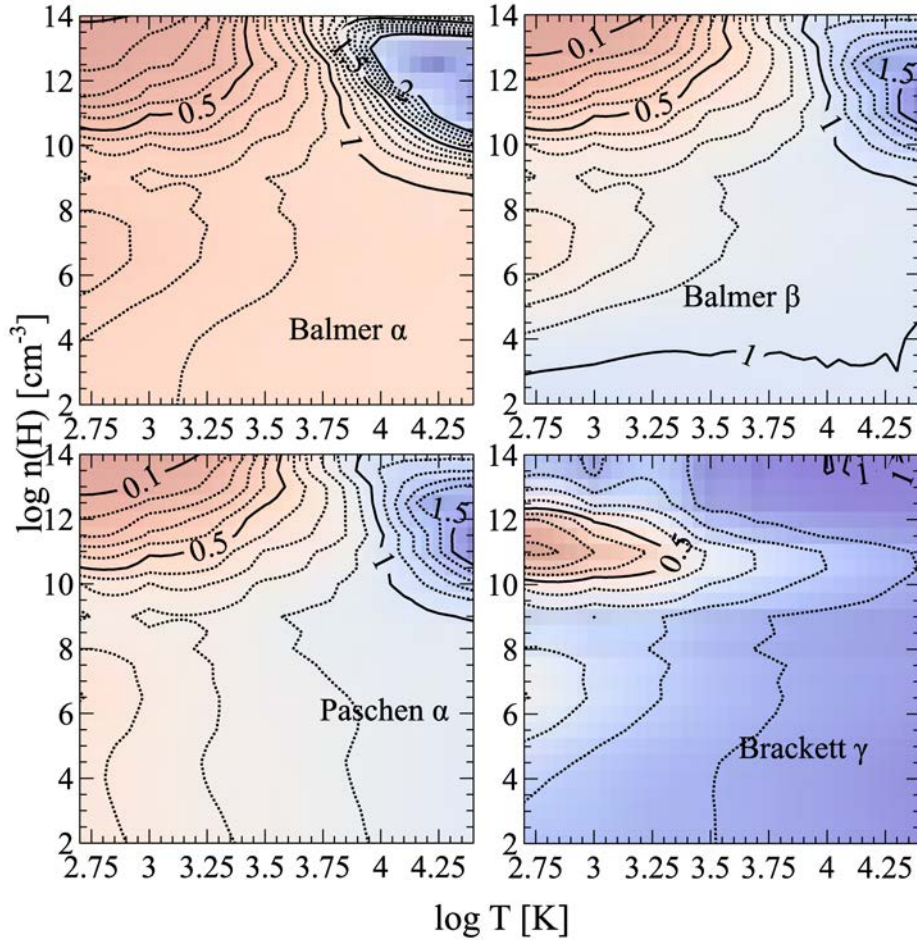
Fig. 6. This shows ratios of our predicted H ɪ emission to the Storey & Hummer (1995) Case B tables for our default H ɪ model. Calculations are for the full temperature and density range they provide. Major contours are at $I/I_{CaseB} = 0.5, 1$, and 1.5 while minor contours, shown as the dotted lines, are at 10% incremental values. The differences at the higher densities are due to the use of more recent collision rates in our calculations.

nature, but rather the Balmer lines merge onto the Balmer jump. This is correct and due to the fact that the oscillator strength is continuous between high-n Balmer lines and the Balmer continuum (Hummer & Storey 1998). The "gap" in the default model is obvious at this high resolution. We note that Schirmer (2016) presents similar figures.

Lyman absorption lines do not suffer from the complexities of H ɪ emission lines since absorption lines depend on the population of the lower level, the ground state in this case. It is then simple to include an arbitrary number of "extra" Lyman lines, lying above the explicit model, so that "gaps" do not appear. An example is shown in Figure 8, a high-resolution blow-up of the spectral region around the Lyman jump. The calculation used our default H^0 model. It is a solar abundance cloud illumi-

nated by our generic AGN SED, with an ionization parameter of $\log U = -2$, a column density of $N(H^0) = 10^{18}$ cm^{-2}, and does not assume Case B. The smooth blending into the Lyman jump is the correct behavior. All iso-sequence models are topped off with these extra Lyman lines.

3.1.5. *The H- and He-like Ions in the X-ray*

The entire H-like and He-like series of ions between H I and Zn XXX are treated with a common code base and have the same commands to change their behavior. Porter & Ferland (2007) discuss the treatment with an emphasis on the changes in the He-like X-ray emission due to UV photoexcitation of the metastable $2\,^3$S level. Mehdipour et al. (2016) compare the X-ray spectral predictions of C13 with the Kaastra (SPEX) and Kallman (XSTAR) codes and find reasonable agreement.
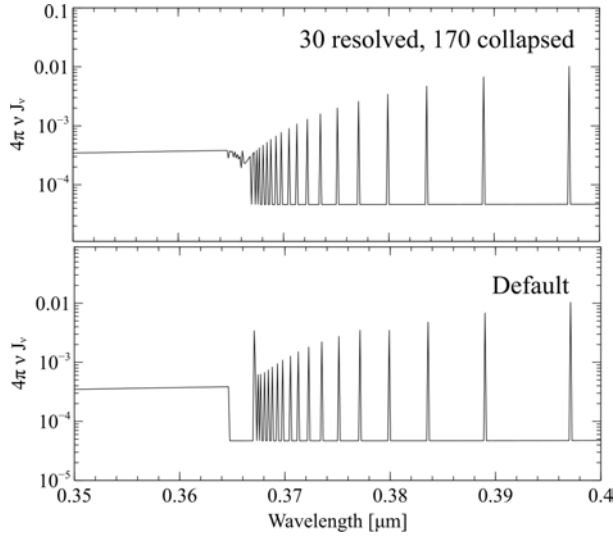
Fig. 7. This compares emission around the Balmer jump for the Case B models used in Figure 5. The continuum resolution is increased by a factor of ten above our default with the command `set continuum resolution 0.1`. The upper and lower panels compare the emission predicted by the large and default models. The large model reproduces the correct smooth merging of the lines and continuum, while the "gap" introduced by the finite size of our default H^0 model is obvious in the lower panel. The color figure can be viewed online.
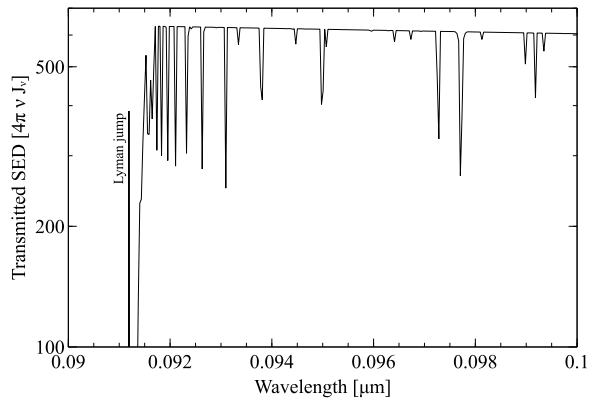
Fig. 8. The transmitted continuum in the region around the Lyman jump is for our default model, which includes "extra" Lyman lines extending to $n = 100$. The high-n Lyman lines merge into the Lyman continuum. The vertical line indicates the wavelength of the Lyman jump. The continuum resolution has been increased by a factor of ten above our default.

The default number of levels for the H-like and He-like iso-electronic sequences are summarized in Tables 2 and 3. The issues discussed above carry over into the X-ray region. Figure 9 shows a small portion
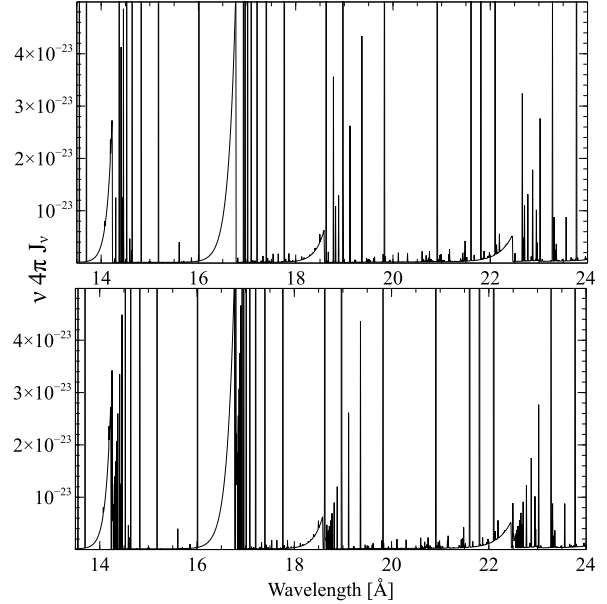
Fig. 9. The emitted spectrum of an optically thin photoionized cloud with solar abundances. The upper panel uses our default models while the lower panel is an enlarged model. The continuum resolution is increased by a factor of ten above our default.

of the emission spectrum of a solar abundance cloud photoionized by our generic AGN continuum. The ionization parameter was adjusted to $\log U = 10^{0.75}$ to insure that C, N, and O were present as H-like and He-like ions.

The "gap" between the recombination edges and the converging Lyman lines is evident in the upper panel. It is larger than in the H I case because we use relatively few levels for these high-ionization species (see Tables 2 and 3). The number of collapsed levels was increased to predict the spectrum in the lower panel. This larger model was computed with the input stream

```
set save prefix "large"
set continuum resolution 0.1
c only include H, C, N, and O, with an increased
c number of collapsed levels
database H-like levels collapsed 20
database He-like levels collapsed 20
table agn
ionization parameter 0.75
hden 0
stop zone 1
set dr 0
iterate
print last iteration
save emitted continuum ".con" last units Angstroms
```

TABLE 2

DEFAULT NUMBER OF LEVELS FOR THE
H-LIKE ISO-ELECTRONIC SEQUENCE

Element	$n(\mathrm{res})$	$nls(\mathrm{res})$	$n(\mathrm{coll})$
H	10	55	15
He	10	55	15
Li	5	15	2
Be	5	15	2
B	5	15	2
C	5	15	5
N	5	15	5
O	5	15	5
F	5	15	2
Ne	5	15	5
Na	5	15	2
Mg	5	15	5
Al	5	15	2
Si	5	15	5
P	5	15	2
S	5	15	5
Cl	5	15	2
Ar	5	15	2
K	5	15	2
Ca	5	15	2
Sc	5	15	2
Ti	5	15	2
V	5	15	2
Cr	5	15	2
Mn	5	15	2
Fe	5	15	5
Co	5	15	2
Ni	5	15	2
Cu	5	15	2
Zn	5	15	5

TABLE 3

DEFAULT NUMBER OF LEVELS FOR HE-LIKE
ISO-ELECTRONIC SEQUENCE

Element	$n(\mathrm{res})$	$nls(\mathrm{res})$	$n(\mathrm{coll})$
He	6	43	20
Li	3	13	2
Be	3	13	2
B	3	13	2
C	5	31	5
N	5	31	5
O	5	31	5
F	3	13	2
Ne	5	31	5
Na	3	13	2
Mg	5	31	5
Al	3	13	2
Si	5	31	5
P	3	13	2
S	5	31	5
Cl	3	13	2
Ar	3	13	2
K	3	13	2
Ca	3	13	2
Sc	3	13	2
Ti	3	13	2
V	3	13	2
Cr	3	13	2
Mn	3	13	2
Fe	5	31	5
Co	3	13	2
Ni	3	13	2
Cu	3	13	2
Zn	5	31	5

The extra levels produce enough lines to fill in the "gap" at this resolution. Regions of significantly increased emission produced by the additional levels are also evident in the larger model.

3.2. A Modified Two-level Approximation for Other Ions

3.2.1. The Two-level Approximation

Textbooks on the interstellar medium (ISM), e.g. Spitzer (1978), Tielens (2005), Osterbrock & Ferland (2006), and Draine (2011), write the ionization balance of an ion as the equivalent two-level system:

$$\frac{n(i+1)}{n(i)} = \frac{\Gamma(i)}{\alpha(i+1)n_e}, \qquad (1)$$

where $n(i+1)$ and $n(i)$ are the densities of two adjacent ionization stages, $\alpha(i+1)$ is the total recombination rate coefficient of the ion (cm^3 s^{-1}) and $\Gamma(i)$ is the ionization rate (s^{-1}). In photoionization equilibrium

$$\Gamma(i) = \int \phi_\nu \sigma_\nu \; d\nu, \qquad (2)$$

where ϕ_ν is the flux of ionizing photons [photons s^{-1} cm^{-2} Hz^{-1}], σ_ν is the photoionization cross section [cm^{-2}] and the integral is over ionizing energies. On the other hand, in collisional ionization equilibrium

$$\Gamma(i) = q(i)n_e, \qquad (3)$$

where $q(i)$ is the collisional ionization rate coefficient.

In its simplest form, the two-level approximation assumes that recombinations to all excited states will eventually decay to the ground state, and that all ionizations occur out of the ground state. Only the ionization rate from the ground state and the sum of recombination coefficients to all excited states need be considered, a great savings in data needs.

This two-level approach extends over to the chemistry. Most codes use databases similar to the UMIST Database for Astrochemistry (McElroy et al. 2013). Reactions between complex molecules are treated as a single channel without detailed treatment of internal structure. In this approximation, rate coefficients do not have a strong density dependence and do not depend on the internal level populations of the molecule. Most of the chemical data needed to implement a more complete model simply do not currently exist.

In some fields, the two-level approximation is called the "coronal" approximation when collisional ionization is dominant. The solar corona has low density and is collisionally ionized. The low densities insure that most of the population is in the ground state and that recombinations to excited states decay to ground. Emission from the solar photosphere is too soft to affect the ionization. CLOUDY has long included a `coronal` command which sets a gas kinetic temperature, informs the code that it is acceptable for no incident radiation field to be specified, and calculates the ionization and emission including thermal collisions and any light or cosmic rays that may also be specified.

3.2.2. The Independent Ionization / Emission Approximation

Together with the two-level approximation, we can further assume that emissions from low-lying levels are not affected by the ionization / recombination process, so that they can be treated as separate problems. As examples, the C IV $\lambda 1549$, Mg II $\lambda 2978$, and [O III] $\lambda\lambda$ 5007, 4959 multiplets are produced by the lowest excited levels of their ions in Figure 3. These levels are much closer to ground than to the continuum, so they should be most directly coupled to the ground state. The fact that, at low particle and photon densities, nearly all of the population of a species is in the ground state, further justifies this assumption.

This "independent ionization / emission" approximation (IIEA) is also suggested from consideration of the relevant timescales. Consider the simple model of the Orion Nebula described by Ferland et al. (2016). The recombination time of a typical ion is ≈ 7 yr at a density of $n \approx 10^4$ cm^{-3}. Electrons tend to be captured into highly excited states, which have lifetimes of about 10^{-5} s to 10^{-8} s, so the electron quickly falls down to the ground state. The electron remains in the ground state for about five hours before another ionizing photon is absorbed and the process starts again.

Line-emission timescales are much faster, with collisional excitation timescales of $\approx 10^5$ s at a density of 10^4 cm^{-3} and photon emission occurring within $\tau \approx 10^{-7}$ s for a typical permitted transition. Collisional / emission processes within the low-lying levels occur on timescales that are $\tau \geq 4$ dex faster than ionization – recombination. As a result, most codes first solve for the ionization distribution of an element, then for the line emission from each ion. They are treated as separate problems.

This is equivalent to the use of photo-emission coefficients (PEC), introduced by Summers et al. (2006) and commonly used in fusion plasmas. The line emissivity for a transition between excited levels i and j can then be expressed as $\text{PEC}^{(\text{exc})}_{\sigma, i \to j} n_\sigma$, where the excited levels i and j are assumed to be in equilibrium with the ground or metastable state σ. Here, $\text{PEC}^{(\text{exc})}_{\sigma, i \to j} = A_{i \to j} \mathcal{F}^{(\text{exc})}_{i\sigma}$ is the excitation photo-emission coefficient for the $i \to j$ transition, where $\mathcal{F}^{(\text{exc})}_{i\sigma}$ accounts for the collisional-radiative excitation to level i from σ.

Systems with an especially complex structure, such as Fe II, are a major exception to the discussion so far. Fe II has levels extending, nearly uniformly, between the ground state and the continuum, as shown in the right of Figure 3. The atomic physics of Fe II is especially complex due to the fact that it has a half-filled d shell, combined with the near energy degeneracy of the 3d and 4s electrons. Unfortunately Fe II emission is strong in a number of astrophysically important classes of objects, including quasars and shocked regions. This is a worst case, with our treatment discussed by Verner et al. (1999).

The remainder of this section discusses our implementation of a modified two-level approximation for many-electron systems. The following section discusses our treatment of the bound levels and their emission.

3.2.3. Ionization / Recombination Rates

Our sources for ionization and recombination data for many-electron systems are summarized in C13. Ground and inner-shell photoionization cross sections are given by Verner et al. (1996), and summed recombination rate coefficients are com-

puted as in Badnell et al. (2003), Badnell (2006), and are listed on Badnell's web site[14].

We have long used collisional ionization rate coefficients presented by Voronov (1997). Two recent studies, Dere (2007) and Kwon & Savin (2014), have presented new rate coefficients for collisional ionization of some ions. These studies are in very good agreement with Voronov (1997) for temperatures around those of the peak abundance of the ion. Unfortunately, the fitting equations used by Dere (2007) and Kwon & Savin (2014) only return positive values for temperatures around the peak abundance of the ion in collisional ionization equilibrium. The Voronov (1997) fits are well behaved over the full temperature range we cover, 2.7 K to 10^{10} K.

As described by Lykins et al. (2013), we improved the Voronov (1997) fits by rescaling by the ratio of the new to Voronov values at temperatures near the peak abundance of the ion. This correction was usually small, well bellow 20%, so has only modest changes in results.

3.2.4. *Collisional Suppression of Dielectronic Recombination (DR)*

Dielectronic recombination (DR), a process where a free electron is captured by exciting a bound electron, forming an autoionizing state that can decay into bound levels, is the dominant recombination process for most many-electron ions. We mainly use data from Badnell[15], which is also the largest collection available for this process.

Energetically, the DR process occurs via levels with energies within kT of the ionization limit, so, as shown in the center of Fig 3, it will mainly populate levels that are close to the ionization limit. Of the ions shown in the Figure, only O III has low-lying autoionizing levels, the levels above the ionization limit. For many ions, experimental data for such low-lying autoionizing levels are either completely missing or incomplete. The summed DR rates listed on the Badnell web site assume that all these populations eventually decay to the ground state, an approximation that must fail at high densities, as quantified below.

It has long been known that DR is suppressed by collisional ionization at moderate to high densities (Sunyaev & Vainshtein 1968; Burgess & Summers 1969; Davidson 1975). Nikolić et al. (2013) extended previous work to estimate the extent of this suppression for various iso-electronic sequences. Their figure

7 shows that the ionization of low stages of iron can change by nearly 1 dex at densities of $\approx 10^{10}$ cm^{-3} when suppression is included. As stressed in that paper, these results are highly approximate, with the uncertainty in the suppression being of order the correction itself. A full solution of the populations of the excited states must be done to get the right answer (Summers et al. 2006). Such corrections do allow the two-level approximation to be applied at higher densities, although with this uncertainty.

Nikolić et al. (2017, in preparation) revisited the problem and estimated new suppression factors that offer an improvement over the 2013 values. We use those suppression factors in this release of Cloudy.

3.2.5. *Limits of the Two-Level Approximation for the ionization*

Over what density range is the two-level approximation valid? How does it fail outside this range? Despite the wide application of this approximation, we do not know of a discussion of these questions.

The two-level approximation will fail when highly excited states do not decay to the ground, most often due to collisional ionization at high densities. Highly-excited levels are long lived due to smaller spontaneous decay rates; for hydrogenic systems the lifetime scales as $\tau \propto n^5$ (He et al. 1990). At the same time, the cross section for collisions increases for higher levels as n^4. So, compared to electrons in low levels, those in highly excited levels decay to lower levels slowly, and a large probability for collisional ionization is the result. Further, at high density and temperature the highly-excited levels of all ions will have significant populations, related to the well-known divergence of the partition function in stellar atmospheres (Hubeny & Mihalas 2014). Collisional ionization from excited states becomes important, and the use of summed recombination coefficients becomes highly approximate, so both the two-level approximation and "independent ionization / emission" assumptions break down.

We can use our complete CRM solutions for the H- and He-like isoelectronic sequences to show where the two-level approximation fails. In Figure 10 we consider the ionization of hydrogen in a collisionally ionized gas at the indicated temperature, shown over a very wide range of density. The Figure, based on one shown in Wang et al. (2014), shows how collisional-radiative effects, mainly involving highly excited levels, cause the hydrogen ionization to go from coronal equilibrium at low-densities to local thermodynamic equilibrium (LTE) at high densities. Figure 5 of Summers et al. (2006) shows a somewhat

---

[14]see http://amdpp.phys.strath.ac.uk/tamoc/RR/, http://amdpp.phys.strath.ac.uk/tamoc/DR/

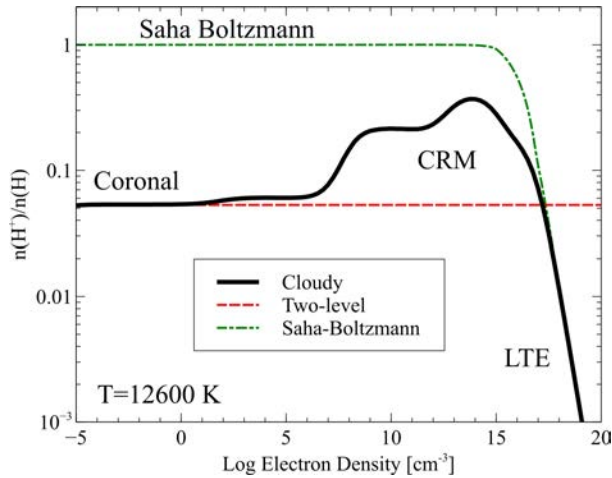[15]http://amdpp.phys.strath.ac.uk/tamoc/DR

Fig. 10. Ionization of hydrogen as a function of density. The low-density coronal approximation limit occurs on the left, while the thermodynamic statistical equilibrium limit applies at high densities. The solid black line is the full numerical CRM solution, the red dashed line is the ionization predicted by the two-level approximation, and the dashed-dotted line is the prediction of the Saha-Boltzmann equation. The color figure can be viewed online.

similar effect. The kinetic temperature was chosen so that the gas would be partially ionized at the lowest densities, so that a wide range in ionization can result.

In the low-density limit, the solution to the coronal equilibrium two-level system given by Equation 1, is

$$\frac{n(i+1)}{n(i)} = \frac{n_e q(i)}{n_e \alpha(i+1)} = \frac{q(i)}{\alpha(i+1)}, \qquad (4)$$

where $n(i+1)$ and $n(i)$ are the densities of the ion and atom, and n_e is the electron density, which cancels out. The two-level solution is given as the red-dashed line in Figure 10. It does not depend on density since the electron density cancels out when collisional ionization and recombination are in balance. It does have an exponential dependence on temperature, as does the Saha-Boltzmann equation described next, because of the exponential Boltzmann factor that enters in the collisional ionization rate coefficient, $q(i)$.

In the high-density limit, as might be found in lower parts of some stellar atmospheres, accretion disks near black holes, or certain laboratory plasmas, the gas comes into LTE and the ionization balance is given by the Saha-Boltzmann equation:

$$\frac{n(i+1)}{n(i)} = \frac{g_e}{n_e} \frac{(2\pi m k T)^{3/2}}{h^3} \frac{u(i+1)}{u(i)} \exp(-\chi_i/kT)$$
$$(5)$$

where g_e is the electron statistical weight, the u's are partition functions, and χ_i is the ionization potential of the atom (Chandrasekhar 1960; Hubeny & Mihalas 2014). In this limit, shown as the green dashed-dotted line in Figure 10, the ionization depends exponentially on the temperature and inversely linearly on the electron density. At the microphysical level this can be understood as a balance between collisional ionization, $n(i) + e \rightarrow n(i+1) + 2e$, and three-body recombination, $n(i+1) + 2e \rightarrow n(i) + e$, the inverse process.

The black line in Figure 10 shows the CLOUDY collisional-radiative solution. It goes between the coronal approximation, equation 4, valid at $n \lesssim 10^7$ cm^{-3}, and the Saha-Boltzmann limit at high densities, equation 5, valid at $n \gtrsim 10^{16}$ cm^{-3}. The density ranges where the coronal, CRM, and LTE limits apply are indicated by the labels.

Many sources, such as the Orion Nebula or planetary nebulae, are safely in the limit where the two-level approximation holds, and lower regions of the solar atmosphere or accretion disks are dense enough to be in LTE. However, many regions, including the emission-line clouds in quasars, or the upper layers of accretion disks, have intermediate densities, where neither approximation holds. This is the density range over which full collisional radiative models must be applied. The density is high enough for collisional ionization from excited levels to be important. Indeed, the modest increase in ionization at densities of $\approx 10^3$ cm^{-3} is caused by collisional ionization from the metastable $2s$ level, which is highly over-populated due to its small radiative decay rate. At high densities, the ionization increases as the density increases and collisional ionization from more highly-excited levels becomes more important. Eventually, when collisional ionization and three-body recombination come into balance, the atom comes into LTE (Seaton 1964).

For more highly-charged ions, the scaling introduced by charge dependencies means their populations also will behave much like Figure 10, but at considerably higher densities. For hydrogenic systems, the lifetime of a level goes as $\tau \propto Z^{-4}$ (Summers et al. 2006), and the energy χ, to ionize a level n, varies as Z^2. Because of this, we expect the two-level approximation to apply at higher densities for more highly-charged ions.
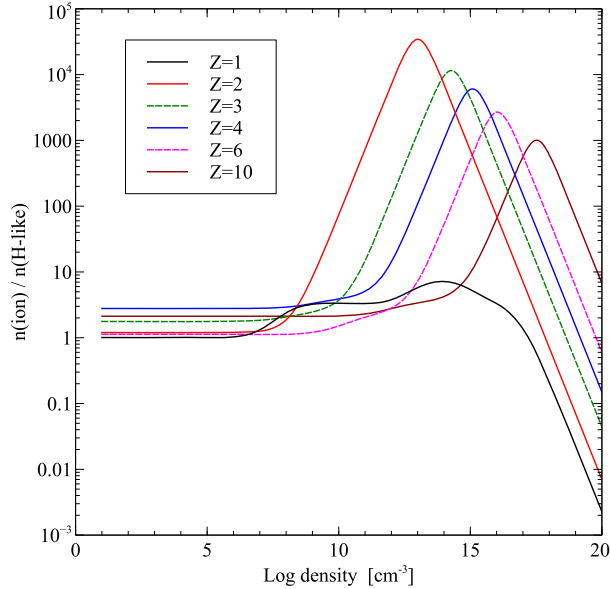
Fig. 11. Density ratio of fully-ionized to single-electron species as a function of electron density. The plot is for different elements with nuclear charge indicated. The effects of increasing charge on the range of validity of the coronal and LTE limits are dramatic.

We quantify this in Figure 11. This shows a plot of the ratio of densities of the fully-ionized to single-electron ions that is very similar to Figure 10, but for different elements, indicated by the nuclear charge Z. Here, the Z^7 scaling of density effects can be seen on the shift in peak densities on going from $Z = 2$ to 10. For each element we have chosen a temperature so that the ratio of ion densities at the low-density limit is $\approx$1–5.

The Cloudy test suite includes a series of example programs which drive Cloudy in various applications. One such test, `collion`, creates tables giving the ionization balance in the low-density collisional-ionization limit. These are formatted to be very similar to the tables in Carole Jordan's classic paper (Jordan 1969). An example, for helium, is given as Table 4. The first column gives the log of the gas kinetic temperature, while the remaining columns give the logs of the fractional abundances of He^0, He^+, and He^{2+}. Only portions of the full temperature range are shown. Such tables, covering the lightest 30 elements and our full temperature range, are present in the `cloudy/tsuite/programs/collion` folder. These tables were consulted to choose the kinetic temperature that resulted in the appropriate low-density limit ionization.

A typical input script, for $Z = 10$, is:

TABLE 4

COLLISIONAL EQUILIBRIUM IONIZATION FRACTIONS

Log Te [K]	He	He+1	He+2
3.00	0.00	–	–
3.10	0.00	–	–
⋮	⋮	⋮	⋮
3.90	0.00	–	–
4.00	0.00	–	–
4.10	-0.00	-6.45	–
4.20	-0.00	-3.93	–
4.30	-0.00	-2.16	–
4.40	-0.07	-0.81	-8.73
4.50	-0.55	-0.15	-5.71
4.60	-1.35	-0.02	-3.70
4.70	-2.07	-0.01	-2.16
4.80	-2.67	-0.05	-0.97
4.90	-3.33	-0.34	-0.26
5.00	-4.15	-0.95	-0.05
⋮	⋮	⋮	⋮
7.00	–	-5.89	-0.00
7.10	–	-6.00	-0.00
7.20	–	-6.11	-0.00
⋮	⋮	⋮	⋮
8.70	–	-7.78	0.00
8.80	–	-7.90	0.00
8.90	–	-8.02	0.00
9.00	–	-8.14	0.00

```
set save prefix "z10"
init "honly.ini"
element neon on
database H-like levels collapsed 50
database He-like levels collapsed 50
database H-like continuum lowering off
database He-like continuum lowering off
hden -5
element neon  abundance 5
coronal, temperature 6.8
eden 1 vary
grid 1 20 .25
stop zone 1
set dr 0
save element neon ".ion" last no hash
save grid ".grd" last no hash
```

This script first "turns off" all elements except hydrogen, to save time, then turns neon, $Z = 10$, back on. Next, the number of collapsed levels is increased to improve the precision of the solution. The `database H-like neon` and similar commands give the iso-electronic sequence and element to change the treatment of particular species. Neon is given a very large abundance, 10^5 times that of hydrogen, to prevent H - Ne charge exchange from affecting the ionization balance. This model is not in charge equilibrium since the electron density is set with the `eden`

TABLE 5

DENSITIES FOR CORONAL AND LTE LIMITS

Charge	$T_{kinetic}$ [K]	n(Coronal) [cm^{-3}]	n(LTE) [cm^{-3}]
1	1.2×10^4	$\lesssim 10^7$	$\gtrsim 10^{16}$
2	7.9×10^4	$\lesssim 10^8$	$\gtrsim 10^{14}$
3	2.2×10^5	$\lesssim 10^{10}$	$\gtrsim 10^{15}$
4	5.2×10^5	$\lesssim 10^{11}$	$\gtrsim 10^{16}$
6	1.3×10^6	$\lesssim 10^{12}$	$\gtrsim 10^{17}$
10	6.3×10^6	$\lesssim 10^{14}$	$\gtrsim 10^{18}$

command. This is used to show one way of driving Cloudy. The `grid` command was used to vary the electron density over a wide range. We set the temperature to $\log T = 6.8$ with the `coronal` command, to produce the desired ionization at low densities. Table 5, which summarizes results, lists the chosen temperature for each charge. The model is in collisional ionization equilibrium so the temperature is, in the simplest case, the only important parameter. The two `save` commands produce files that were later used to create the Figures. Continuum lowering is treated following Bautista & Kallman (2000) and is disabled with the command `database H-like continuum lowering off`.

The shift of the CRM peak to higher densities for higher Z is dramatic, and is a result of the changing lifetimes, level energies, and collisional rate coefficients, as described above. Table 5 indicates approximate density limits over which the coronal and LTE limits apply. We choose the lower limit where the ratio was higher by $\approx 30\%$ than the value at the lowest density. The LTE limit was chosen as the density when the solution goes over to the asymptotic Saha-Boltzmann power-law. The actual results do depend on the chosen temperature. The values in the Table are highly approximate and only intended to serve as a guide.

The photoionization case behaves quite differently from the collisional case. In collisionally-ionized plasmas the peak abundance of an ion with ionization potential IP occurs at temperatures roughly equal to the IP (Jordan 1969). At these temperatures, collisions can fully populate all levels from the ground state (see Figure 3) so the populations of excited levels are far larger than for a photoionized plasma. Collisional ionization out of these levels produces the CRM peak seen in Figures 10 and 11.

We computed a series of photoionization models for the same elements, density range, and ioniza-
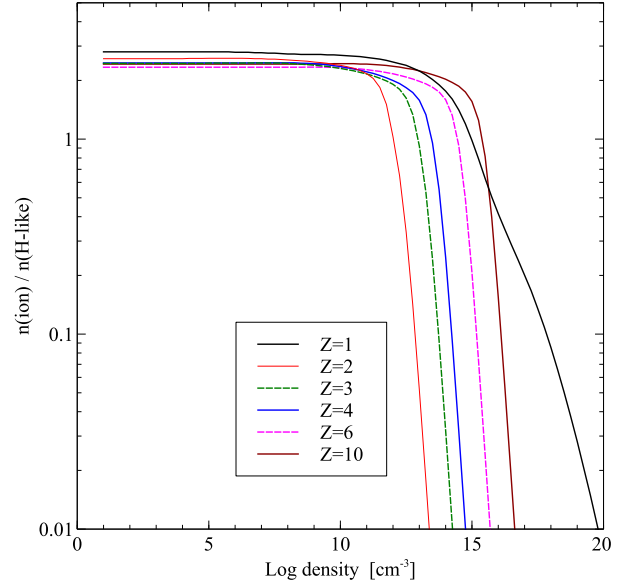
Fig. 12. As in Figure 11, but for the photoionization case. The CRM peak, prominent in Figure 11 and produced by collisional ionization from highly-excited levels, is not present because the Rydberg levels that enhance the ionization have a smaller population in photoionization equilibrium.

tion ratio, with results shown in Figure 12. The gas is illuminated by a blackbody with a temperature $T_{BB} = 2 \times 10^4 \times Z^2$ K. The ionization parameter (AGN3, eqn 14.7) was adjusted to establish the desired ionization ratio in the low-density limit. The gas kinetic temperature, which plays a minor role in establishing the ionization, was set to values typical of the ionization parameter.

The input scripts that produced this figure were similar to:

```
set save prefix "z10"
init "honly.ini"
element hydrogen ionization -9 0
element neon on
element neon abundance -2
hden -5 vary
grid 1 20 .25
constant temperature 2e5 K
blackbody 2e6
ionization parameter 0.3
database H-like neon levels collapsed 50
database He-like neon levels collapsed 50
database H-like continuum lowering off
database He-like continuum lowering off
stop zone 1
set dr 0
save element neon ".ion" last no hash
save grid ".grd" last no hash
```

TABLE 6

DENSITIES FOR PHOTOIONIZATION
CORONAL LIMIT

Charge	Coronal $[\,\mathrm{cm^{-3}}]$
1	$\lesssim 10^{10}$
2	$\lesssim 10^{10}$
3	$\lesssim 10^{12}$
4	$\lesssim 10^{14}$
6	$\lesssim 10^{16}$
10	$\lesssim 10^{16}$

Many of the commands are similar to the collisional ionization case. This example shows a second way to vary the electron density over the desired range. Only H and Ne are included in the model, and Ne has a modest abundance. The hydrogen ionization fraction is set so that the H^0 density is 10^{-9} smaller than the total hydrogen density.

The CRM peak is not present because excited levels are not overpopulated at these lower temperatures. The decreasing ionization at high densities is produced by three-body recombination bringing higher levels into LTE. Table 6 gives the density limit for the two-level approximation to be valid. This is taken as the density where the ionization ratio has fallen by 30%. As also happened in Table 5, hydrogen behaves differently because electron - atom collision rate coefficients are so much smaller than electron-ion rate coefficients.

Tables 5 and 6 are meant as an indication of where our methods of solving for the ionization of many-electron systems will fail. The ranges of validity are highly approximate for several reasons. The collisional ionization results are sensitive to the gas kinetic temperature while the photoionization predictions depend on the SED shape. Further, we only have complete CRM models, extending to high Rydberg levels, for one and two-electron systems. The energy level structure, as shown in Figure 3, does not resemble the structure of many-electron systems, which tend to have a higher density of levels with low energies.

We are working to incorporate the CRM methods developed by the laboratory plasma community to have a better representation of the highly excited levels. A number of physics codes have been developed, mainly in support of experimental facilities, to do just that. Many are summarized in the NLTE7 and NLTE9 code-comparison workshop summaries

of Chung et al. (2013) and Piron et al. (2017). Few of these codes are openly available. The ADAS data collection, part of the ADAS code described by Summers et al. (2006), is available through the OPEN-ADAS[16] portal, and the FLYCHK code of Chung et al. (2005) is hosted at NIST[17].

4. ATOMS AND IONS

The greatest changes to our treatment of atoms and ions involved the move to large databases, as described in § 2, and the development of our Stout database (Lykins et al. 2015). This section describes other advances, mainly involving Gaunt factors.

Gaunt factors, named after John Arthur Gaunt, are corrections to classical electron-ion interaction theory to incorporate quantum results (Garstang 1993). Three Gaunt factors are encountered (Menzel & Pekeris 1935; Aller 1963). Following the Menzel & Pekeris (1935) numbering and Chandrasekhar's notation (Chandrasekhar 1957), g_I corrects bound-bound transitions, g_{II} describes free-bound processes and is discussed in § 4.2 below, while g_{III} adjusts free-free or bremsstrahlung emission and is discussed in the next section. Burgess & Summers (1987) summarize numerical methods of calculating radiative Gaunt factors for complex ions.

4.1. *Free-Free Gaunt Factor* g_{III}

Free-free or bremsstrahlung emission is the dominant coolant at high temperatures, is usually the main contributor to radio emission in nebulae, and can produce emission across the full electromagnetic spectrum if the gas is hot enough. As Figure 5.2 of Rybicki & Lightman (1979) shows, different ranges of temperatures and photon energies require different asymptotic expressions for g_{III}. These approximations do not join continuously with one another. For this reason, it is not possible to use such expansions across the full temperature and spectral range we cover with Cloudy.

van Hoof et al. (2014) derived averaged and wavelength-specific free-free Gaunt factors g_{III}, limited to non-relativistic energies. This work was extended by van Hoof et al. (2015) to include parameters where relativistic effects were important. Results from both studies were presented as tables that can be downloaded, and these are now used by Cloudy to predict free-free emission.

Values of g_{III} covering the full range of kinetic temperature, photon energy, and nuclear charge considered by Cloudy are shown in Figure 13. As is

---

[16]http://open.adas.ac.uk/
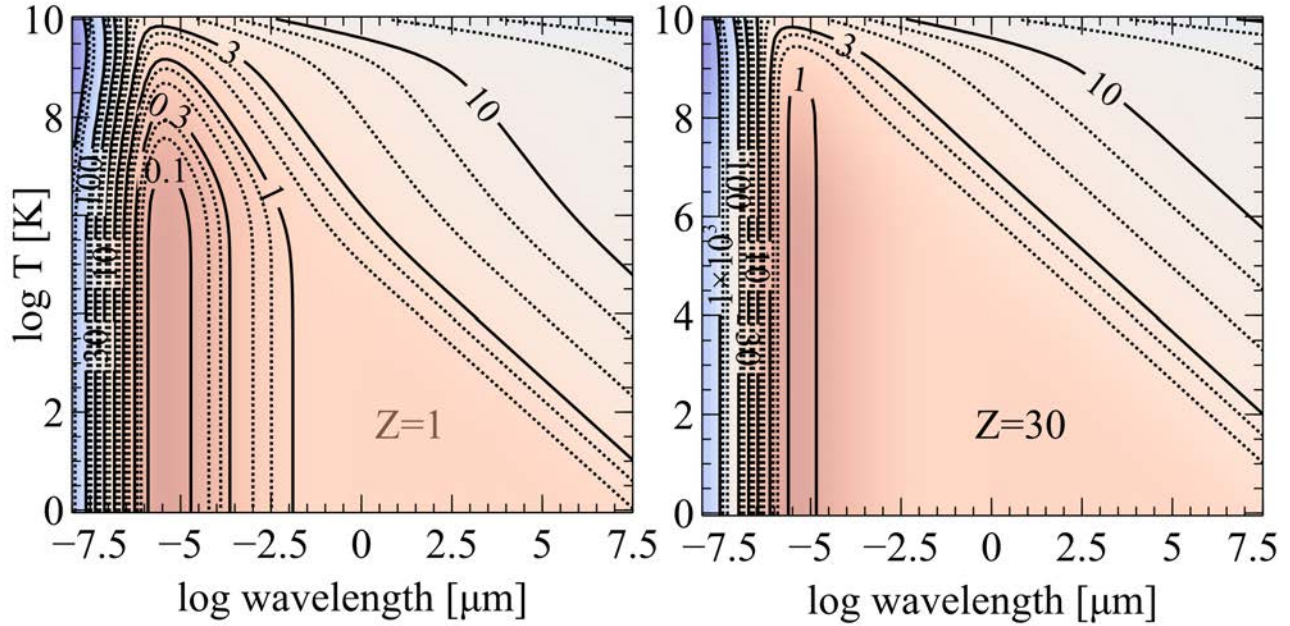[17]http://nlte.nist.gov/FLY/

Fig. 13. Values of the g_{III} Gaunt factor over the full wavelength, temperature, and nuclear charge range CLOUDY considers.

well known, $g_{III} \approx 1$ across "nebular" temperatures and UV, optical, and NIR wavelengths. The closeness to unity shows that emission is roughly classical over these parameters. We see that g_{III} initially drops below 1 towards shorter wavelengths. But then, at yet shorter wavelengths, it starts rising towards infinity when the relativistic effects become important. We also see that $g_{III} > 1$ at long wavelengths, which is the well-known non-relativistic result for radio emission. The values depend on nuclear charge, as shown by comparing the left panel, for hydrogen ($Z = 1$), and the right panel, for zinc ($Z = 30$). This is because the relativistic effects break the simple Z-scaling that exists in non-relativistic calculations. As explained in the original papers, we believe that these values are highly accurate.

4.2. *Free-Bound Gaunt Factors g_{II}*

Rate coefficients for radiative recombination are derived from the photoionization cross section, using detailed balance, often called the Milne relation (see, for instance, Appendix 2 of AGN3). The g_{II} factor allows classical expressions for the photoionization cross section to be used to obtain accurate recombination rate coefficients.

Seaton (1959), hereafter S59, derived hydrogenic radiative recombination rate coefficients over a broad range of temperature using the g_{II} ap-

proach. Sutherland & Dopita (1993), hereafter SD93, claimed that this work was numerically flawed and offered corrections to Seaton's theory. One of us has revisited the theory of hydrogenic radiative recombination twice (Ferland 1980; Ferland et al. 1992), referred to as F80 and F92, and found only excellent agreement with S59, so this claim is puzzling.

We use a finite model to approximate the internal structure of H^0, so we need to "top off" the model by accounting for the difference between the infinite-level total radiative recombination and the summed recombination to the modeled levels. This requires accurate Case B recombination coefficients over a very broad temperature range. This brings up the SD93 correction to the S59 theory. SD93 is *very* highly cited, and its results are widely used, so it is important to understand whether there is a problem in S59.

S59 developed analytical expansions, in the small- and high-temperature limits, of quantities that enter into g_{II}. No analytical expansion was possible at intermediate energies and direct numerical integration was performed instead. S59 presented the expansions as equations and the numerical results as tables. S59 estimated the errors due to the high-temperature expansion to not exceed 2% for $T \leq 10^4$ K, and that they increased for higher temperatures.
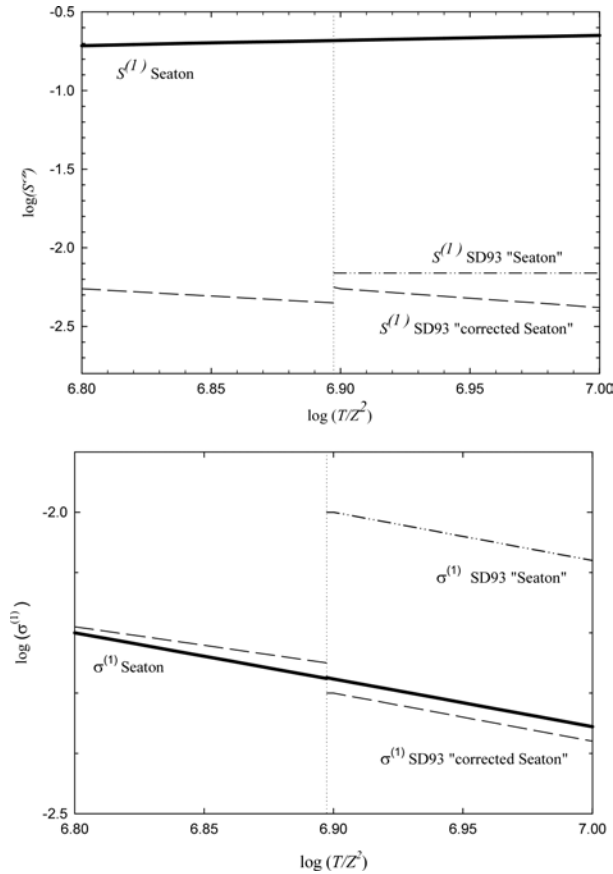
Fig. 15. Hydrogenic recombination rate coefficients are shown vs. reduced temperature, T/Z^2, for the ground state, $n = 1$. The vertical dotted line marks the SD93 discontinuity, where the theory changes from the numerical to analytical forms. The dash-dotted line gives SD93's evaluation of the Seaton rate, taken from the upper panel of their Figure 1. The dashed line is SD93's "corrected Seaton" theory. The heavy solid line gives our recalculation of the rates using Seaton's original expressions and tables. All the rates are multiplied by the reduced temperature.

Fig. 14. This shows two of the quantities that enter into the S59 calculation of g_{II}. The vertical dotted line marks the point where SD93 claim that Seaton's theory is discontinuous. The dashed-dotted lines give the quantities plotted in the lower panel of Figure 1 of SD93. The dashed curves give SD93's "corrected Seaton" theory. The heavy solid lines give our recalculation of the terms S and σ using Seaton's original expressions and tables.

SD93, § 3.4.1 and Figure 1, report that the S59 intermediate-temperature numerical, and high-temperature analytical, results do not smoothly join one another, and offer an alternative expression for the high-temperature part. We show results from their tables and figure as our Figures 14 and 15. Figure 14 shows one of the S59 intermediate results taken from their tables. The line marked "SD93 Seaton" is their version of S59 while "corrected Seaton" is their altered version. F80 closely followed S59, so we have some experience in working with this paper. The heavy line is our evaluation of S59. It is continuous and somewhat displaced from SD93.

Figure 15 compares total recombination rate coefficients over the narrow temperature range where SD93 report problems. The discontinuities are obvi-

ous. The heavy line is our evaluation of S59. It is continuous and displaced from SD93.

Figure 16 shows total recombination rate coefficients over a broad range of temperature. The heavy line gives our reevaluation of the Seaton results. S59 notes that his expressions are not valid above 10^6 K and the heavy line ends at that temperature. The lines marked "Mappings I" and "corrected Seaton" are taken from SD93. The line marked "Mappings I" is an extrapolation of the S59 expression as used by Arnaud & Rothenflug (1985) and the Mappings I code. The line marked "corrected Seaton" is the expression proposed by SD93.

Today the g_{II} approach is seldom used because large repositories of photoionization cross-sections, such as the Opacity Project (Seaton 1987), are readily available, so the Milne relation can be applied directly to photoionization cross sections. F92 took this approach. The F92 results are believed to be of high accuracy for all temperatures presented, as was recently confirmed by Mao et al. (2017). S59 reported that his results should be "in error by less than 0.5 per cent for $(T/Z^2) \leq 10^5$ K, by 3 per cent for $(T/Z^2) = 10^6$ K and by 31 per cent for $(T/Z^2) = 5 \times 10^6$ K." F92 confirms these error estimates.

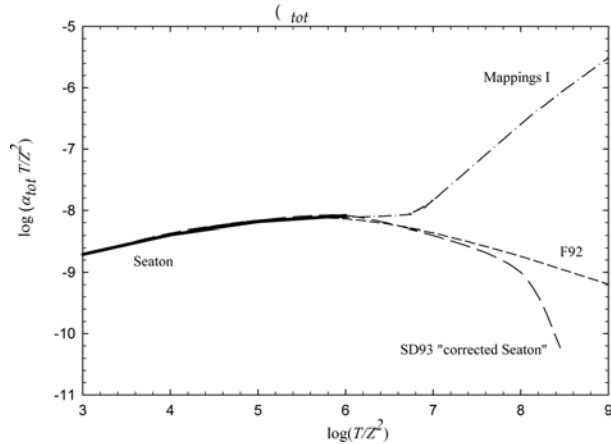Fig. 16. Comparison of various hydrogenic total Case B recombination rate coefficients. Our reevaluation of Seaton's theory is shown as the heavy solid line drawn over the temperature range where he said it was applicable. The dot-dashed line gives the rate used in Mappings I, equation (7) of SD93. The SD93 "corrected Seaton" rate is shown as the long dashed line. The short dashed line gives the F92 rates derived by direct numerical integration of the Milne equation over hydrogenic photoionization cross sections. The F92 curve lies behind the Seaton curve for $T < 10^6$ K, the temperature range he indicated the theory was accurate. All rate terms are multiplied by a factor of T/Z^2.

Our models of the H- and He-like isoelectronic sequences require level-resolved recombination rate coefficients and photoionization cross sections. We now use hydrogenic expressions, for H-like, or results from the Opacity Project as described by Porter et al. (2012), to obtain the needed data. But we use F92 to provide the correction needed to "top off" the hydrogenic systems. We believe that this is the correct approach and do not use the SD93 theory.

5. THE GRAIN AND CHEMICAL MODELS

Our treatment of the chemistry and molecular emission is described in C13, Abel et al. (2005), Shaw et al. (2005), and Abel et al. (2008). Grain physics, which has a great impact on the chemistry, is described by van Hoof et al. (2004), while Abel et al. (2005) outlines how we do ionization / recombination of ions on grain surfaces.

5.1. H_2 formation on Grain Surfaces

The treatment of H_2 formation via catalysis on grain surfaces due to chemisorption and physisorption, the Eley - Rideal mechanism (Le Bourlot et al. 2012), has been modified since C13. Our revised treatment incorporates the rates from Cazaux & Tielens (2002, 2004), including the corrections of Cazaux & Tielens (2010). Our implementation of the Cazaux & Tielens rates utilizes equations C1, C2, and C3 given in the appendix of Röllig et al. (2013). However, while comparing the latter paper to the Cazaux & Tielens work, two typesetting errors in equation C2, which describes chemisorption, were found, as confirmed by private communications with the authors. First, the entire right side of equation C2, not just the 2F term, should be raised to the -1 power. The second error in C2 involves the exponential dependence of the H_2 formation rate on the desorption energy of chemisorbed hydrogen, which should have a negative sign.

The new rates were first used in the chemical modeling of Orion's Veil (Abel et al. 2016), a low H_2 abundance environment where the revised rates were expected to have the greatest impact through increased H_2 formation (Le Bourlot et al. 2012). However, since most of the increased rate occurs on PAHs (polycyclic aromatic hydrocarbons, Röllig et al. 2013) and since small grains are largely absent in the Veil, the effects on the H_2 abundances were found to be less than 10%.

5.2. H_2 Collisions and H_2, HD Cooling

Our complete H_2 model is described by Shaw et al. (2005). We include three datasets for H_2 – H^0 collisions, as controlled by options on the command `database H2 collisions`. The default is to use the rates given by Wrathmall et al. (2007). The rates given by Le Bourlot et al. (1999) are also available. The recent dataset, Lique (2015), which includes ortho-para-changing reactive collisions, is available in this release, although Wrathmall et al. (2007) remains the default. The H_2 cooling is the explicit sum of the difference between the collisional excitation and deexcitation rates given in Equation 7 below.

We fall back on simple and approximate models of H_2 formation and cooling when our complete H_2 model is not used. Our model of the dissociation physics is inspired by the Tielens & Hollenbach (1985) H_2 model and is described by Elwert et al. (2005). H_2 cooling is approximated with the function given by Glover & Abel (2008). HD cooling is given by Flower et al. (2000). There are cases where these are significantly different from the approximations used in C13.

5.3. How does the PAH Abundance Vary Across the H^+, H^0, and H_2 Regions of a Nebula?

CLOUDY can consider the adjacent H^+, H^0, and H_2 regions of a nebula, the so-called H II region, PDR, and molecular cloud. This brings in questions

concerning how the PAH abundance changes across these regions. Observations of the Orion Bar originally showed (Sellgren et al. 1990) that PAHs emit in a narrow region that might most closely be associated with the H^0 region (AGN3 § 8.5). The obvious interpretation is that PAHs are destroyed in the H^+ region of the nebula. The lack of PAH emission at deeper, more molecular, regions of the PDR could be due to a lack of PAHs in H_2 regions, or simply an illumination effect, where PAHs do not fluoresce because UV light does not penetrate into the well-shielded high A_V regions where H_2 is found. This is an area of active research

We provide three options to describe how the PAH abundance varies with physical conditions. These are controlled with the commands:

```
set PAH constant
set PAH "H"
set PAH "H,H2"
```

The `constant` option will keep the PAH abundance constant across the H^+, H^0, and H_2 regions. This allows PAHs to exist in the H^+ region. We do this for completeness, even though observations suggest that PAHs are not present there. The `"H"` option will scale the PAH abundance as the atomic hydrogen fraction, $n(\mathrm{PAH}) \propto n(\mathrm{H})/n_\mathrm{total}$, where n_total is the total density of hydrogen in all forms. This is the simplest interpretation of the Orion Bar observations. The `"H,H2"` option will scale the PAH abundance as the fraction of hydrogen that is either atomic or molecular, $n(\mathrm{PAH}) \propto [n(\mathrm{H}) + 2n(\mathrm{H_2}))]/n_\mathrm{total}$. This is consistent with the Orion Bar observations if UV extinction prevents starlight fluorescence of PAHs in deeper molecular regions. By default, we assume the `"H"` case.

Figure 17 explores the effects that the PAH abundance has on the electron density in the F1 PDR model of the Lorentz Center workshop on PDRs (Röllig et al. 2007). The model is discussed extensively in that paper, so only the relevant details are given here. We added PAHs with three times our default abundance, to be consistent with current estimates, and computed the three PAH abundance cases. The panels show the abundances of some very important species as a function of extinction A_V in the lower panel. Extinction depends on whether the light source is a point source or extended (AGN3 § 7.6) and we use the point-source definition here.

The main regions of a PDR are evident in the lower panel of Figure 17, which is for the `"H"` case. Hydrogen is atomic at very shallow regions but quickly becomes molecular. Carbon transitions from
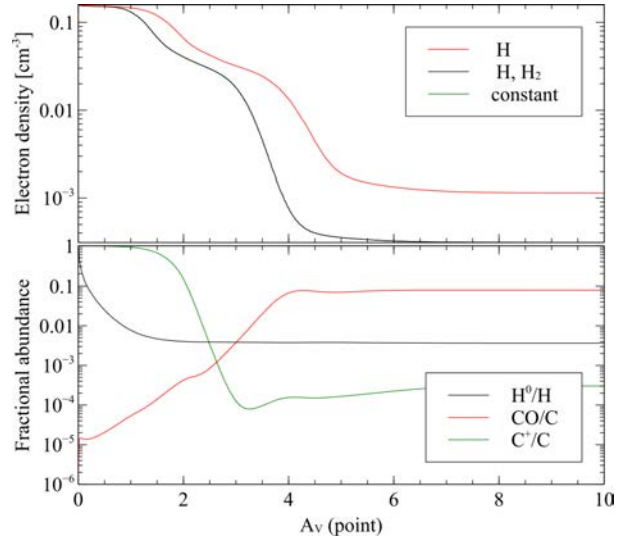
Fig. 17. This compares the effects of our different PAH abundance laws in the Leiden F1 PDR model. The upper panel shows the electron density for the three cases, see text for details. The `constant` and `"H,H2"` cases overlap because there is very little H^+ in this model. The lower panel shows fractional abundances, for the `"H"` case, for some of the important species in a PDR.

C^+ to CO in a narrow range around $A_V \approx 2-4$ mag. Röllig et al. (2007) give further details. The SED used in this model is only defined over a narrow spectral range, see Figure 18, and includes no H-ionizing photons, so the only H^+ present is created by cosmic ray secondary ionization. The next subsection describes some effects this simple SED has our full H I model.

The upper panel shows the predicted electron density. Cosmic rays are the dominant source of hydrogen ionization in this cloud while carbon is a dominant electron donor in some regions. Our treatment of electron capture on grain surfaces is described by van Hoof et al. (2004) and Abel et al. (2005). Although we show all three options, there is little H^+ in this model, so the `constant` and `"H,H2"` cases are identical. The PAH abundance does not vary across Figure 17 in that case. In the `"H"` case, PAHs are present near the illuminated face but have very low abundance at $A_V > 1$ mag, where H is mostly H_2.

Table 7 shows the logs of some predicted column densities for the `"H,H2"` and `"H"` cases. The differences, which can be large, are caused by the changed electron density. These changes suggest a method to determine observationally how the PAH abundance varies with the hydrogen molecular fraction.

TABLE 7

EFFECTS OF PAH ABUNDANCE LAWS

Species	"H"	"H,H2"
H^+	15.43	14.99
H_2	21.90	21.89
H_3^+	14.63	14.91
C^+	17.41	17.28
CH	16.02	16.31
CH_4	15.06	15.78
C_3	15.28	15.86
OH	13.84	13.68
H_2O	13.94	13.73
CO	16.90	16.52
SiO	14.93	14.54

Fig. 18. The SED produced by the `table ISM` command is the lighter line. The infrared cirrus is the peak at $\lambda \sim 100\,\mu$m and starlight dominates at shorter wavelengths. The points just shortward of the Lyman limit ($0.0912\,\mu$m) are interpolated—actually it is thought that interstellar extinction removes most of this continuum. The dashed line shows the interpolated SED and the solid line shows the effects of absorption introduced by adding the `extinguish` command. The heavy red line is SED produced the `table Draine` continuum and used in many PDR calculations. The color figure can be viewed online.

5.4. Lyman Line Pumping in PDR Models

We participated in the 2004 Leiden PDR meeting where we compared our predictions with codes specifically designed to model PDRs (Röllig et al. 2007). The comparison models employed an SED that was only defined over a very narrow range of wavelengths, as shown by the heavy red line in Figure 18. This uses our `table Draine` command to enter the galactic background radiation field given by equation 23 of Draine & Bertoldi (1996).

Early in the comparisons we noticed that our calculations predicted a thin moderately-ionized layer of warm gas on the illuminated face of the PDR that was not seen by the other codes. Some investigation revealed that it was due to hydrogen continuum fluorescence through the Lyman lines, followed by photoionization of the metastable $2s$ level. The process, and our method of removing it to allow comparison with conventional PDR codes, is described next.

Our preferred method of generating the local interstellar radiation field is to use the command `table ISM`. This uses Figure 2 of Black (1987) to represent the *unextinguished* local interstellar radiation field (see Figure 18). The continuum generated by CLOUDY is exactly that given by Black, except that the radiation field between 1 and 4 Ryd is interpolated from the observed or inferred values. Actually it is thought that this part of the radiation field is heavily absorbed by gas in the ISM so that little radiation exists where the dotted line appears, at least in the galactic plane. Such absorption can be introduced with our `extinguish` command. This SED does not include the cosmic microwave background

so that it can be used at any redshift. The CMB command is used to add this component.

Figure 19 shows a closeup of the UV/ FUV portion of the SED with line styles similar to Figure 18. Conventional PDR calculations of, for instance, the Orion PDR, scale up the Draine isotropic radiation field to mimic the SED of the illuminating stars, in this case the Trapezium cluster.

Our preferred method of treating a PDR near a region of active star formation is to include models of the full SED of the central star cluster to model successive H^+, H^0, and H_2 layers (Abel et al. 2005). The higher blue line in Figure 19 shows a portion of the SED of the Trapezium cluster, as implemented with our new `table SED "Trapezium.sed"` command. There is a strong Lyman jump and significant Lyman continuum radiation. The lower black line shows the SED transmitted through the H^+ region and entering the PDR. The stellar continuum is

Fig. 19. The thick red line shows the limited SED produced by the `table Draine` command and used in many PDR calculations. The SED of the Orion Trapezium cluster is shown as the higher blue line while the SED transmitted through the H^+ region and incident on the PDR is the lower black line. The continuum resolution is ten times higher than our default to increase the contrast in the absorption lines. The Lyman line optical depth through the H^+ region is large and the Lyman lines are quite optically thick. The vertical lines at the lower left indicate positions of Lyma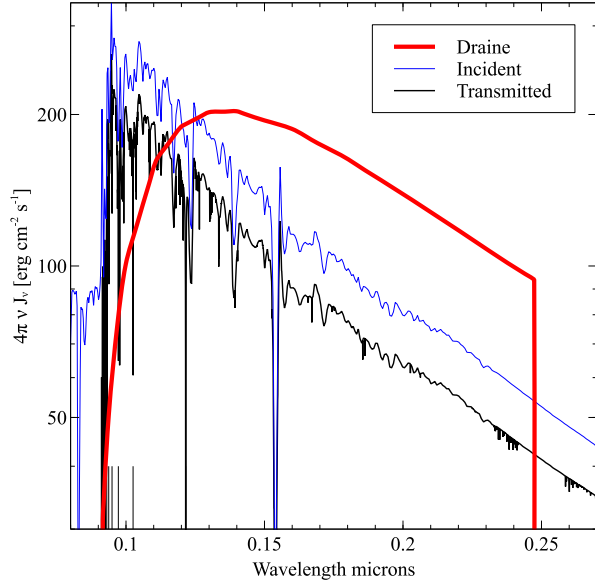n lines. The incident SEDs were normalized to the same radiation parameter G_0. The color figure can be viewed online.

harder than the Draine field, especially at the short wavelengths which cause electron photoejection from grains.

This SED was produced by creating the following model of the Orion Nebula in the style of Baldwin et al. (1991):

```
set continuum resolution 0.1
set save prefix "full"
phi(H) 13.0721 range 0.25 1
table SED "Trapezium.sed"
hden 4
abundances Orion
grains PAH 3 function
stop  efrac -2
stop  temperature off
constant pressure
save overview ".ovr"
save continuum units microns last ".con"
```

This script increases our default continuum resolution by a factor of ten, to make the Lyman absorption line contrast, as discussed next, more promi-

nent. Orion grains and our default PAHs, using the `function` keyword, are included. Note that it was necessary to recompile the grain opacities since the continuum mesh was changed by increasing the resolution. This was done with the `compile grains` command. The incident SED is the Trapezium cluster with the flux of ionizing photons, set with the `phi(H)` command, deduced by Baldwin et al. (1991). Their density was used, and the equation of state assumes constant total pressure. The `stop temperature off` command prevents the code from stopping at the point where the kinetic temperature falls below 4000 K, one of our default stopping criteria. Instead, the calculation stops when the electron fraction, n_e/n_{total}, falls below 10^{-2}, a point near the illuminated face of the PDR.

Orion grains, as used here, are fairly grey, apparently due to a deficiency of small particles. As a result, the UV portion of the transmitted SED is fainter than the incident SED, but the shape is not otherwise greatly changed. Nearly all radiation shortward of the Lyman limit is extinguished. The increased continuum resolution used in Figure 19 allows Lyman absorption lines formed in the H^+ layer to stand out. The vertical bars at the lower left of the figure mark the positions of the higher Lyman lines, which are strongly in absorption. Because of this Lyman line self-shielding, very little light reaches the PDR in the cores of the Lyman lines.

Conventional PDR calculations use the smooth Draine & Bertoldi (1996) SED shown in Figure 19. We do participate in PDR meetings and include several PDR models in our test suite, so this SED must be used. This SED, when coupled with our full model of H I, produces several unexpected results. Figure 20, computed using our version of the standard Leiden (Röllig et al. 2007) V4 test case, shows the problem. The heavy line shows our predicted temperature and hydrogen ionization as a function of depth from the illuminated face of the PDR. We predict a thin, $\delta r \sim 10^{10}$ cm, layer of warm ionized gas.

Examination revealed that this layer is produced by photoionization of hydrogen by the Balmer continuum. The process is outlined in Figure 21. Radiation in the Lyman lines pumps H I to excite the np levels. Some decay to the metastable $2s$ level while others decay back to $1s$ producing Lyman lines which then scatter within the H^0 gas. These eventually decay to produce a Balmer line, and populate either $2s$ or $2p$. The metastable $2s$ level is long lived and can have a significant population. The Balmer continuum photoionizes $2s$, producing the warm, more
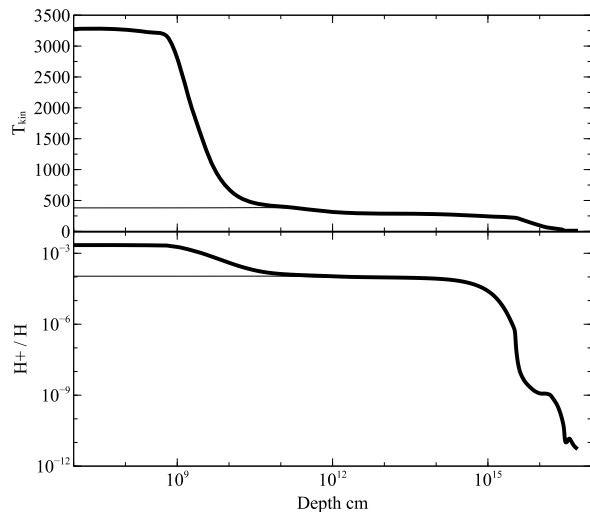
Fig. 20. The gas kinetic temperature (upper panel) and ionized hydrogen fraction (lower panel) for one of the Leiden Meeting test cases. The thick line shows predictions for the simple PDR SED striking an unshielded PDR. A thin layer of warm ionized gas, produced by the process sketched in Figure 21, is produced. The thin line is the same calculation but with the `database H-like Lyman pumping off` command included to block Lyman line fluorescence, as is done in the `pdr_leiden_v4.in` test case in our test suite.

Fig. 21. This shows the process which produces the thin warm layer in Figure 20. Radiation in the Lyman lines photoexcites the np levels via high-n Lyman lines. Many decay to the metastable $2s$ level, which is then photoionized by the Balmer continuum. The process is an artifact of the smooth SED used in PDR simulations. In nature, there is sufficient H I column density in the H^+ layer to make the Lyman lines self shielded.

ionized, layer. The thickness of the layer is set by the column density needed for the Lyman lines to become self shielded.

In previous versions of CLOUDY, we recommended adding the `case B` command to artificially make the Lyman lines optically thick. That command has other effects and we introduce a new command, `database H-like Lyman pumping off`, to make all Lyman lines optically thick. The actual effect is to prevent the pumping rather than change the radiative transfer of the Lyman lines. When this command is included in the input deck we obtain the results shown as the light line in Figure 19. This not only makes our predictions more closely match those of conventional PDR codes, but also results in a significant time savings since resolving the thin warm layer is fairly expensive.

5.5. The LAMDA Database

Since C13, we have updated our version of the LAMDA (Schöier et al. 2005) database of molecular structure and emission. LAMDA does not use version numbers. Our version of LAMDA was downloaded on 2015 June 30.

In addition to updating collisional rates for several species, which have been modified by LAMDA

since the last integration of CLOUDY with the LAMDA database in C10, we added the ability to predict the intensity of five of their new species: OH^+, H_2S, H_2CS, C_2H, and NH_2D.

CLOUDY uses the stored level energies to predict line wavelengths, photon energies, and collision rates (Lykins et al. 2015). Some of the energy levels present in LAMDA are not precise enough to compute wavelengths with sufficient accuracy. LAMDA does give the frequency of all transitions to higher precision than the energy levels. Therefore, for the species where more precision is needed, we modified the LAMDA data to include higher precision for the energy levels. This was especially important for hyperfine transitions, such as in OH, where computing the wavelengths using the energy level spacing present in LAMDA leads to multiple transitions having the same wavelength. For C17, these issues have been resolved and all hyperfine transitions for OH are now specified with unique wavelengths.

Overall, the improved rates from the LAMDA update did change some molecular intensities in our test suite of simulations. The largest and most notable were H_2O, CS, and some of the high rotational transitions of CO.

5.6. *The Grain Data*

In order to model grains in photoionized environments and XDRs, Cloudy needs grain refractive index data covering the entire wavelength range from the X-ray to the far-IR and sub-mm regime. The reason for this is that Cloudy creates a self-consistent model of the physical state of the grains. The X-ray data are needed because X-ray photons can be important for heating and charging of the grains in environments with a hard radiation field, while the IR and sub-mm data are obviously needed to correctly predict the thermal emission from the grains. Refractive index data covering such a vast wavelength region are very hard to find, which is the reason why Cloudy only offers data for a limited set of grain materials. In C17 we added refractive index data for α-SiC using the results from Laor & Draine (1993). The enthalpy data needed to model stochastic heating of these grains were taken from Chekhovskoy (1971). We created a custom fit to the data from Table 4 for $T < 300$ K, while we retained Equation 3 for higher temperatures, resulting in the following formulas for the heat capacity C_p of α-SiC in $\mathrm{cal\,mol^{-1}\,K^{-1}}$:

$$C_p = 13.25 \times [0.398 f_3(T/\Theta_1) + 0.602 f_3(T/\Theta_2)]$$
$$\text{for } T < 300 \text{ K,}$$
$$C_p = 13.25 - 2035/T + 288 \times 10^5/T^2 \exp(-5680/T)$$
$$\text{for } T \geq 300 \text{ K.}$$

Here T is the temperature of the grain in kelvin, Θ_i are the Debye temperatures of the material given by $\Theta_1 = 747$ K and $\Theta_2 = 1647$ K, and the function f_n is given by:

$$f_n(x) = \frac{1}{n} \int_0^1 \frac{y^n \mathrm{d}y}{\exp(y/x) - 1}.$$

To convert the heat capacity to $\mathrm{erg\,mol^{-1}\,K^{-1}}$, the formulas above need to be multiplied by $4.184 \times 10^7\,\mathrm{erg\,cal^{-1}}$.

Cloudy includes data for AC and BE amorphous carbon taken from Rouleau & Martin (1991). These data used an erroneous $\beta = 2$ extrapolation of the laboratory data towards long wavelengths. This extrapolation has been removed in C17, so that the data now have the expected $\beta \approx 1$ behavior in the sub-mm regime.

The numerical integration scheme for grain opacities that is part of the Mie code has been rewritten, resulting in higher accuracy results. This was needed for the new SiC refractive index data, but will also result in more accurate data for other grain materials. We also modified the code to allow it to converge opacity data for larger grains. All the grain opacity files in C17 have been updated using the new code.

6. THE COOLING FUNCTION

The gas kinetic temperature is the only temperature used in a non-equilibrium plasma. A temperature could be defined for individual level populations or the degree of ionization, but each would have a different value if the gas is not in LTE. The electron velocity distribution in a fully ionized gas is assumed to be Maxwellian because of frequent electron-electron elastic collisions (Spitzer 1962; Ferland et al. 2016). This is often not true in a partially-ionized gas, especially one exposed to energetic radiation or cosmic rays (Spitzer & Tomasko 1968). In this case, a population of suprathermal electrons can be present, and is treated as described in C13 and AGN3. The kinetic temperature is set by the energy exchange, the rate at which inelastic collisions between particles convert kinetic energy into light, which then escapes. The cooling function, described here, represents the total cooling due to all species.

6.1. *Species Cooling*

Nearly all species are now treated with multi-level models of the internal structure of the atom or molecule. In earlier versions of the code, with much simpler model atoms, it was easy to determine the cooling due to a particular line. For a two-level atom the net energy exchange, the rate at which kinetic energy is converted into light, is

$$\Lambda_1 = (n_l q_{l,u} - n_u q_{u,l}) h\nu_{u,l}\,, \qquad (6)$$

where the q's are collision rates, s^{-1}, u, l indicate the upper and lower levels, and $h\nu_{u,l}$ represents the energy difference, which corresponds to the photon energy for a two-level system.

With a large multi-level model this single-line concept loses meaning. The total cooling due to a species with N levels is

$$\Lambda_{species} = \sum_{u=2}^{N} \sum_{l=1}^{l<u} (n_l q_{l,u} - n_u q_{u,l}) h\nu_{u,l}\,, \qquad (7)$$

We now report the total cooling due to a species with the species label followed by a wavelength of "0" to indicate that it represents the entire species. Examples include the following entries which were taken from the output of the `save line labels` command (§ 2.6.5 above):

```
30      H  1c   0   net cooling due to iso-seq species
31      H  1h   0   heating due to iso-seq species
32      He 2c   0   net cooling due to iso-seq species
33      He 2h   0   heating due to iso-seq species
450     Sc16c   0   net cooling due to database species
451     Sc16h   0   heating due to database species
452     Sc17c   0   net cooling due to database species
453     Sc17h   0   heating due to database species
```

Each entry has either "c" or "h" after the line label. The "c" indicates that the sum in Equation 7 is positive and that the species contributes net cooling. If the level populations are inverted, corresponding to a negative temperature, the species will heat rather than cool the gas, the sum will be negative, and will appear with the "h" character. This often occurs when levels are predominantly photoexcited by the attenuated incident radiation field.

6.2. *Time-Steady Non-Equilibrium Cooling Function*

Nearly all of the calculations presented in this paper are non-equilibrium in the sense that the ionization and level populations are not described by the gas kinetic temperature. The Boltzmann level population and Saha-Boltzmann ionization equations do not apply. Equilibrium only occurs at the highest densities in Figures 10, 11, and 12.

By default, CLOUDY solves for the non-equilibrium conditions in a gas cloud in steady state, i.e., assuming that its properties do not evolve over times that are more rapid than those needed for atomic processes to come into equilibrium. This is accomplished by taking the difference between the recombination and ionization rates in the ionization balance equation for each species to be zero. We provide an `age` command that will check whether this is a valid assumption.

Gnat & Ferland (2012), Lykins et al. (2013), and Wang et al. (2014) use CLOUDY to compute time-steady cooling. Figure 22 shows cooling functions for three very different sets of chemical abundances. The cooling in the primordial case is dominated by H, He, and their molecules, while the solar case has been discussed in many papers. The original review by Dalgarno & McCray (1972) is still among the best. The cooling in the high-metallicity case, marked "Z10", is dominated by the heavy elements.

The input script used to create the large solar case shown in Figure 22 is given below. This set of calculations uses our `grid` command to vary the kinetic temperature between 10 K and 10^{10} K. The `grid` and `optimize` command now use the `*nix fork` system call to compute a series of independent models, one on each available thread. This method
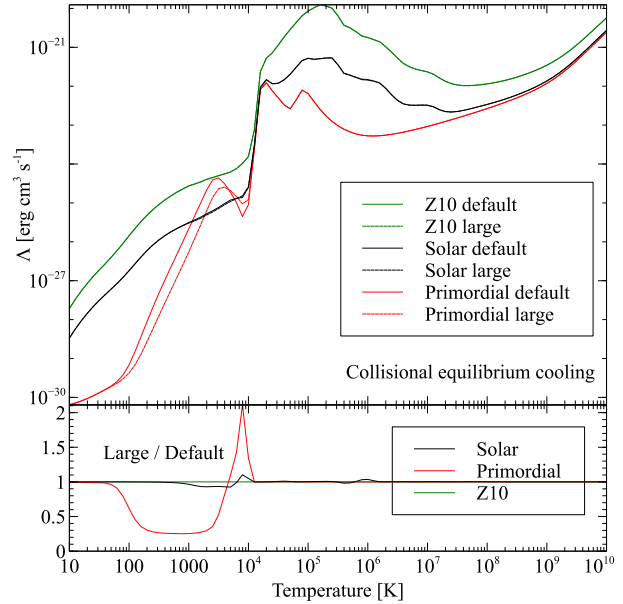
Fig. 22. Time-steady non-equilibrium cooling for three sets of chemical abundances. The gas is collisionally ionized by thermal collisions although background cosmic rays are included to allow the chemistry to converge at very low temperatures. Calculations are done for both our default and maximum atomic models. The upper panel shows the total cooling for each set of abundances while the lower panel shows the ratio of cooling computed with the large to default models.

of computing in parallel is discussed further in § 8 below.

```
set save prefix "all"
database H2
database CHIANTI levels maximum
database stout levels maximum
database lamda levels maximum
coronal t=3 vary
grid 1 10 .1 log
hden 0
stop zone 1
set dr 0
cosmic rays background
save grid ".grd"
save cooling ".col"
```

This example may have problems on some computers. A single calculation uses nearly 4GB of RAM since all the models are set to the largest number of levels. However, this is a grid run which launches many models simultaneously. If the total memory requirements of these models exceed the physical memory in the system, the OS may start using swap space (which is very slow) to compute the model, or (if that fails) abort the sim. This is an inevitable consequence of computing many large models on a multi-core system. In such a case, the solution is to

run the model sequentially by adding the keyword `sequential` to the `grid` command. Then, only a single thread will be started requiring 4 GiB of memory in total. This is another example of the necessary compromise between model fidelity and resource utilization which permeates this review.

The `coronal` command sets the kinetic temperature and tells the code to bypass its normal check that the incident SED is correctly specified, since a purely collisional model may be intended. The `hden` command sets the hydrogen density to $1\,\mathrm{cm}^{-3}$ and the `set dr` and `stop zone 1` commands result in a single zone with a 1 cm thickness. We include the chemistry network originally based on Abel et al. (2005) and Röllig et al. (2007), and originally based on UMIST (Le Teuff et al. 2000). That chemistry will not converge at low temperatures without a source of ionization to drive the ion-molecule reactions. The background cosmic rays provide that ionization.

Figure 22 compares the cooling with both our default and largest data sets, and shows their ratio in the lower panel. The largest differences are due to including the complete H_2 model in the large models. The complete model includes detailed treatment of formation and dissociation processes, which results in somewhat different predictions for the chemistry, compared with the default model. The explicit calculation of thousands of H_2 lines changes the cooling per H_2. Both produce the large differences around 100 K - 1000 K in the primordial case.

There are only small differences at moderate to high temperatures. The default model is surprisingly accurate for these temperatures due to the level selection criteria described by Lykins et al. (2013).

Figure 23 compares the total emission for the "Z10" case and a temperature of 10^6 K for our default (red) and large (black) models. Over much of the spectrum they are similar and the default model includes the strongest lines. However, there are significant "gaps" in some portions of the spectrum as shown in the lowest panel. This shows that our default setup is good enough for most purposes, but that there will be circumstances when a larger model is needed.

6.3. Time-dependent non-equilibrium cooling

There are applications where the time-steady assumption is not valid (e.g., Gnat & Sternberg 2007; Gnat 2017). Cloudy has long included the option to model time-steady non-equilibrium dynamical flows, (Henney et al. 2005, 2007), in which advected material enters gas at a particular location, altering the balance equations.
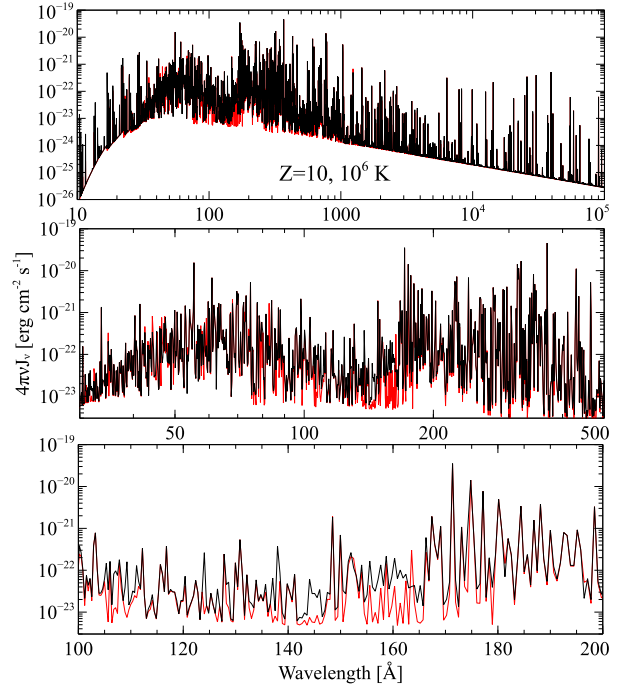
Fig. 23. The spectrum of a $10Z_\odot$ plasma using our default (red) and large database (black). The top panel shows the full emission and each panel below it is a zoom into smaller regions of spectrum. The color figure can be viewed online.

Chatzikos et al. (2015) has extended this to treat the time-dependent non-equilibrium case. This extended the steady-state treatment to permit solving the class of time-dependent problems related to the cooling of a parcel of gas from a definite initial state. In the time-dependent scheme, ionization and recombination are not in balance, which introduces a net rate of change for a species density. This permits advancing the ionization for each species over time-steps Δt with a first-order implicit integration scheme, as explained in mode detail in Chatzikos et al. (2015).

Example calculations, available as of C17,[18] evolve a unit volume of gas from a preset temperature (30 million K) to a definite floor (10,000 K). The commands

```
coronal 3e7 init time
stop time when temperature falls below 1e4
```

are used to set the initial and final temperatures.

Figure 24 presents the evolution of temperature with time in the top panel, and of the time-step advance with temperature in the bottom panel. The

---

[18]Test suite models `time_cool_cd.in` and `time_cool_cp.in`.
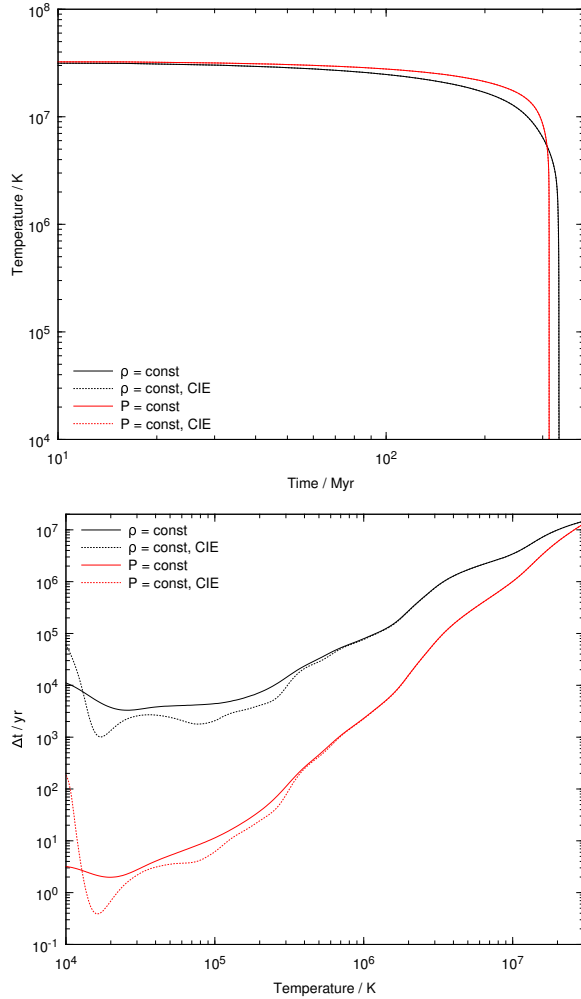
Fig. 24. Time-dependent cooling of a unit volume of gas. Evolution of temperature with time *(top panel)* and time-step advance with temperature *(bottom panel)* under isobaric and isochoric conditions. The dashed curves show the evolution assuming collisional ionization equilibrium (CIE). The color figure can be viewed online.

solver adapts the time-step to track the changing conditions in the gas. At high temperatures, the system evolves slowly, and large time-steps are taken, while at lower temperatures, the time-step size is reduced and a larger number of steps is required for fixed fractional change in temperature. In both isochoric and isobaric cases, cooling down to 10 million K overwhelms the total cooling time of the gas, which subsequently cools down to 10,000 K about 4–15 times faster. This is related to the peak of the cooling function around 300,000 K, see Figure 22. For isobaric conditions, the density rises with decreasing temperature, which enhances the cooling rate of the gas, and leads to the shorter cooling time-

steps seen in the bottom panel of Figure 24. Compared to the collisional equilibrium ionization case, the system generally takes longer time-steps, because the cooling function is suppressed, as explained in Gnat & Sternberg (2007).

As Figure 25 shows, the time-dependent scheme is able to reproduce the known behavior that deviations from equilibrium at fixed temperature become important only below the peak of the cooling curve at ≈300,000 K (Chatzikos et al. 2015). We illustrate this effect by forcing equilibrium conditions with the command[19]

`set dynamics populations equilibrium`

In that Figure, the equilibrium ionization fraction of Fe^{6+} drops quickly with decreasing temperature. This comparison highlights the non-equilibrium origin for the tail to moderate ionization fraction values at lower temperatures.

In time-steady calculations, CLOUDY reports the instantaneous intrinsic and emergent emission produced by the cloud, where the latter has been corrected for extinction occurring outside the line-forming region. These are reported by default in the main output of the program.

In time-dependent calculations, integrations over time of the instantaneous intrinsic and emergent emission are performed, referred to as "cumulative" emission. The general form of the integration is

$$F = \int dt\, j(t)\, w(t)\,, \qquad (8)$$

where $w(t)$ is a weighting function. Its application to line emission is presented in Chatzikos et al. (2015), equation (3). The integration may be performed in two fashions, or not done at all, through the commands

```
set cumulative mass
set cumulative flux
set cumulative off
```

By default, weighting by `mass` is performed, which uses a weighting function $w(t) = 1/\rho(t)$, where $\rho(t)$ is the mass density at time t. Notice that the units of the time-integral of the emissivity are erg g^{-1}. Obviously then, this choice closely traces the predictions of the cooling flow model (Fabian et al. 1984). Specifically for lines, the integral reduces to the usual line Γ factors (Chatzikos et al. 2015; Graney & Sarazin 1990). Luminosities may be obtained from these estimates by multiplication by the

---

[19]See test suite model `time_cool_cp_eq.in`.
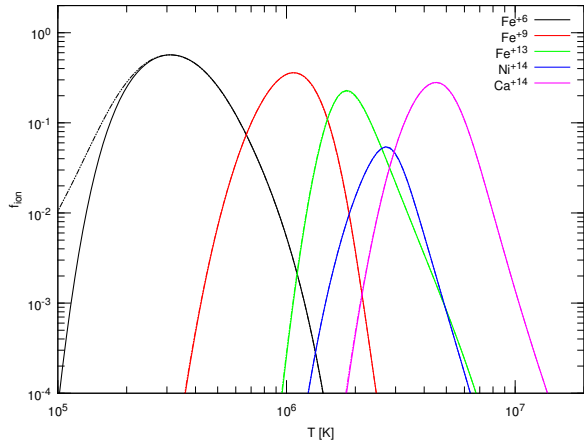
Fig. 25. Comparison of ionization fractions in collisional equilibrium (solid lines) and non-equilibrium ionization (dot-dot-dashed lines). The effects of the latter become important below 300,000 K.

Fig. 26. Cooling flow spectra in the energy range 0.1–9 keV, at different energy resolutions. The top panel corresponds to the proposed resolution of *Athena*, the middle panel corresponds to the current state-of-the-art resolution obtained with dispersed X-ray spectrometers, such as *RGS* onboard *XMM-Newton*, while the bottom panel corresponds to the typical energy resolution in X-ray imaging observations.

mass cooling rate, $\dot{M}$. Notice, however, that these considerations apply only to unit volume calculations; for extended clouds the meaning of the computed emission is unclear.

On the other hand, when weighting by `flux`, the weighting function is taken to be unity, $w(t) = 1$, which suggests that the units of the integrated emission are erg cm^{-3}. This is equivalent to the power emitted per unit volume over the course of the integration. For extended models, the units become erg cm^{-2}, and have the meaning of the accumulated flux over the duration of the simulation. Such weighting is more appropriate for calculations on fixed domains, as will be discussed in a future paper.

For a cooling flow, we follow a parcel of gas as it cools down, in the manner shown in Figure 24. We integrate over time the intrinsic and emergent emission to capture the emission from all the regions that contribute to the observed spectrum. By default, CLOUDY reports both the instantaneous emission from the gas at each time, as well as the cumulative emission up to that point in the simulation, when time-dependent simulations are enabled.

Figure 26 presents the predicted soft X-ray spectrum from a cooling flow, as would be observed by X-ray telescopes at three different energy resolutions. The bottom panel corresponds to the current state of affairs for X-ray imaging spectroscopy with the detectors onboard *Chandra* or *XMM-Newton*. The current state of the art, obtained with X-ray dispersed spectroscopy observations, is shown in the middle panel. Finally, the top panel shows the spectrum

that can be obtained with microcalorimeters such as those onboard the unfortunate *Hitomi* mission, and the proposed *Athena* mission.

For the purposes of that Figure, the cumulative emission (line and continuum) was obtained by using the keyword `cumulative` with the family of `save continuum` commands. Note that the instantaneous cloud emission can still be obtained by invoking the `save` commands without the `cumulative` keyword. For reference, a minimum set of commands to reproduce the high resolving power spectrum in the top panel of the Figure is the following

```
coronal 1.1e7 K init time
hden 5.88e-2 linear
constant pressure reset
set dr 0
set nend 1
stop zone 1
iterate 400
stop time when temperature falls below 6e5 K
cosmic rays background
set save resolving power 2000
save cumulative continuum units Angstroms \
    last "cooling.concum"
```
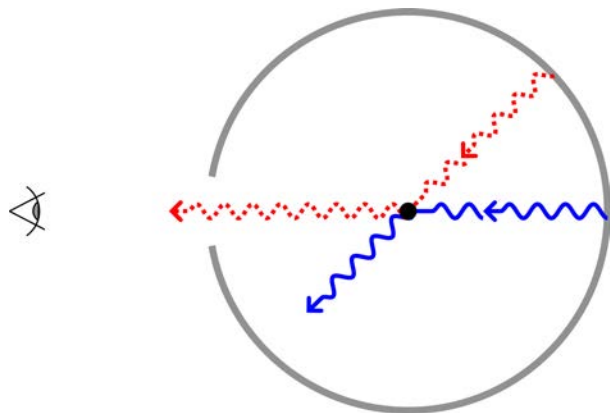
Fig. 27. Photons of an isotropic continuum are absorbed and reemitted in random directions by an idealized isolated absorber (atom or molecule). This process does not change the isotropic character of the radiation field, but it does populate the upper level of the transition for an ensemble of absorbers, and therefore moderates the line emissivity.

We point out that the `set save resolving power` command increases the line-to-continuum contrast without adjusting the line width and therefore violates energy conservation in the saved spectrum.

7. OTHER PHYSICS CHANGES

7.1. *Corrections for Isotropic Radiation*

Chatzikos et al. (2013) expanded our treatment of isotropic radiation fields to produce new reporting options in which their effects are removed, to better approximate what is measured at the telescope. Figure 27 presents an idealized situation, in which an isolated absorber (atom or molecule) is exposed to isotropic radiation, and undergoes two successive excitations, each followed by a radiative deexcitation. An example might be the CMB photo-exciting the CO rotation ladder. Because of the isotropic character of the field, the number of photons scattered out of the line of sight is equal to the number scattered into the line-of-sight, so the radiation field remains isotropic despite the presence of the absorber. No net emission or absorption feature is produced.

A population of absorbers behaves similarly. Isotropic photons at the frequency of an atomic (or molecular) transition are absorbed and reemitted in random directions, leaving the field isotropic. Although pumping by an isotropic continuum does not produce a spectral line in the two-level system, it does affect the level populations, which then affect the line emissivity. This has been traditionally parameterized as a diminution factor on the emergent line intensity (e.g., D'Cruz et al. 1998).

It can be shown that this diminution factor is connected to the escape probability formalism employed for the transfer of radiation. The essence of the escape probability theorem lies in the statement that the net emission from a parcel of gas at some location in a cloud is proportional to the probability of escape from the cloud starting from that location in a *single* flight. Photons that require several scatterings before escape are assumed to be absorbed *in situ*, that is, CLOUDY does not track their propagation through the gas cloud. The first proof of the theorem was offered by Irons (1978), who showed that it had the character of energy conservation for an emitting volume. The theorem was subsequently extended by Rybicki (1984), who showed that it was far more detailed, as it applied to individual rays. In Chatzikos et al. (2013), Rybicki's formalism was refined for the case of isotropic radiation, and it was shown that the net emission is proportional to the usual escape probability times a factor that depends on the field intensity (see equations (39) and (40) in Chatzikos et al. 2013). It was also shown that this form reduces to the traditional diminution factor.

Because isotropic radiation may affect line emissivities across the spectrum, as of C17, line intensities are corrected for isotropic radiation by default. This resembles the usual practice in far infrared, millimeter, and radio observations to automatically correct for the CMB by some method (position, beam, or frequency switching), so that the observer is provided with net line or continuum fluxes. This behavior may be disabled with the aid of the command:

`no lines isotropic continuum subtraction`

which causes line intensities uncorrected for isotropic radiation to be reported.

On the other hand, the transmission of the continuum through the cloud involves only the attenuation of radiation at some frequency due to optical depth effects. By default, CLOUDY reports the total continuum radiation, including any attenuated isotropic radiation, unless the command:

`no isotropic continuua report`

is issued, or the keyword `no isotropic` is used with any of the `save continuum` commands. Either of these options will cause the continuum to be corrected for any (attenuated) isotropic radiation.

As an illustration of these capabilities, Figure 28 presents the emergent spectrum of an interstellar cloud irradiated by two isotropic continua: the cosmic microwave background and the local interstellar continuum. The black and red curves show the total
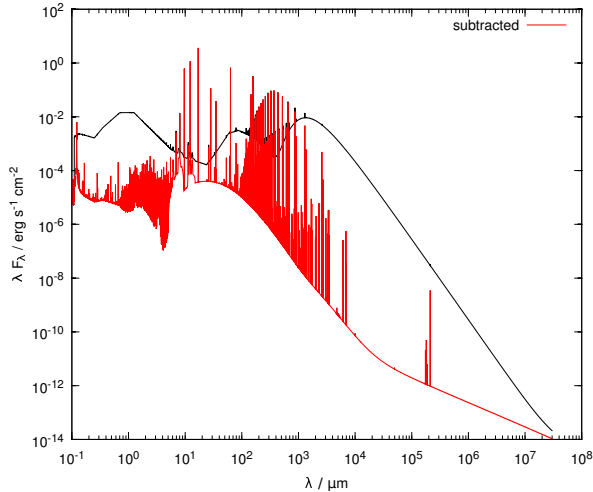
Fig. 28. Example of the correction for isotropic continua. An interstellar cloud is exposed to a radiation field that is the superposition of two isotropic continua: the local interstellar radiation field, and the CMB. The black curve shows the spectrum emergent from the cloud. This is the light distribution incident on a telescope. In the radio and the far infrared, observations are corrected in real time for isotropic continua (e.g., by position, beam, or frequency switching). The red curve shows the spectrum that such observations would yield. Notice that at the position of the H I 21cm line, the correction is about 4 dex. The color figure can be viewed online.

emergent spectrum, and that corrected for isotropic radiation, respectively. The figure highlights the magnitude of isotropic radiation in the mm, where the CMB overwhelms the diffuse fields by 6–8 dex. The calculation may be reproduced with the following commands:

```
cmb
table ism
extinguish 21
cosmic ray background
database H2
grains PAH 3
abundances ISM
hden 3
stop thickness 1 linear parsec
constant temperature 500 K
stop temperature off
save continuum units microns "iso.con"
save continuum units microns no isotropic \
    "iso.con-noiso"
```

7.2. *Chemical Composition*

The built-in abundance sets have been exported to external files located in the `cloudy/data/abundances` directory. These are

much easier to add or change since updates no longer require editing the C++ source code. There is no change in the `abundances`-type commands which use these files.

The default composition is given in the file `cloudy/data/abundances/default.abn`. It can be updated by merely changing this file. A new `abundance "filename"` command has been introduced. The chemical composition will be read from the specified file, which may be located in the current directory or in `cloudy/data/abundances`. The `abundance "filename"` command has a `print` option to report the gas abundances and grain types used.

The command `abundances isotopes` may be used to specify isotope fractions for the species of astrophysical interest. By default, the isotope abundances of Asplund et al. (2009) are used, with a couple of modifications (see `cloudy/data/abundances/default-iso.abn`).

The command `element [name] isotopes` may be issued to modify the default isotopic abundances to user-specified values. For instance, the commands to specify isotope fractions for hydrogen and carbon are now:

```
element hydrogen isotopes (1, 1) (2, 2e-5)
element carbon isotopes (12, 29) (13, 1)
```

For each element, isotopes are specified as pairs of the atomic weight and its fractional abundance by number. The sum of isotopic abundances is renormalized to unity.

7.3. *The Table SED Command and Stellar Grids*

A number of built-in SEDs are available by a series of `table ...` commands. These have been exported into data files in the `cloudy/data/SED` directory. This makes the external SEDs simple to maintain and easy to build upon. The `table ...` commands present in previous versions of the code work as they did before.

The `table HM12` command has been added to implement the Haardt & Madau (2012) grid of background continua. The command works the same way as the `table HM05` command, except that the keyword quasar is not supported (since data files for the quasar-only case do not exist). This command uses the stellar grid infrastructure described in C13 to do the interpolation. The `table HM05` command has also been moved over to use this infrastructure, but this should be transparent to the user.

these areas, particularly collisional excitation processes, and worthwhile improvements for more typical cases.

8.4. *Other Changes*

A large number of small changes have occurred. These are summarized at `http://trac.nublado.org/wiki/NewC17`. Some of the more significant changes are:

- Commas are no longer allowed to be embedded in numbers, they are treated as separators along with most other symbols. Standard exponential format 3.14159e16 can be used instead. Using commas embedded in numbers was deprecated since C10.

- The `tlaw` command now has a `table` option, similar in function to the existing `dlaw table` command.

- We are converting the `save` command output to report linear quantities. The output had reported a mix of log and linear quantities. A `log` option has been added to report quantities in the old style, for backwards compatibility.

- The fundamental constants have been updated to the CODATA 2014 values.

- The `run_parallel.pl` script can now run only a subset of the scripts in the test suite. We have added a new script `rerun_parallel.pl` that works the same way as `run_parallel.pl`, except that it does not delete the output from a previous run.

- We have added support for platforms where `g++` is missing, but the `clang++` compiler is present. This includes systems with a FreeBSD or Mac OS X operating system.

8.5. *Online Access*

The primary access to all versions of Cloudy remains the `http://nublado.org` web site. The general organization has not changed since the C13 review. A full set of changes to Cloudy since C13, many too technical to be included here, are available on the page `http://trac.nublado.org/wiki/NewC17`.

Many suggestions for improving Cloudy came from the discussion forum hosted at `https://groups.yahoo.com/neo/groups/cloudy_`

`simulations/info`. Gabriel Altay provided valuable input for implementing the `table HM12` command. Testing for the beta versions of this release was provided by Christophe Morriset, Eric Pellegrini, & Mitchell Revalski. We are grateful for their help.

DEDICATION

We dedicate this paper to the many friends of the Cloudy *project across Mexico, and to the Mexican people for making our many visits to their beautiful country so wonderful.*

APPENDICES

A. ATOMIC AND IONIC SPECIES TREATED IN Cloudy

Table 8 lists the species treated by Cloudy, followed by the database from which their energy and transition, radiative and collisional, data are drawn.

The table was prepared with the aid of the `cloudy/scripts/db-species-tex.pl` Perl script in the Cloudy distribution, which operates on the output of the `save species labels` command.

B. STOUT DATA

Table 9 lists the species included in the Stout database. Species names followed by the symbol "‡" are used by default by Cloudy, as they are listed in `Stout.ini.masterlist`. For each species, the references for the energy, transition probability, and collisional data are given. For the latter, the designation "baseline" has the same meaning as in Lykins et al. (2015), namely that no collisional data are available, and that the "g-bar" approximation is used instead.

The table was prepared with the aid of the Perl scripts `cloudy/scripts/db-ref-bib2json.pl` and `cloudy/scripts/db-ref-json2tex.pl` in the Cloudy distribution. The former walks through the Stout database, gathers bibliographical references, and stores them in an external file in JSON format. The latter script operates on the data in that file to create the table itself, in TeX format.

TABLE 8

SPECIES DATA BASES

Species	Database	Species	Database	Species	Database	Species	Database
H	H-like	O^{7+}	H-like	Mg^{4+}	Chianti	P	Stout
He	He-like	F	…	Mg^{5+}	Chianti	P^+	Stout
He^+	H-like	F^+	Stout	Mg^{6+}	Chianti	P^{2+}	Stout
Li	Stout	F^{2+}	Stout	Mg^{7+}	Chianti	P^{3+}	Stout
Li^+	He-like	F^{3+}	Stout	Mg^{8+}	Chianti	P^{4+}	Chianti
Li^{2+}	H-like	F^{4+}	Stout	Mg^{9+}	Chianti	P^{5+}	Stout
Be	Stout	F^{5+}	Stout	Mg^{10+}	He-like	P^{6+}	Chianti
Be^+	Stout	F^{6+}	Stout	Mg^{11+}	H-like	P^{7+}	Chianti
Be^{2+}	He-like	F^{7+}	He-like	Al	Stout	P^{8+}	Chianti
Be^{3+}	H-like	F^{8+}	H-like	Al^+	Chianti	P^{9+}	Chianti
B	Stout	Ne	Stout	Al^{2+}	Stout	P^{10+}	Chianti
B^+	Stout	Ne^+	Stout	Al^{3+}	Stout	P^{11+}	Chianti
B^{2+}	Stout	Ne^{2+}	Stout	Al^{4+}	Chianti	P^{12+}	Chianti
B^{3+}	He-like	Ne^{3+}	Chianti	Al^{5+}	Stout	P^{13+}	He-like
B^{4+}	H-like	Ne^{4+}	Chianti	Al^{6+}	Chianti	P^{14+}	H-like
C	Stout	Ne^{5+}	Chianti	Al^{7+}	Chianti	S	Stout
C^+	Stout	Ne^{6+}	Chianti	Al^{8+}	Chianti	S^+	Stout
C^{2+}	Stout	Ne^{7+}	Chianti	Al^{9+}	Chianti	S^{2+}	Stout
C^{3+}	Chianti	Ne^{8+}	He-like	Al^{10+}	Chianti	S^{3+}	Chianti
C^{4+}	He-like	Ne^{9+}	H-like	Al^{11+}	He-like	S^{4+}	Chianti
C^{5+}	H-like	Na	Stout	Al^{12+}	H-like	S^{5+}	Chianti
N	Stout	Na^+	Stout	Si	Stout	S^{6+}	Chianti
N^+	Chianti	Na^{2+}	Chianti	Si^+	Stout	S^{7+}	Chianti
N^{2+}	Chianti	Na^{3+}	Chianti	Si^{2+}	Stout	S^{8+}	Chianti
N^{3+}	Chianti	Na^{4+}	Chianti	Si^{3+}	Stout	S^{9+}	Chianti
N^{4+}	Stout	Na^{5+}	Chianti	Si^{4+}	Chianti	S^{10+}	Chianti
N^{5+}	He-like	Na^{6+}	Chianti	Si^{5+}	Chianti	S^{11+}	Chianti
N^{6+}	H-like	Na^{7+}	Chianti	Si^{6+}	Stout	S^{12+}	Chianti
O	Stout	Na^{8+}	Chianti	Si^{7+}	Chianti	S^{13+}	Chianti
O^+	Stout	Na^{9+}	He-like	Si^{8+}	Stout	S^{14+}	He-like
O^{2+}	Stout	Na^{10+}	H-like	Si^{9+}	Chianti	S^{15+}	H-like
O^{3+}	Chianti	Mg	Stout	Si^{10+}	Chianti	Cl	Stout
O^{4+}	Stout	Mg^+	Chianti	Si^{11+}	Chianti	Cl^+	Chianti
O^{5+}	Chianti	Mg^{2+}	Stout	Si^{12+}	He-like	Cl^{2+}	Chianti
O^{6+}	He-like	Mg^{3+}	Chianti	Si^{13+}	H-like	Cl^{3+}	Chianti
Cl^{4+}	Stout	K^{4+}	Chianti	Sc	Stout	Ti^{14+}	Chianti
Cl^{5+}	Stout	K^{5+}	Chianti	Sc^+	Stout	Ti^{15+}	Chianti
Cl^{6+}	Stout	K^{6+}	Stout	Sc^{2+}	Stout	Ti^{16+}	Chianti
Cl^{7+}	Stout	K^{7+}	Stout	Sc^{3+}	Stout	Ti^{17+}	Chianti
Cl^{8+}	Stout	K^{8+}	Chianti	Sc^{4+}	Stout	Ti^{18+}	Chianti
Cl^{9+}	Chianti	K^{9+}	Stout	Sc^{5+}	Stout	Ti^{19+}	Chianti

TABLE 8 (CONTINUED)

Species	Database	Species	Database	Species	Database	Species	Database
Cl^{10+}	Chianti	K^{10+}	Chianti	Sc^{6+}	Stout	Ti^{20+}	He-like
Cl^{11+}	Chianti	K^{11+}	Chianti	Sc^{7+}	Stout	Ti^{21+}	H-like
Cl^{12+}	...	K^{12+}	Chianti	Sc^{8+}	Stout	V	...
Cl^{13+}	Chianti	K^{13+}	Chianti	Sc^{9+}	Stout	V^{+}	...
Cl^{14+}	...	K^{14+}	Chianti	Sc^{10+}	Stout	V^{2+}	...
Cl^{15+}	He-like	K^{15+}	Chianti	Sc^{11+}	Stout	V^{3+}	Stout
Cl^{16+}	H-like	K^{16+}	Chianti	Sc^{12+}	Stout	V^{4+}	...
Ar	Stout	K^{17+}	He-like	Sc^{13+}	Stout	V^{5+}	Stout
Ar^{+}	Stout	K^{18+}	H-like	Sc^{14+}	Stout	V^{6+}	Stout
Ar^{2+}	Stout	Ca	Stout	Sc^{15+}	Stout	V^{7+}	Stout
Ar^{3+}	Stout	Ca^{+}	Chianti	Sc^{16+}	Stout	V^{8+}	Stout
Ar^{4+}	Stout	Ca^{2+}	Stout	Sc^{17+}	Stout	V^{9+}	Stout
Ar^{5+}	Stout	Ca^{3+}	Stout	Sc^{18+}	...	V^{10+}	Stout
Ar^{6+}	Chianti	Ca^{4+}	Chianti	Sc^{19+}	He-like	V^{11+}	Stout
Ar^{7+}	Chianti	Ca^{5+}	Stout	Sc^{20+}	H-like	V^{12+}	Stout
Ar^{8+}	Chianti	Ca^{6+}	Chianti	Ti	...	V^{13+}	...
Ar^{9+}	Chianti	Ca^{7+}	Chianti	Ti^{+}	...	V^{14+}	Stout
Ar^{10+}	Chianti	Ca^{8+}	Chianti	Ti^{2+}	Stout	V^{15+}	Stout
Ar^{11+}	Chianti	Ca^{9+}	Chianti	Ti^{3+}	Stout	V^{16+}	Stout
Ar^{12+}	Chianti	Ca^{10+}	Chianti	Ti^{4+}	Stout	V^{17+}	Stout
Ar^{13+}	Chianti	Ca^{11+}	Chianti	Ti^{5+}	Stout	V^{18+}	Stout
Ar^{14+}	Chianti	Ca^{12+}	Chianti	Ti^{6+}	Stout	V^{19+}	Stout
Ar^{15+}	Chianti	Ca^{13+}	Chianti	Ti^{7+}	Stout	V^{20+}	Stout
Ar^{16+}	He-like	Ca^{14+}	Chianti	Ti^{8+}	Stout	V^{21+}	He-like
Ar^{17+}	H-like	Ca^{15+}	Chianti	Ti^{9+}	Stout	V^{22+}	H-like
K	Stout	Ca^{16+}	Chianti	Ti^{10+}	Chianti	Cr	...
K^{+}	Stout	Ca^{17+}	Chianti	Ti^{11+}	Chianti	Cr^{+}	Stout
K^{2+}	Stout	Ca^{18+}	He-like	Ti^{12+}	Stout	Cr^{2+}	...
K^{3+}	Stout	Ca^{19+}	H-like	Ti^{13+}	Chianti	Cr^{3+}	Stout
Cr^{4+}	Stout	Mn^{15+}	Stout	Fe^{25+}	H-like	Ni^{6+}	Stout
Cr^{5+}	...	Mn^{16+}	Chianti	Co	...	Ni^{7+}	...
Cr^{6+}	Chianti	Mn^{17+}	Chianti	Co^{+}	...	Ni^{8+}	Stout
Cr^{7+}	Chianti	Mn^{18+}	Chianti	Co^{+}	Stout	Ni^{9+}	...
Cr^{8+}	Chianti	Mn^{19+}	Chianti	Co^{2+}	Stout	Ni^{10+}	Stout
Cr^{9+}	Stout	Mn^{20+}	Chianti	Co^{3+}	...	Ni^{11+}	Chianti
Cr^{10+}	Stout	Mn^{21+}	Chianti	Co^{4+}	...	Ni^{12+}	Chianti
Cr^{11+}	Stout	Mn^{22+}	Chianti	Co^{5+}	...	Ni^{13+}	Chianti
Cr^{12+}	Chianti	Mn^{23+}	He-like	Co^{6+}	...	Ni^{14+}	Stout
Cr^{13+}	Chianti	Mn^{24+}	H-like	Co^{7+}	Stout	Ni^{15+}	Chianti
Cr^{14+}	Stout	Fe	Stout	Co^{8+}	...	Ni^{16+}	Chianti
Cr^{15+}	Chianti	Fe^{+}	Stout	Co^{9+}	Stout	Ni^{17+}	Chianti
Cr^{16+}	Chianti	Fe^{2+}	Stout	Co^{10+}	Stout	Ni^{18+}	Chianti
Cr^{17+}	Chianti	Fe^{3+}	Chianti	Co^{11+}	Stout	Ni^{19+}	Chianti

TABLE 8 (CONTINUED)

Species	Database	Species	Database	Species	Database	Species	Database
Cr^{18+}	Chianti	Fe^{4+}	Chianti	Co^{12+}	Stout	Ni^{20+}	Chianti
Cr^{19+}	Chianti	Fe^{5+}	Chianti	Co^{13+}	Stout	Ni^{21+}	Chianti
Cr^{20+}	Chianti	Fe^{6+}	Stout	Co^{14+}	Stout	Ni^{22+}	Chianti
Cr^{21+}	Chianti	Fe^{7+}	Chianti	Co^{15+}	Stout	Ni^{23+}	Chianti
Cr^{22+}	He-like	Fe^{8+}	Stout	Co^{16+}	Chianti	Ni^{24+}	Chianti
Cr^{23+}	H-like	Fe^{9+}	Chianti	Co^{17+}	Stout	Ni^{25+}	Chianti
Mn	Stout	Fe^{10+}	Chianti	Co^{18+}	Chianti	Ni^{26+}	He-like
Mn^{+}	. . .	Fe^{11+}	Chianti	Co^{19+}	Chianti	Ni^{27+}	H-like
Mn^{2+}	. . .	Fe^{12+}	Chianti	Co^{20+}	Chianti	Cu	Stout
Mn^{3+}	. . .	Fe^{13+}	Chianti	Co^{21+}	Chianti	Cu^{+}	. . .
Mn^{4+}	Stout	Fe^{14+}	Chianti	Co^{22+}	Chianti	Cu^{2+}	. . .
Mn^{5+}	Stout	Fe^{15+}	Chianti	Co^{23+}	Chianti	Cu^{3+}	. . .
Mn^{6+}	. . .	Fe^{16+}	Chianti	Co^{24+}	Chianti	Cu^{4+}	. . .
Mn^{7+}	Chianti	Fe^{17+}	Chianti	Co^{25+}	He-like	Cu^{5+}	. . .
Mn^{8+}	Chianti	Fe^{18+}	Chianti	Co^{26+}	H-like	Cu^{6+}	. . .
Mn^{9+}	Chianti	Fe^{19+}	Chianti	Ni	Stout	Cu^{7+}	. . .
Mn^{10+}	Stout	Fe^{20+}	Chianti	Ni^{+}	Chianti	Cu^{8+}	. . .
Mn^{11+}	Stout	Fe^{21+}	Chianti	Ni^{2+}	Stout	Cu^{9+}	. . .
Mn^{12+}	Stout	Fe^{22+}	Chianti	Ni^{3+}	Stout	Cu^{10+}	. . .
Mn^{13+}	Stout	Fe^{23+}	Chianti	Ni^{4+}	Stout	Cu^{11+}	. . .
Mn^{14+}	Chianti	Fe^{24+}	He-like	Ni^{5+}	. . .	Cu^{12+}	Stout
Cu^{13+}	Stout	Zn^{19+}	Chianti	CN	LAMDA	HTiS	. . .
Cu^{14+}	Stout	Zn^{20+}	. . .	CN^{+}	. . .	$HTiS^{+}$	. . .
Cu^{15+}	Stout	Zn^{21+}	. . .	CO	LAMDA	HeH^{+}	. . .
Cu^{16+}	Stout	Zn^{22+}	Chianti	CS	LAMDA	Li^{-}	. . .
Cu^{17+}	Stout	Zn^{23+}	Chianti	CS^{+}	. . .	LiH	. . .
Cu^{18+}	. . .	Zn^{24+}	Chianti	ClO	. . .	LiH^{+}	. . .
Cu^{19+}	. . .	Zn^{25+}	. . .	ClO^{+}	. . .	N_2	. . .
Cu^{20+}	Stout	Zn^{26+}	Chianti	H^{-}	. . .	N_2^{+}	. . .
Cu^{21+}	Stout	Zn^{27+}	Chianti	H_2	. . .	N_2H^{+}	LAMDA
Cu^{22+}	Stout	Zn^{28+}	He-like	$H_2^{\star}$	. . .	N_2O	. . .
Cu^{23+}	Stout	Zn^{29+}	H-like	H_2^{+}	. . .	NH	. . .
Cu^{24+}	Stout	ArH^{+}	. . .	H_2CCl^{+}	. . .	NH^{+}	. . .
Cu^{25+}	. . .	C_2	. . .	H_2CO	LAMDA	NH_2	. . .
Cu^{26+}	. . .	C_2^{+}	. . .	H_2Cl^{+}	. . .	NH_2^{+}	. . .
Cu^{27+}	He-like	C_2H	LAMDA	H_2O	LAMDA	NH_3	LAMDA
Cu^{28+}	H-like	C_2H^{+}	. . .	H_2O^{+}	. . .	NH_3^{+}	. . .
Zn	. . .	C_2H_2	. . .	H_3^{+}	. . .	NH_4^{+}	. . .
Zn^{+}	Stout	$C_2H_2^{+}$	. . .	H_3O^{+}	LAMDA	NO	LAMDA
Zn^{2+}	. . .	$C_2H_3^{+}$	. . .	HC_3N	LAMDA	NO^{+}	. . .
Zn^{3+}	Stout	C_3	. . .	HCN	LAMDA	NO_2	. . .
Zn^{4+}	. . .	C_3^{+}	. . .	HCN^{+}	. . .	NO_2^{+}	. . .
Zn^{5+}	. . .	C_3H	. . .	$HCNH^{+}$	. . .	NS	. . .

TABLE 8 (CONTINUED)

Species	Database	Species	Database	Species	Database	Species	Database
Zn^{6+}	. . .	C_3H^+	. . .	HCO^+	LAMDA	NS^+	. . .
Zn^{7+}	. . .	CCl	. . .	HCS^+	LAMDA	NeH^+	. . .
Zn^{8+}	. . .	CCl^+	. . .	HCTi	. . .	O_2	LAMDA
Zn^{9+}	. . .	CH	. . .	$HCTi^+$	. . .	O_2^+	. . .
Zn^{10+}	. . .	CH^+	. . .	HCl	LAMDA	OCN	. . .
Zn^{11+}	. . .	CH_2	. . .	HCl^+	. . .	OCN^+	. . .
Zn^{12+}	. . .	CH_2^+	. . .	HNC	LAMDA	OCS	LAMDA
Zn^{13+}	. . .	CH_3	. . .	HNO	. . .	OCS^+	. . .
Zn^{14+}	. . .	CH_3^+	. . .	HNO^+	. . .	OH	LAMDA
Zn^{15+}	. . .	CH_3OH	LAMDA	HNTi	. . .	OH^+	LAMDA
Zn^{16+}	. . .	CH_4	. . .	$HNTi^+$	. . .	S_2	. . .
Zn^{17+}	. . .	CH_4^+	. . .	HS	. . .	S_2^+	. . .
Zn^{18+}	Stout	CH_5^+	. . .	HS^+	. . .	SO	LAMDA
SO^+	. . .	SiO^+	. . .	TiH^+	. . .	TiO^+	. . .
SO_2	LAMDA	$SiOH^+$	. . .	TiH_2	. . .	TiO_2	. . .
SiC_2	LAMDA	TiC	. . .	TiH_2^+	. . .	$TiOH^+$	. . .
SiH	. . .	TiC^+	. . .	TiN	. . .	TiS	. . .
SiH_2^+	. . .	TiC_2	. . .	TiN^+	. . .	TiS^+	. . .
SiN	. . .	TiC_2^+	. . .	TiNC	. . .	^{13}CO	LAMDA
SiN^+	. . .	TiF^+	. . .	$TiNC^+$	. . .		
SiO	LAMDA	TiH	. . .	TiO	. . .		

TABLE 9

REFERENCES FOR STOUT DATABASE. SPECIES MARKED WITH ‡ ARE LISTED IN STOUT.INI, THE DEFAULT MASTERLIST

Species	Energy	Transition	Collision
Li ‡	NIST 2013-11-08	NIST 2013-10-18	baseline
Be ‡	NIST 2014-09-16	NIST 2014-09-16	baseline
Be^+ ‡	NIST 2013-11-08	NIST 2013-10-18	baseline
B ‡	NIST 2013-10-18	NIST 2013-10-18	baseline
B^+ ‡	NIST 2014-09-16	NIST 2014-09-16	baseline
B^{2+} ‡	NIST 2014-09-16	NIST 2014-09-16	baseline
C ‡	NIST 2013-10-01	NIST 2013-10-01	Johnson et al. (1987)
			Mendoza (1983)
			Abrahamsson et al. (2007)
			Roueff & Le Bourlot (1990)
			Schroder et al. (1991)
			Staemmler & Flower (1991)
C^+ ‡	NIST 2013-10-01	NIST 2013-10-01	Goldsmith et al. (2012)
			Wiesenfeld & Goldsmith (2014)
			Tayal (2008)
C^{2+} ‡	NIST 2013-11-08	NIST 2013-10-20	Berrington et al. (1985)
	Fernández-Menchero et al. (2014a)	Fernández-Menchero et al. (2014a)	Fernández-Menchero et al. (2014a)
C^{3+}	NIST 2014-09-16	NIST 2014-09-16	baseline
N ‡	NIST 2013-12-05	Froese Fischer & Tachiev (2004) NIST 2013-12-05	Tayal (2006)
N^+	NIST 2014-09-16	NIST 2014-09-16	baseline
N^{2+}	NIST 2014-09-16	NIST 2014-09-16	baseline
N^{3+}	NIST 2014-09-16	NIST 2014-09-16	baseline
N^{4+} ‡	NIST 2013-12-05	NIST 2013-12-05	baseline
O ‡	NIST 2014-01-09	NIST 2014-01-09	Bell et al. (1998)
			Barklem (2007)
			Abrahamsson et al. (2007)
			Krems et al. (2006)
			Monteiro & Flower (1987)
			Jaquet et al. (1992)
			Pequignot (1990)
			Wang & McConkey (1992)
O^+ ‡	NIST 2014-01-26	Froese Fischer & Tachiev (2004) NIST 2014-01-26	Kisielius et al. (2009)
O^{2+} ‡	NIST 2014-09-16	NIST	Aggarwal (1983)
		Galavis et al. (1997)	Aggarwal (1985)
		Storey & Zeippen (2000)	Bhatia & Kastner (1993)
		Tachiev & Froese Fischer (2001)	Lennon & Burke (1994)
			Storey et al. (2014)
O^{4+}	NIST 2014-09-16	NIST 2014-09-16	Fernández-Menchero et al. (2014a)
	Fernández-Menchero et al. (2014a)	Fernández-Menchero et al. (2014a)	
O^{5+}	NIST 2014-09-16	NIST 2014-09-16	baseline

TABLE 9 (CONTINUED)

Species	Energy	Transition	Collision
F^+ ‡	NIST 2013-10-01	NIST 2013-10-01	Butler & Zeippen (1994)
F^{2+} ‡	NIST 2014-09-16	NIST 2014-09-16	baseline
F^{3+} ‡	NIST 2013-10-01	NIST 2013-10-01	Lennon & Burke (1994)
F^{4+} ‡	NIST 2014-09-16	NIST 2014-09-16	baseline
F^{5+} ‡	NIST 2014-09-16	NIST 2014-09-16	Fernández-Menchero et al. (2014a)
	Fernández-Menchero et al. (2014a)	Fernández-Menchero et al. (2014a)	
F^{6+} ‡	NIST 2014-09-16	NIST 2014-09-16	baseline
Ne ‡	NIST 2014-09-16	NIST 2014-09-16	baseline
Ne^+ ‡	NIST 2013-10-01	NIST 2013-10-01	Griffin et al. (2001)
			Hollenbach & McKee (1989)
Ne^{2+} ‡	NIST	McLaughlin et al. (2011)	McLaughlin et al. (2011)
	McLaughlin et al. (2011)		
Ne^{3+}	NIST 2014-09-16	NIST 2014-09-16	baseline
Ne^{4+}	NIST 2014-09-16	NIST 2014-09-16	baseline
Ne^{6+}	NIST 2014-09-16	NIST 2014-09-16	baseline
Ne^{7+}	NIST 2014-09-16	NIST 2014-09-16	baseline
Na ‡	NIST 2013-10-01	NIST 2013-10-01	Verner, private communication
Na^+ ‡	NIST 2014-09-16	NIST 2014-09-16	baseline
Na^{2+}	NIST 2014-09-16	NIST 2014-09-16	baseline
Na^{3+}	NIST 2014-09-16	NIST 2014-09-16	baseline
Na^{4+}	NIST 2014-09-16	NIST 2014-09-16	baseline
Na^{5+}	NIST 2014-09-16	NIST 2014-09-16	baseline
Na^{6+}	NIST 2014-09-16	NIST 2014-09-16	baseline
Na^{7+}	NIST 2014-09-16	NIST 2014-09-16	baseline
Na^{8+}	NIST 2014-09-16	NIST 2014-09-16	baseline
Mg ‡	NIST 2013-10-01	NIST 2013-10-01	Barklem et al. (2012)
			Osorio et al. (2015)
Mg^+	NIST 2014-09-16	NIST 2014-09-16	baseline
Mg^{2+} ‡	NIST 2013-10-01	NIST 2013-10-01	Liang & Badnell (2010)
			NIST 2013-09-07
Mg^{3+}	NIST 2014-09-16	NIST 2014-09-16	baseline
Mg^{4+}	NIST 2014-09-16	NIST 2014-09-16	baseline
Mg^{5+}	NIST 2014-09-16	NIST 2014-09-16	baseline
Mg^{6+}	NIST 2014-09-16	NIST 2014-09-16	baseline
Mg^{7+}	NIST 2014-09-16	NIST 2014-09-16	baseline
Mg^{8+}	NIST 2014-09-16	NIST 2014-09-16	baseline
Mg^{9+}	NIST 2014-09-16	NIST 2014-09-16	baseline
Al ‡	NIST 2013-10-01	NIST 2013-10-01	baseline
Al^+	NIST 2014-09-16	NIST 2014-09-16	baseline
Al^{2+} ‡	NIST 2013-10-01	NIST 2013-10-01	Dufton & Kingston (1987)
Al^{3+} ‡	NIST 2014-09-16	NIST 2014-09-16	baseline
Al^{4+}	NIST 2014-09-16	NIST 2014-09-16	baseline
Al^{5+} ‡	NIST 2014-05-24	NIST 2014-05-24	Butler & Zeippen (1994)
Al^{6+}	NIST 2014-09-16	NIST 2014-09-16	baseline
Al^{7+}	NIST 2014-09-16	NIST 2014-09-16	baseline

TABLE 9 (CONTINUED)

Species	Energy	Transition	Collision
Al^{8+}	NIST 2014-09-16	NIST 2014-09-16	baseline
Al^{9+}	NIST 2014-09-16	NIST 2014-09-16	baseline
Al^{10+}	NIST 2014-09-16	NIST 2014-09-16	baseline
Si ‡	NIST 2013-10-01	NIST 2013-10-01	Hollenbach & McKee (1989)
Si^+ ‡	NIST 2014-08-01	Laha et al. (2016)	Aggarwal & Keenan (2014)
	Laha et al. (2016)		Barinovs et al. (2005)
			Laha et al. (2016)
Si^{2+} ‡	Fernández-Menchero et al. (2014b)	Kwong et al. (1983)	Fernández-Menchero et al. (2014b)
	NIST	Fernández-Menchero et al. (2014b)	
Si^{3+} ‡	NIST 2013-10-01	NIST 2013-10-01	Liang et al. (2009)
Si^{4+}	NIST 2014-09-16	NIST 2014-09-16	baseline
Si^{5+}	NIST 2014-09-16	NIST 2014-09-16	baseline
Si^{6+} ‡	NIST 2014-05-24	NIST 2014-05-24	Butler & Zeippen (1994)
Si^{7+}	NIST 2014-09-16	NIST 2014-09-16	baseline
Si^{8+} ‡	NIST 2013-10-01	NIST 2013-10-01	Lennon & Burke (1994)
Si^{9+}	NIST 2014-09-16	NIST 2014-09-16	baseline
Si^{10+}	NIST 2014-09-16	NIST 2014-09-16	baseline
Si^{11+}	NIST 2014-09-16	NIST 2014-09-16	baseline
P ‡	NIST 2013-10-18	NIST 2013-10-18	baseline
P^+ ‡	NIST 2013-10-01	NIST 2013-10-01	Krueger & Czyzak (1970)
P^{2+} ‡	NIST 2013-10-01	NIST 2013-10-01	Krueger & Czyzak (1970)
P^{3+} ‡	NIST 2014-09-16	NIST 2014-09-16	baseline
P^{4+}	NIST 2014-09-16	NIST 2014-09-16	baseline
P^{5+} ‡	NIST 2014-09-16	NIST 2014-09-16	baseline
P^{6+}	NIST 2014-09-16	NIST 2014-09-16	baseline
P^{7+}	NIST 2014-09-16	NIST 2014-09-16	baseline
P^{8+}	NIST 2014-09-16	NIST 2014-09-16	baseline
P^{11+}	NIST 2014-09-16	NIST 2014-09-16	baseline
P^{12+}	NIST 2014-09-16	NIST 2014-09-16	baseline
S ‡	NIST 2013-10-01	NIST 2013-10-01	Hollenbach & McKee (1989)
S^+ ‡	NIST	Kisielius et al. (2014)	Tayal & Zatsarinny (2010)
S^{2+} ‡		Froese Fischer et al. (2006)	Hudson et al. (2012b)
		Tayal (1997)	
		Podobedova et al. (2009)	
		Heise et al. (1995)	
S^{3+}	NIST 2014-09-16	NIST 2014-09-16	baseline
S^{4+}	NIST 2014-09-16	NIST 2014-09-16	baseline
S^{5+}	NIST 2014-09-16	NIST 2014-09-16	baseline
S^{6+}	NIST 2014-09-16	NIST 2014-09-16	baseline
S^{7+}	NIST 2014-09-16	NIST 2014-09-16	baseline
S^{8+}	NIST 2014-09-16	NIST 2014-09-16	baseline
S^{9+}	NIST 2014-09-16	NIST 2014-09-16	baseline
S^{10+}	NIST 2014-09-16	NIST 2014-09-16	baseline
S^{11+}	NIST 2014-09-16	NIST 2014-09-16	baseline
S^{12+}	NIST 2014-09-16	NIST 2014-09-16	baseline

TABLE 9 (CONTINUED)

Species	Energy	Transition	Collision
S^{13+}	NIST 2014-09-16	NIST 2014-09-16	baseline
Cl ‡	NIST 2013-10-01	NIST 2013-10-01	Hollenbach & McKee (1989)
Cl$^+$	NIST 2014-09-16	NIST 2014-09-16	baseline
Cl^{2+}	NIST 2014-09-16	NIST 2014-09-16	baseline
Cl^{3+}	NIST 2014-09-16	NIST 2014-09-16	baseline
Cl^{4+} ‡	NIST 2014-09-16	NIST 2014-09-16	baseline
Cl^{5+} ‡	NIST	Fernández-Menchero et al. (2014b)	Fernández-Menchero et al. (2014b)
	Fernández-Menchero et al. (2014b)		
Cl^{6+} ‡	Liang et al. (2009)	Liang et al. (2009)	Liang et al. (2009)
Cl^{7+} ‡	Liang & Badnell (2010)	Liang & Badnell (2010)	Liang & Badnell (2010)
Cl^{8+} ‡	NIST 2013-10-01	NIST 2013-10-01	Berrington et al. (1998)
Cl^{9+}	NIST 2014-09-16	NIST 2014-09-16	baseline
Ar ‡	NIST 2013-11-08	NIST 2013-10-01	baseline
Ar$^+$ ‡	NIST 2013-10-01	NIST 2013-10-01	Pelan & Berrington (1995)
Ar^{2+} ‡	NIST 2013-10-01	NIST 2013-10-01	Galavis et al. (1995)
Ar^{3+} ‡	NIST 2013-10-01	NIST 2013-10-01	Ramsbottom et al. (1997)
Ar^{4+} ‡	NIST 2013-10-01	NIST 2013-10-01	Galavis et al. (1995)
Ar^{5+} ‡	NIST 2013-10-01	NIST 2013-10-01	Saraph & Storey (1996)
Ar^{6+}	NIST 2014-09-16	NIST 2014-09-16	baseline
Ar^{7+}	NIST 2014-09-16	NIST 2014-09-16	baseline
Ar^{8+}	NIST 2014-09-16	NIST 2014-09-16	baseline
Ar^{9+}	NIST 2014-09-16	NIST 2014-09-16	baseline
Ar^{10+}	NIST 2014-09-16	NIST 2014-09-16	baseline
Ar^{12+}	NIST 2014-09-16	NIST 2014-09-16	baseline
Ar^{13+}	NIST 2014-09-16	NIST 2014-09-16	baseline
K ‡	NIST 2013-10-01	NIST 2013-10-01	baseline
K$^+$ ‡	NIST 2014-09-16	NIST 2014-09-16	baseline
K^{2+} ‡	NIST 2013-10-01	NIST 2013-10-01	Pelan & Berrington (1995)
K^{3+} ‡	NIST 2013-10-01	NIST 2013-10-01	Galavis et al. (1995)
K^{4+}	NIST 2014-09-16	NIST 2014-09-16	baseline
K^{5+}	NIST 2014-09-16	NIST 2014-09-16	baseline
K^{6+} ‡	NIST 2013-10-01	NIST 2013-10-01	Saraph & Storey (1996)
K^{7+} ‡	NIST	Fernández-Menchero et al. (2014b)	Fernández-Menchero et al. (2014b)
	Fernández-Menchero et al. (2014b)		
K^{8+}	NIST 2014-09-16	NIST 2014-09-16	baseline
K^{9+} ‡	NIST 2014-09-16	NIST 2014-09-16	baseline
K^{10+}	NIST 2014-09-16	NIST 2014-09-16	baseline
K^{11+}	NIST 2014-09-16	NIST 2014-09-16	baseline
K^{12+}	NIST 2014-09-16	NIST 2014-09-16	baseline
K^{13+}	NIST 2014-09-16	NIST 2014-09-16	baseline
K^{14+}	NIST 2014-09-16	NIST 2014-09-16	baseline
K^{15+}	NIST 2014-09-16	NIST 2014-09-16	baseline
K^{16+}	NIST 2014-09-16	NIST 2014-09-16	baseline

TABLE 9 (CONTINUED)

Species	Energy	Transition	Collision
Ca ‡	NIST 2013-10-01	NIST 2013-10-01	baseline
Ca$^+$	NIST 2014-09-16	NIST 2014-09-16	baseline
Ca^{2+} ‡	NIST 2014-09-16	NIST 2014-09-16	baseline
Ca^{3+} ‡	NIST 2013-10-01	NIST 2013-10-01	Pelan & Berrington (1995)
Ca^{4+}	NIST 2014-09-16	NIST 2014-09-16	baseline
Ca^{5+} ‡	NIST 2014-09-16	NIST 2014-09-16	baseline
Ca^{6+}	NIST 2014-09-16	NIST 2014-09-16	baseline
Ca^{7+}	NIST 2014-09-16	NIST 2014-09-16	baseline
Ca^{9+}	NIST 2014-09-16	NIST 2014-09-16	baseline
Ca^{10+}	NIST 2014-09-16	NIST 2014-09-16	baseline
Ca^{11+}	NIST 2014-09-16	NIST 2014-09-16	baseline
Ca^{12+}	NIST 2014-09-16	NIST 2014-09-16	baseline
Ca^{14+}	NIST 2014-09-16	NIST 2014-09-16	baseline
Sc ‡	NIST 2013-10-18	NIST 2013-10-18	baseline
Sc$^+$ ‡	NIST 2013-10-01	NIST 2013-10-01	Wasson et al. (2011)
Sc^{2+} ‡	NIST 2013-10-01	NIST 2013-10-01	baseline
Sc^{3+} ‡	NIST 2014-09-16	NIST 2014-09-16	baseline
Sc^{4+} ‡	NIST 2013-10-01	NIST 2013-10-01	Pelan & Berrington (1995)
Sc^{5+} ‡	NIST 2013-10-01	NIST 2013-10-01	baseline
Sc^{6+} ‡	NIST 2014-09-16	NIST 2014-09-16	baseline
Sc^{7+} ‡	NIST 2014-09-16	NIST 2014-09-16	baseline
Sc^{8+} ‡	NIST 2014-09-16	NIST 2014-09-16	baseline
V^{10+} ‡	NIST 2014-09-16	NIST 2014-09-16	baseline
V^{11+} ‡	NIST	Fernández-Menchero et al. (2014b)	Fernández-Menchero et al. (2014b)
V^{12+} ‡	NIST 2014-09-16	NIST 2014-09-16	baseline
V^{14+} ‡	NIST	NIST	Berrington et al. (1998)
	NIST	NIST	
V^{15+} ‡	NIST 2014-09-16	NIST 2014-09-16	baseline
V^{16+} ‡	NIST 2014-09-16	NIST 2014-09-16	baseline
V^{17+} ‡	NIST 2014-09-16	NIST 2014-09-16	baseline
V^{18+} ‡	NIST 2014-09-16	NIST 2014-09-16	baseline
V^{19+} ‡	NIST 2014-09-16	NIST 2014-09-16	baseline
V^{20+} ‡	NIST 2014-09-16	NIST 2014-09-16	baseline
Cr$^+$ ‡	NIST 2013-10-01	NIST 2013-10-01	Grieve & Ramsbottom (2012)
Cr^{3+} ‡	NIST 2013-10-01	NIST 2013-10-01	baseline
Cr^{4+} ‡	NIST 2013-10-01	NIST 2013-10-01	baseline
Cr^{6+}	NIST 2014-09-16	NIST 2014-09-16	baseline
Cr^{8+}	NIST 2014-09-16	NIST 2014-09-16	baseline
Cr^{9+} ‡	NIST 2014-09-16	NIST 2014-09-16	baseline
Cr^{10+} ‡	NIST 2014-09-16	NIST 2014-09-16	baseline
Cr^{11+} ‡	NIST 2014-09-16	NIST 2014-09-16	baseline
Cr^{12+}	NIST 2014-09-16	NIST 2014-09-16	baseline
Cr^{13+}	NIST 2014-09-16	NIST 2014-09-16	baseline
Cr^{14+} ‡	NIST 2014-09-16	NIST 2014-09-16	baseline
Cr^{15+}	NIST 2014-09-16	NIST 2014-09-16	baseline
Cr^{16+}	NIST 2014-09-16	NIST 2014-09-16	baseline

TABLE 9 (CONTINUED)

Species	Energy	Transition	Collision
Cr^{17+}	NIST 2014-09-16	NIST 2014-09-16	baseline
Cr^{18+}	NIST 2014-09-16	NIST 2014-09-16	baseline
Cr^{19+}	NIST 2014-09-16	NIST 2014-09-16	baseline
Cr^{20+}	NIST 2014-09-16	NIST 2014-09-16	baseline
Cr^{21+}	NIST 2014-09-16	NIST 2014-09-16	baseline
Mn ‡	NIST 2013-11-08	NIST 2013-10-18	baseline
Mn^{4+} ‡	NIST 2014-09-16	NIST 2014-09-16	baseline
Mn^{5+} ‡	NIST 2014-09-16	NIST 2014-09-16	baseline
Mn^{7+}	NIST 2014-09-16	NIST 2014-09-16	baseline
Mn^{8+}	NIST 2014-09-16	NIST 2014-09-16	baseline
Mn^{9+}	NIST 2014-09-16	NIST 2014-09-16	baseline
Mn^{10+} ‡	NIST 2014-09-16	NIST 2014-09-16	baseline
Mn^{11+} ‡	NIST 2014-09-16	NIST 2014-09-16	baseline
Mn^{12+} ‡	NIST 2014-09-16	NIST 2014-09-16	baseline
Mn^{13+} ‡	NIST	Fernández-Menchero et al. (2014b)	Fernández-Menchero et al. (2014b)
	Fernández-Menchero et al. (2014b)		
Mn^{14+}	NIST 2014-09-16	NIST 2014-09-16	baseline
Mn^{15+} ‡	NIST 2014-09-16	NIST 2014-09-16	baseline
Mn^{16+}	NIST 2014-09-16	NIST 2014-09-16	baseline
Mn^{17+}	NIST 2014-09-16	NIST 2014-09-16	baseline
Mn^{18+}	NIST 2014-09-16	NIST 2014-09-16	baseline
Mn^{19+}	NIST 2014-09-16	NIST 2014-09-16	baseline
Mn^{20+}	NIST 2014-09-16	NIST 2014-09-16	baseline
Mn^{21+}	NIST 2014-09-16	NIST 2014-09-16	baseline
Mn^{22+}	NIST 2014-09-16	NIST 2014-09-16	baseline
Fe ‡	NIST 2013-10-18	NIST 2013-10-18	Hollenbach & McKee (1989)
Fe^{+}	Verner et al. (1999)	Verner et al. (1999)	Verner et al. (1999)
Fe^{2+} ‡	Zhang (1996)	Zhang (1996)	Zhang (1996)
Fe^{3+}	NIST 2014-09-16	NIST 2014-09-16	baseline
Fe^{4+}	NIST 2014-09-16	NIST 2014-09-16	baseline
Fe^{5+}	NIST 2014-09-16	NIST 2014-09-16	baseline
Fe^{6+} ‡	Witthoeft & Badnell (2008)	Witthoeft & Badnell (2008)	Witthoeft & Badnell (2008)
Fe^{8+}	NIST 2014-09-16	NIST 2014-09-16	Del Zanna et al. (2014b)
	Del Zanna et al. (2014b)	Del Zanna et al. (2014b)	
Fe^{9+}	NIST 2014-09-16	NIST 2014-09-16	baseline
Fe^{10+}	NIST 2014-09-16	NIST 2014-09-16	baseline
Fe^{12+}	NIST 2014-09-16	NIST 2014-09-16	baseline
Fe^{13+}	NIST 2014-09-16	NIST 2014-09-16	baseline
Fe^{14+}	NIST 2014-09-16	NIST 2014-09-16	baseline
Fe^{15+}	NIST 2014-09-16	NIST 2014-09-16	baseline
Fe^{16+}	NIST 2014-09-16	NIST 2014-09-16	baseline
Fe^{17+}	NIST 2014-09-16	NIST 2014-09-16	baseline
Fe^{18+}	NIST 2014-09-16	NIST 2014-09-16	baseline
Fe^{19+}	NIST 2014-09-16	NIST 2014-09-16	baseline
Fe^{20+}	NIST 2014-09-16	NIST 2014-09-16	baseline
Fe^{21+}	NIST 2014-09-16	NIST 2014-09-16	baseline

TABLE 9 (CONTINUED)

Species	Energy	Transition	Collision
Fe^{22+}	NIST 2014-09-16	NIST 2014-09-16	baseline
Fe^{23+}	NIST 2014-09-16	NIST 2014-09-16	baseline
Co^+ ‡	NIST 2014-09-16	NIST 2014-09-16	Storey et al. (2015)
		Storey et al. (2015)	
Co^{2+} ‡	NIST 2014-09-16	NIST 2014-09-16	Storey & Sochi (2016)
		Storey & Sochi (2016)	
Co^{7+} ‡	NIST 2014-09-16	NIST 2014-09-16	baseline
Co^{9+} ‡	NIST 2014-09-16	NIST 2014-09-16	baseline
Co^{10+} ‡	NIST 2013-10-01	NIST 2013-10-01	Pelan & Berrington (1995)
Co^{11+} ‡	NIST 2014-09-16	NIST 2014-09-16	baseline
Co^{12+} ‡	NIST 2014-09-16	NIST 2014-09-16	baseline
Co^{13+} ‡	NIST 2014-09-16	NIST 2014-09-16	baseline
Co^{14+} ‡	NIST 2014-09-16	NIST 2014-09-16	baseline
Co^{15+} ‡	NIST 2014-09-16	NIST 2014-09-16	baseline
Co^{16+}	NIST 2014-09-16	NIST 2014-09-16	baseline
Co^{17+} ‡	NIST 2014-09-16	NIST 2014-09-16	baseline
Co^{18+}	NIST 2014-09-16	NIST 2014-09-16	baseline
Co^{19+}	NIST 2014-09-16	NIST 2014-09-16	baseline
Co^{20+}	NIST 2014-09-16	NIST 2014-09-16	baseline
Co^{21+}	NIST 2014-09-16	NIST 2014-09-16	baseline
Co^{22+}	NIST 2014-09-16	NIST 2014-09-16	baseline
Co^{23+}	NIST 2014-09-16	NIST 2014-09-16	baseline
Co^{24+}	NIST 2014-09-16	NIST 2014-09-16	baseline
Ni ‡	NIST 2013-10-01	NIST 2013-10-01	Hollenbach & McKee (1989)
Ni^+	NIST 2013-10-01	NIST 2013-10-01	Cassidy et al. (2011)
Ni^{2+} ‡	NIST 2014-09-16	NIST 2014-09-16	baseline
Ni^{3+} ‡	NIST 2014-09-16	NIST 2014-09-16	baseline
Ni^{4+} ‡	NIST 2014-09-16	NIST 2014-09-16	baseline
Ni^{6+} ‡	NIST 2014-09-16	NIST 2014-09-16	baseline
Ni^{8+} ‡	NIST 2014-09-16	NIST 2014-09-16	baseline
Ni^{10+}	NIST 2014-09-16	NIST 2014-09-16	Del Zanna et al. (2014a)
	Del Zanna et al. (2014a)	Del Zanna et al. (2014a)	
Ni^{11+}	NIST 2014-09-16	NIST 2014-09-16	baseline
Ni^{12+}	NIST 2014-09-16	NIST 2014-09-16	baseline
Ni^{13+}	NIST 2014-09-16	NIST 2014-09-16	baseline
Ni^{14+}	Del Zanna et al. (2014c)	Del Zanna et al. (2014c)	Del Zanna et al. (2014c)
	NIST		
Ni^{15+}	NIST 2014-09-16	NIST 2014-09-16	baseline
Ni^{16+}	Aggarwal et al. (2007)	Aggarwal et al. (2007)	Hudson et al. (2012a)
Ni^{17+}	NIST 2014-09-16	NIST 2014-09-16	baseline
Ni^{18+}	NIST 2014-09-16	NIST 2014-09-16	baseline
Ni^{19+}	NIST 2014-09-16	NIST 2014-09-16	baseline
Ni^{20+}	NIST 2014-09-16	NIST 2014-09-16	baseline
Ni^{21+}	NIST 2014-09-16	NIST 2014-09-16	baseline
Ni^{22+}	NIST 2014-09-16	NIST 2014-09-16	baseline
Ni^{23+}	NIST 2014-09-16	NIST 2014-09-16	baseline
Ni^{24+}	NIST 2014-09-16	NIST 2014-09-16	baseline

TABLE 9 (CONTINUED)

Species	Energy	Transition	Collision
Ni^{25+}	NIST 2014-09-16	NIST 2014-09-16	baseline
Cu ‡	NIST 2014-09-16	NIST 2014-09-16	baseline
Cu^{12+} ‡	NIST 2014-09-16	NIST 2014-09-16	baseline
Cu^{13+} ‡	NIST 2014-09-16	NIST 2014-09-16	baseline
Cu^{14+} ‡	NIST 2014-09-16	NIST 2014-09-16	baseline
Cu^{15+} ‡	NIST 2014-09-16	NIST 2014-09-16	baseline
Cu^{16+} ‡	NIST 2014-09-16	NIST 2014-09-16	baseline
Cu^{17+} ‡	NIST	Fernández-Menchero et al. (2014b)	Fernández-Menchero et al. (2014b)
	Fernández-Menchero et al. (2014b)		
Cu^{20+} ‡	NIST 2014-09-16	NIST 2014-09-16	baseline
Cu^{21+} ‡	NIST 2014-09-16	NIST 2014-09-16	baseline
Cu^{22+} ‡	NIST 2014-09-16	NIST 2014-09-16	baseline
Cu^{23+} ‡	NIST 2014-09-16	NIST 2014-09-16	baseline
Cu^{24+} ‡	NIST 2014-09-16	NIST 2014-09-16	baseline
Zn^{+} ‡	NIST	Kisielius et al. (2015)	Kisielius et al. (2015)
Zn^{3+} ‡	NIST		baseline
Zn^{18+} ‡	NIST	Fernández-Menchero et al. (2014b)	Fernández-Menchero et al. (2014b)
	Fernández-Menchero et al. (2014b)		

REFERENCES

Abel, N. P., Ferland, G. J., O'Dell, C. R., & Troland, T. H. 2016, ApJ, 819, 136

Abel, N. P., Ferland, G. J., Shaw, G., & van Hoof, P. A. M. 2005, ApJS, 161, 65

Abel, N. P., Hoof, P. A. M. v., Shaw, G., Ferland, G. J., & Elwert, T. 2008, ApJ, 686, 1125

Abrahamsson, E., Krems, R. V., & Dalgarno, A. 2007, ApJ, 654, 1171

Aggarwal, K. M. 1983, ApJS, 52, 387

_____. 1985, A&A, 146, 149

Aggarwal, K. M., & Keenan, F. P. 2014, MNRAS, 442, 388

Aggarwal, K. M., Tayal, V., Gupta, G. P., & Keenan, F. P. 2007, Atomic Data and Nuclear Data Tables, 93, 615

Aller, L. H. 1963, Astrophysics. The atmospheres of the sun and stars (New York: Ronald Press)

Arnaud, M., & Rothenflug, R. 1985, A&AS, 60, 425

Asplund, M., Grevesse, N., Sauval, A. J., & Scott, P. 2009, ARA&A, 47, 481

Badnell, N. R. 2006, ApJS, 167, 334

Badnell, N. R., et al. 2003, A&A, 406, 1151

Baker, J. G., & Menzel, D. H. 1938, ApJ, 88, 52

Baldwin, J. A., Ferland, G. J., Martin, P. G., Corbin, M. R., Cota, S. A., Peterson, B. M., & Slettebak, A. 1991, ApJ, 374, 580

Barinovs, Ğ., van Hemert, M. C., Krems, R., & Dalgarno, A. 2005, ApJ, 620, 537

Barklem, P. S. 2007, A&A, 462, 781

Barklem, P. S., Belyaev, A. K., Spielfiedel, A., Guitou, M., & Feautrier, N. 2012, A&A, 541, A80

Bauman, R. P., Porter, R. L., Ferland, G. J., & MacAdam, K. B. 2005, ApJ, 628, 541

Bautista, M. A., & Kallman, T. R. 2000, ApJ, 544, 581

Bell, K. L., Berrington, K. A., & Thomas, M. R. J. 1998, MNRAS, 293, L83

Benjamin, R. A., Skillman, E. D., & Smits, D. P. 1999, ApJ, 514, 307

Berrington, K. A., Burke, P. G., Dufton, P. L., & Kingston, A. E. 1985, Atomic Data and Nuclear Data Tables, 33, 195

Berrington, K. A., Saraph, H. E., & Tully, J. A. 1998, A&AS, 129, 161

Bhatia, A. K., & Kastner, S. O. 1993, Atomic Data and Nuclear Data Tables, 54, 133

Black, J. H. 1987, in Astrophysics and Space Science Library, Vol. 134, Interstellar Processes (Hollenbach, D. J. and Thronson, Jr., H. A.), 731–744

Brocklehurst, M. 1971, MNRAS, 153, 471

_____. 1972, MNRAS, 157, 211

Burgess, A., & Summers, H. P. 1969, ApJ, 157, 1007

_____. 1987, MNRAS, 226, 257

Burgess, A., & Tully, J. A. 1992, A&A, 254, 436

Butler, K., & Zeippen, C. J. 1994, A&AS, 108, 1

Cassidy, C. M., Ramsbottom, C. A., & Scott, M. P. 2011, ApJ, 738, 5

Cazaux, S., & Tielens, A. G. G. M. 2002, ApJ, 575, L29

————. 2004, ApJ, 604, 222

————. 2010, ApJ, 715, 698

Chandrasekhar, S. 1957, An introduction to the study of stellar structure. (New York, Dover Publications)

————. 1960, Radiative transfer (New York: Dover)

Chatzikos, M., Ferland, G. J., Williams, R. J. R., Porter, R., & van Hoof, P. A. M. 2013, ApJ, 779, 122

Chatzikos, M., et al. 2015, MNRAS, 446, 1234

Chekhovskoy, V. Y. 1971, J. Chem. Thermodynamics, 3, 289

Chung, H.-K., Bowen, C., Fontes, C. J., Hansen, S. B., & Ralchenko, Y. 2013, High Energy Density Physics, 9, 645

Chung, H.-K., Chen, M. H., Morgan, W. L., Ralchenko, Y., & Lee, R. W. 2005, High Energy Density Physics, 1, 3

Dalgarno, A., & McCray, R. A. 1972, ARA&A, 10, 375

Davidson, K. 1975, ApJ, 195, 285

D'Cruz, N. L., Sarazin, C. L., & Dubau, J. 1998, ApJ, 501, 414

Del Zanna, G., Storey, P. J., & Badnell, N. R. 2014a, A&A, 566, A123

Del Zanna, G., Storey, P. J., Badnell, N. R., & Mason, H. E. 2014b, A&A, 565, A77

Del Zanna, G., Storey, P. J., & Mason, H. E. 2014c, A&A, 567, A18

Dere, K. P. 2007, A&A, 466, 771

Dere, K. P., Landi, E., Mason, H. E., Monsignori Fossi, B. C., & Young, P. R. 1997, A&AS, 125

Draine, B. T. 2011, Physics of the Interstellar and Intergalactic Medium (Princeton University Press)

Draine, B. T., & Bertoldi, F. 1996, ApJ, 468, 269

Dufton, P. L., & Kingston, A. E. 1987, Journal of Physics B Atomic Molecular Physics, 20, 3899

Elwert, T., Ferland, G. J., Henney, W. J., & Williams, R. J. R. 2005, in IAU Symposium, Vol. 235, IAU Symposium, 132P

Fabian, A. C., Nulsen, P. E. J., & Canizares, C. R. 1984, Nature, 310, 733

Ferland, G. J. 1980, PASP, 92, 596

————. 2003, ARA&A, 41, 517

Ferland, G. J., Henney, W. J., O'Dell, C. R., & Peimbert, M. 2016, RMxAA, 52, 261

Ferland, G. J., Henney, W. J., O'Dell, C. R., Porter, R. L., van Hoof, P. A. M., & Williams, R. J. R. 2012, ApJ, 757, 79

Ferland, G. J., Korista, K. T., Verner, D. A., Ferguson, J. W., Kingdon, J. B., & Verner, E. M. 1998, PASP, 110, 761

Ferland, G. J., Peterson, B. M., Horne, K., Welsh, W. F., & Nahar, S. N. 1992, ApJ, 387, 95

Ferland, G. J., & Rees, M. J. 1988, ApJ, 332, 141

Ferland, G. J., & Williams, R. J. R. 2016, in Modern Methods in Collisional-Radiative Modeling of Plasmas, ed. Y. Ralchenko (Cham: Springer International Publishing), 153–180

Ferland, G. J., et al. 2013, RMxAA, 49, 137

Fernández-Menchero, L., Del Zanna, G., & Badnell, N. R. 2014a, A&A, 566, A104

————. 2014b, A&A, 572, A115

Flower, D. R., Le Bourlot, J., Pineau des Forêts, G., & Roueff, E. 2000, MNRAS, 314, 753

Froese Fischer, C., & Tachiev, G. 2004, Atomic Data and Nuclear Data Tables, 87, 1

Froese Fischer, C., Tachiev, G., & Irimia, A. 2006, Atomic Data and Nuclear Data Tables, 92, 607

Galavis, M. E., Mendoza, C., & Zeippen, C. J. 1995, A&AS, 111, 347

————. 1997, A&AS, 123, 159

Garstang, R. H. 1993, in Bulletin of the American Astronomical Society, Vol. 25, American Astronomical Society Meeting Abstracts #182 (Washington, AAS), 934

Glover, S. C. O., & Abel, T. 2008, MNRAS, 388, 1627

Gnat, O. 2017, ApJS, 228, 11

Gnat, O., & Ferland, G. J. 2012, ApJS, 199, 20

Gnat, O., & Sternberg, A. 2007, ApJS, 168, 213

Goldsmith, P. F., Langer, W. D., Pineda, J. L., & Velusamy, T. 2012, ApJS, 203, 13

Graney, C. M., & Sarazin, C. L. 1990, ApJ, 364, 561

Grieve, M. F. R., & Ramsbottom, C. A. 2012, MNRAS, 424, 2461

Griffin, D. C., Mitnik, D. M., & Badnell, N. R. 2001, Journal of Physics B Atomic Molecular Physics, 34, 4401

Guzmán, F., Badnell, N. R., Chatzikos, M., van Hoof, P. A. M., Williams, R. J. R., & Ferland, G. J. 2017a, MNRAS, 467, 3944

Guzmán, F., Badnell, N. R., Williams, R. J. R., van Hoof, P. A. M., Chatzikos, M., & Ferland, G. J. 2016, MNRAS, 459, 3498

————. 2017b, MNRAS, 464, 312

Haardt, F., & Madau, P. 2012, ApJ, 746, 125

He, X., Chen, A., Zhang, C., & Li, B. 1990, Journal of Physics B Atomic Molecular Physics, 23, 661

Heise, C., Smith, P. L., & Calamai, A. G. 1995, ApJ, 451, L41

Henney, W. J., Arthur, S. J., Williams, R. J. R., & Ferland, G. J. 2005, ApJ, 621, 328

Henney, W. J., Williams, R. J. R., Ferland, G. J., Shaw, G., & O'Dell, C. R. 2007, ApJ, 671, L137

Hollenbach, D., & McKee, C. F. 1989, ApJ, 342, 306

Hubeny, I., & Mihalas, D. 2014, Theory of Stellar Atmospheres (Princeton, NJ: Princeton University Press)

Hudson, C. E., Norrington, P. H., Ramsbottom, C. A., & Scott, M. P. 2012a, A&A, 537, A12

Hudson, C. E., Ramsbottom, C. A., & Scott, M. P. 2012b, ApJ, 750, 65

Hummer, D. G., & Storey, P. J. 1987, MNRAS, 224, 801

————. 1998, MNRAS, 297, 1073

Irons, F. E. 1978, MNRAS, 182, 705

Izotov, Y. I., Thuan, T. X., & Guseva, N. G. 2014, Monthly Notices of the Royal Astronomical Society, 445, 778

Jaquet, R., Staemmler, V., Smith, M. D., & Flower, D. R. 1992, Journal of Physics B Atomic Molecular Physics, 25, 285

Johnson, C. T., Burke, P. G., & Kingston, A. E. 1987, Journal of Physics B Atomic Molecular Physics, 20, 2553

Jordan, C. 1969, MNRAS, 142, 501

Kisielius, R., Kulkarni, V. P., Ferland, G. J., Bogdanovich, P., & Lykins, M. L. 2014, ApJ, 780, 76

Kisielius, R., Kulkarni, V. P., Ferland, G. J., Bogdanovich, P., Som, D., & Lykins, M. L. 2015, ApJ, 804, 76

Kisielius, R., Storey, P. J., Ferland, G. J., & Keenan, F. P. 2009, MNRAS, 397, 903

Kramida, A., Yu. Ralchenko, Reader, J., & and NIST ASD Team. 2014, NIST Atomic Spectra Database (ver. 5.2), [Online]. Available: http://physics.nist.gov/asd [2014, November 28]. National Institute of Standards and Technology, Gaithersburg, MD.

Krems, R. V., Jamieson, M. J., & Dalgarno, A. 2006, ApJ, 647, 1531

Krueger, T. K., & Czyzak, S. J. 1970, Proceedings of the Royal Society of London Series A, 318, 531

Kwon, D.-H., & Savin, D. W. 2014, ApJ, 784, 13

Kwong, H. S., Johnson, B. C., Smith, P. L., & Parkinson, W. H. 1983, Phys. Rev. A, 27, 3040

Laha, S., et al. 2016, MNRAS, 455, 3405

Landi, E., Del Zanna, G., Young, P. R., Dere, K. P., & Mason, H. E. 2012, ApJ, 744, 99

Laor, A., & Draine, B. T. 1993, ApJ, 402, 441

Le Bourlot, J., Le Petit, F., Pinto, C., Roueff, E., & Roy, F. 2012, A&A, 541, A76

Le Bourlot, J., Pineau des Forêts, G., & Flower, D. R. 1999, MNRAS, 305, 802

Le Teuff, Y. H., Millar, T. J., & Markwick, A. J. 2000, A&AS, 146, 157

Lennon, D. J., & Burke, V. M. 1994, A&AS, 103, 273

Liang, G. Y., & Badnell, N. R. 2010, A&A, 518, A64

Liang, G. Y., Whiteford, A. D., & Badnell, N. R. 2009, A&A, 500, 1263

Lique, F. 2015, MNRAS, 453, 810

Luridiana, V., Simón-Díaz, S., Cerviño, M., Delgado, R. M. G., Porter, R. L., & Ferland, G. J. 2009, ApJ, 691, 1712

Lykins, M. L., Ferland, G. J., Porter, R. L., van Hoof, P. A. M., Williams, R. J. R., & Gnat, O. 2013, MNRAS, 429, 3133

Lykins, M. L., et al. 2015, ApJ, 807, 118

Mao, J., Kaastra, J., & Badnell, N. R. 2017, A&A, 599, A10

McElroy, D., Walsh, C., Markwick, A. J., Cordiner, M. A., Smith, K., & Millar, T. J. 2013, A&A, 550, A36

McLaughlin, B. M., Lee, T.-G., Ludlow, J. A., Landi, E., Loch, S. D., Pindzola, M. S., & Ballance, C. P. 2011, Journal of Physics B Atomic Molecular Physics, 44, 175206

Mehdipour, M., Kaastra, J. S., & Kallman, T. 2016, A&A, 596, A65

Mendoza, C. 1983, in IAU Symposium, Vol. 103, Planetary Nebulae, ed. D. R. Flower, 143–172

Menzel, D. H., & Pekeris, C. L. 1935, MNRAS, 96, 77

Monteiro, T. S., & Flower, D. R. 1987, MNRAS, 228, 101

Nikolić, D., Gorczyca, T. W., Korista, K. T., Ferland, G. J., & Badnell, N. R. 2013, ApJ, 768, 82

Osorio, Y., Barklem, P. S., Lind, K., Belyaev, A. K., Spielfiedel, A., Guitou, M., & Feautrier, N. 2015, A&A, 579, A53

Osterbrock, D. E., & Ferland, G. J. 2006, Astrophysics of gaseous nebulae and active galactic nuclei, 2nd. ed. (Sausalito, CA: University Science Books)

Pelan, J., & Berrington, K. A. 1995, A&AS, 110, 209

Pengelly, R. M., & Seaton, M. J. 1964, MNRAS, 127, 165

Péquignot, D. 1986, in Model Nebulae, ed. D. Pequignot, 363

Pequignot, D. 1990, A&A, 231, 499

Piron, R., et al. 2017, High Energy Density Physics, 23, 38

Podobedova, L. I., Kelleher, D. E., & Wiese, W. L. 2009, Journal of Physical and Chemical Reference Data, 38, 171

Porter, R. L., Bauman, R. P., Ferland, G. J., & MacAdam, K. B. 2005, ApJ, 622, L73

Porter, R. L., & Ferland, G. J. 2007, ApJ, 664, 586

Porter, R. L., Ferland, G. J., Kraemer, S. B., Armentrout, B. K., Arnaud, K. A., & Turner, T. J. 2006, PASP, 118, 920

Porter, R. L., Ferland, G. J., & MacAdam, K. B. 2007, ApJ, 657, 327

Porter, R. L., Ferland, G. J., Storey, P. J., & Detisch, M. J. 2012, MNRAS, 425, L28

Ramsbottom, C. A., Bell, K. L., & Keenan, F. P. 1997, MNRAS, 284, 754

Röllig, M., Szczerba, R., Ossenkopf, V., & Glück, C. 2013, A&A, 549, A85

Röllig, M., et al. 2007, A&A, 467, 187

Roueff, E., & Le Bourlot, J. 1990, A&A, 236, 515

Rouleau, F., & Martin, P. G. 1991, ApJ, 377, 526

Rybicki, G. B. 1984, in Methods in Radiative Transfer, ed. W. Kalkofen (Cambridge University Press), 21–64

Rybicki, G. B., & Lightman, A. P. 1979, Radiative processes in astrophysics (New York, Wiley-Interscience), 393 p.

Saraph, H. E., & Storey, P. J. 1996, A&AS, 115, 151

Saraph, H. E., & Tully, J. A. 1994, A&AS, 107, 29

Schirmer, M. 2016, PASP, 128, 114001

Schöier, F. L., van der Tak, F. F. S., van Dishoeck, E. F., & Black, J. H. 2005, A&A, 432, 369

Schroder, K., Staemmler, V., Smith, M. D., Flower, D. R., & Jaquet, R. 1991, Journal of Physics B Atomic Molecular Physics, 24, 2487

Seaton, M. 1987, Journal of Physics B Atomic Molecular Physics, 20, 6363

Seaton, M. J. 1959, MNRAS, 119, 81

————. 1962, Proceedings of the Physical Society, 79, 1105

————. 1964, MNRAS, 127, 177

Sellgren, K., Tokunaga, A. T., & Nakada, Y. 1990, ApJ, 349, 120

Shaw, G., Ferland, G. J., Abel, N. P., Stancil, P. C., & van Hoof, P. A. M. 2005, ApJ, 624, 794

Spitzer, L. 1962, Physics of Fully Ionized Gases (2nd edition) (New York: Interscience)

————. 1978, Physical processes in the interstellar medium (New York Wiley-Interscience), 333 p.

Spitzer, L. J., & Tomasko, M. G. 1968, ApJ, 152, 971

Staemmler, V., & Flower, D. R. 1991, Journal of Physics B Atomic Molecular Physics, 24, 2343

Storey, P. J., & Hummer, D. G. 1995, MNRAS, 272, 41, on the web at http://adc.gsfc.nasa.gov/adc-cgi/cat.pl?/catalogs/6/6064/

Storey, P. J., & Sochi, T. 2016, MNRAS, 459, 2558

Storey, P. J., Sochi, T., & Badnell, N. R. 2014, MNRAS, 441, 3028

Storey, P. J., & Zeippen, C. J. 2000, MNRAS, 312, 813

Storey, P. J., Zeippen, C. J., & Sochi, T. 2015, ArXiv e-prints

Summers, H. P., et al. 2006, Plasma Physics and Controlled Fusion, 48, 263

Sunyaev, R. A., & Vainshtein, L. A. 1968, Astrophys. Lett., 1, 69

Sutherland, R. S., & Dopita, M. A. 1993, ApJS, 88, 253

Tachiev, G., & Froese Fischer, C. 2001, Canadian Journal of Physics, 79, 955

Tayal, S. S. 1997, Atomic Data and Nuclear Data Tables, 67, 331

————. 2006, ApJS, 163, 207

————. 2008, A&A, 486, 629

Tayal, S. S., & Zatsarinny, O. 2010, ApJS, 188, 32

Tielens, A. G. G. M. 2005, The Physics and Chemistry of the Interstellar Medium (Cambridge, UK: Cambridge University Press)

Tielens, A. G. G. M., & Hollenbach, D. 1985, ApJ, 291, 722

van Hoof, P. A. M., Ferland, G. J., Williams, R. J. R., Volk, K., Chatzikos, M., Lykins, M., & Porter, R. L. 2015, MNRAS, 449, 2112

van Hoof, P. A. M., Weingartner, J. C., Martin, P. G., Volk, K., & Ferland, G. J. 2004, MNRAS, 350, 1330

van Hoof, P. A. M., Williams, R. J. R., Volk, K., Chatzikos, M., Ferland, G. J., Lykins, M., Porter, R. L., & Wang, Y. 2014, MNRAS, 444, 420

Verner, D. A., Ferland, G. J., Korista, K. T., & Yakovlev, D. G. 1996, ApJ, 465, 487

Verner, E. M., Verner, D. A., Korista, K. T., Ferguson, J. W., Hamann, F., & Ferland, G. J. 1999, ApJS, 120, 101

Voronov, G. S. 1997, Atomic Data and Nuclear Data Tables, 65, 1

Vrinceanu, D., & Flannery, M. R. 2001a, Phys. Rev. A, 63, 032701

————. 2001b, Journal of Physics B Atomic Molecular Physics, 34, L1

Vrinceanu, D., Onofrio, R., & Sadeghpour, H. R. 2012, ApJ, 747, 56

Wang, S., & McConkey, J. W. 1992, Journal of Physics B Atomic Molecular Physics, 25, 5461

Wang, Y., Ferland, G. J., Lykins, M. L., Porter, R. L., van Hoof, P. A. M., & Williams, R. J. R. 2014, MNRAS, 440, 3100

Wasson, I. R., Ramsbottom, C. A., & Scott, M. P. 2011, ApJS, 196, 24

Wiesenfeld, L., & Goldsmith, P. F. 2014, ApJ, 780, 183

Williams, R. J. R., Guzmán, F., Badnell, N. R., van Hoof, P. A. M., Chatzikos, M., & Ferland, G. J. 2017, Journal of Physics B Atomic Molecular Physics, 50, 115201

Witthoeft, M. C., & Badnell, N. R. 2008, A&A, 481, 543

Wrathmall, S. A., Gusdorf, A., & Flower, D. R. 2007, MNRAS, 382, 133

Zhang, H. 1996, A&AS, 119, 523

Nicholas P. Abel: Department of Physics, University of Cincinnati, 4200 Clermont College Drive, Batavia, Ohio, 45103, USA (npabel2@gmail.com).

N. R. Badnell: Department of Physics, University of Strathclyde, Glasgow, G4 0NG, UK (badnell@phys.strath.ac.uk).

M. Chatzikos, F. Guzmán, Gary J. Ferland and Matthew L. Lykins: Department of Physics and Astronomy, University of Kentucky, Lexington, KY 40506, USA (gary@pa.uky.edu, mchatzikos@gmail.com, francisco.guzman@uky.edu, mllyki3@uky.edu).

Francis P. Keenan: Astrophysics Research Centre, School of Mathematics and Physics, Queen's University Belfast, Belfast BT7 1NN, Northern Ireland, U.K. (f.keenan@qub.ac.uk).

Ryan L. Porter and Phillip Stancil: Department of Physics and Astronomy and Center for Simulational Physics, The University of Georgia, Athens, Georgia 30602-2451, USA (ryanlporter@gmail.com, stancil@physast.uga.edu).

Peter A. M. van Hoof: Royal Observatory of Belgium, Ringlaan 3, 1180 Brussels, Belgium (p.vanhoof@oma.be).

Robin J. R. Williams: AWE plc, Aldermaston, Reading RG7 4PR, UK (robin.williams@awe.co.uk).